UNIVERSITY OF OTTAWA

PH.D. THESIS

Tailoring Metasurface Lattice-Controlled Resonances for Flat-Optic Applications

Author:

MD SAAD-BIN-ALAM

Supervisors:

KSENIA DOLGALEVA & ROBERT W. BOYD

A thesis submitted to the University of Ottawa in partial fulfillment of the requirements for the Doctorate in Philosophy (Ph.D.) in Electrical and Computer Engineering

uOttawa

Faculté de génie
Faculty of Engineering

School of Electrical Engineering and Computer Science
University of Ottawa

Declaration of Authorship

I, Md SAAD-BIN-ALAM, declare that this thesis, titled "Tailoring Metasurface Lattice-Controlled Resonances for Flat-Optic Applications", and the work presented in it are my own. I confirm that except where specific reference is made to the work of others, the contents of this dissertation are original and have not been submitted in whole or in part for consideration for any other degree or qualification in this, or any other university. This dissertation is my own work and contains nothing which is the outcome of work done in collaboration with others, except as specified in the text and Acknowledgements.

Md Saad-Bin-Alam
January, 2023
Ottawa, Canada

UNIVERSITY OF OTTAWA

Abstract

Faculty of Engineering

School of Electrical Engineering and Computer Science

Doctorate in Philosophy (Ph.D.) in Electrical and Computer Engineering

Tailoring Metasurface Lattice-Controlled Resonances for Flat-Optic Applications

by Md SAAD-BIN-ALAM

Flat-optics enable the miniaturization of many traditional bulk photonic devices routinely used in optical modulation and detection in telecommunication systems, biosensing and microscopic imaging in biomedical research, and light detection and ranging (LiDAR) used in automobile, military and surveillance applications. The backbone of typical flat-optic devices are the metasurfaces comprising structured nanoparticle lattices embedded in flat layer of traditional dielectric or semiconductor optical materials. The metasurface lattices can create optical resonances by exploiting different aspects of the light-matter interaction, *e.g.*, light absorption, radiation, scattering and diffraction by the nanoparticles array. Such resonances are essential for the efficient optical interactions performed by the flat-optic devices, for example, enhancing nonlinear second-harmonic generation for optical frequency modulators, or enhancing light absorption in photodetectors.

This Ph.D. dissertation reports the mechanisms of exciting and tailoring the metasurface lattice-controlled resonances using metal nanoparticle arrays. Exhibiting localized surface plasmon effects, metal particles can dramatically enhance the light field intensity under resonance conditions. Nevertheless, by nature, metal particles concurrently exhibit high absorption, radiation, and scattering losses, which cannot be sufficiently suppressed by the localized surface plasmon resonances. Almost two decades ago, researchers theoretically estimated that the benefits of the plasmonic field enhancement could

still be harnessed by suppressing the scattering loss by organizing such lossy metal particles in a periodic lattice formation. In contrast to the low-Q localized resonances, such an engineered lattice arrangement could excite high-Q nonlocalized resonances, which are now often called as lattice plasmon or surface lattice resonances. Notwithstanding, the efforts on the experimental validation of such a concept were not succeeding as per expectation in terms of the resonance Q-factors. Thus, prior to the work accomplished in this dissertation, it was largely believed by the photonics community that, it is the 'lossy' plasmonic metal particles that do not allow to excite the high-Q resonances as per the minimum requirements in the practical flat optic applications.

As a primary contribution to my Ph.D. dissertation, we successfully debunk that myth. In our work, we systematically proved that the non-localized lattice resonances can still be excited in 'lossy' metal nanoparticle arrays. Precisely, we improved both the design of the metasurface lattices and their fabrication and characterization techniques to eventually observe the high-Q lattice resonances as per the theoretical prediction. Our primary success later inspired us to analyze the systems more profoundly to make them suitable for different types of practical applications, which ultimately resulted in additional secondary successful projects described in my Ph.D. dissertation. The success of these projects would allow us in the future to utilize the nonlocalized plasmonic metasurface lattice-controlled resonances in a diverse range of flat integrated photonics applications, such as free-space light modulation and detection, which may rely on the nonlinear or electro-optical light-matter interaction in the flat thin-film region. We believe that the outcome of this dissertation will pave the way to designing and manufacturing efficient flat meta-optic devices for real-life applications, particularly in the telecommunication and medical sectors for the utmost betterment of human civilization.

Acknowledgements

All glory to Allah the Almighty, the Magnificent, the most Wise and the most Merciful for letting me accomplish my Ph.D. dissertation. Truly, my gratitude for our Lord Allah Subhanau wa Ta'la has no limit, who created us in the best shapes and educated us with His knowledge through His divine books and His messengers (PBUH) via His angels. Oh Allah, I testify that, verily, we are from You, and verily we will return to You!

This dissertation is a compilation of my primary research contributions in the field of plasmonic metasurface flat resonators, which I carried out at the University of Ottawa, Canada. I want to express my heartiest respect and gratitude to my supervisors, Prof. Ksenia P. Dolgaleva and Prof. Robert W. Boyd, for allowing me to be in the Canada Excellence Research Chair (CERC) group as a graduate student. It was an absolute honor to be nominated by my supervisors as the lead research student in a fantastic research field. Undoubtedly, the time I spent as a graduate student in our research group was the best part of my academic educational career.

The successful accomplishments of all my research work were possible thanks to a bunch of senior research fellows affiliated with our group in different phases of my graduate study. My extreme love and gratitude go to my two immediate mentors-come-big brothers: (1) Dr. Orad Reshef, who primarily groomed me in optical device simulation, nurtured me as a professional researcher and supported me selflessly in both good and challenging moments, and (2) Dr. Mikko J. Huttunen who trained me on hands-on lab experiments during the early stage of my graduate study (Master's) and later also invited me as a Visiting Research Student in his research group in Finland. I am also grateful to Prof. Kosmas L. Tsakmakidis for preparing my mind to analyze any theoretical matters during my Master's study.

I am heavily grateful and respectful to Dr. Jeremy Upham, the senior research fellow and the lab manager in Prof. Boyd's Lab, for his tremendous support in both academic and administrative aspects.

I want to express my sincere respect for Prof. Jeff Lundeen and Prof. Ebrahim Karimi, the two other group leaders in the CERC group, and Prof. Jean-Michel Ménard and Prof. Pierre Berini for their true love, encouragement and suggestions in different stages during my graduate study. My special thanks to Prof. Marti Kauranen from Tampere University in Finland for his love and guidance during my visit to his lab in 2018.

My special thanks to Dr. Brian T. Sullivan and Dr. Graham Carlow from Iridian Spectral Technologies Ltd. for giving me the opportunity to collaborate with them on a research project.

I am incredibly thankful to the other former and current postdoctoral fellows in our entire CERC group, namely, Dr. Daniel Espinoza, Dr. Robert Fickler, Dr. Lambert Ginner, Dr. Enno Giese, Dr. Girish Kulkarni, Dr. Boris Braverman, Dr. Israel De Leon, Dr. Sebastian Schulz, Dr. Boris Rosentein Levin, Dr. Girish Kulkarni, Dr. Rasool Alaee, Dr. Rocio Margoth Cordova Castro and Dr. Shubhendra Jain for their genuine admiration and encouragement for me, although we did not have the opportunity to work directly on any project together.

My special love, thanks and prayers must go to Dr. Kashif M. Awan and Dr. M. Zahirul Alam, the two senior Alumni in our group, who were my genuine well-wishers for all time and constantly expanded their help to me as my big brothers when I needed.

I want to express my respect and gratitude to Mr. Hugo Begin, Ms. Deniz Akmaner and Ms. Gloria Kaneza, the former administrative secretaries in our CERC group, for every administrative support they gave me with outstanding professionalism and enormous patience. My respect and gratitude will also be with the departed soul of Ms. Chelsea Burna, the former administrative secretary of the Centre for Research in Photonics at the University of Ottawa (CRPuO), whom I can never forget for her lovely support in different situations which she always provided with nice smiles coming from her pure-heart.

Besides, I would also like to acknowledge the love, guidance and encouragement from all the faculty members and staff in both the Faculty of Engineering and the Faculty of Science at the University of Ottawa, which I received on different occasions for my success and achievements.

I want to express my honest and endless love for my colleagues inside and beyond our research group, who were always beside me as my true friends, well-wishers and supports in different phases of my graduate student life. As an international student in Canada, I was so fortunate to meet many wonderful people from different cultural backgrounds who quickly turned into my close friends. Beyond the abovementioned people, the list of my friends' names is large. However, it is my honor to mention the names of my other colleagues-come-friends below. I firmly believe all of these people, whose names I am going to mention here (even the names of all my friends whose names I cannot recall now), will always remain as my true friends and well-wishers throughout the rest of my life, and vice versa.

The rest of my friends and colleagues (apart from the early-mentioned people) in both Prof. Dolgaleva and Prof. Boyd's groups at the uOttawa are: Kaustubh Vyas, Sisira Suresh, Mahdieh Chartab Jabbari, Theng-Loo Lim, Yaswant Vaddi, Maryam Abbasi, Ryan Hogan, Mohammad Karimi, Asad Ahmed Tahir, Payman Rasekh, Shayan Saeidi, Prova C. Gomez, Saad Jaddua, Yaryna Mamchur, Sijyl Fasih, Abdurrahman Hassan Abdi, Lisa Ackermann, Tomás Santiago-Cruz, Alperen Tügen, Stephen Harrigan, Isaac Soward, Rania Mahjoub, Daniel Hutama, Cheng Li, Ehsan Mobini, Sina Aghili, Sohel Zibod, Akbar Safari, Matt Runyon, Samuel Lemieux, Zohreh Hirbodvash, Tomas Jefferson Florez Gutierrez, Omid Mozafar, Mahtab Amooei, Ozan Oner, Mfon Odungide, Fatemeh Mousavi Karimi, Deniz Aydin, Tuhin Mishuk Paul, and the others whose names I cannot recall at this moment. Also, my friends from Prof. Boyd's University of Rochester group are: Saleem Iqbal, Saumya Choudhary, Nick Black, Surendar Vijayakumar, E. Samuel Arroyo-Rivera, and the others whose names I cannot remember at this moment.

My friends outside my research group are: Gazi Mahamudul Hassan, Khaled Sami Ramadan Atia, Joshua Baxter, Soheil Abdul Jalil, Deepak Kallepalli, Mujibur Rahman, Mehedi Hassan, Abdul Jabbar Siddiqui, Aldo Camilo Martinez, Alan Godfrey, Kate Fenwick, Maryam Amiri, Neda Nouri, Melika Afshar, Ali Maleki, Syeda Fatemeh Nazanin Dehgan Manshadi, Eeswar Kumar, Aswin Vishnuradhan, Ebin Joseph, Ashish Jain, Athulia Thulaseedharan, Manuel Ferrer-Garcia, Wei Cui, Ahmed Jaber, Alexei Halpin, Aidan Baker-Murray, Frédéric Bouchard, and so forth whose names I cannot remember right now. I am asking forgiveness from those whose names are missing here, but even though I forget their names now, I want to confirm that my love and respect will always be with them.

I also want to thank my all friends and well-wishers around the world whom became my friends during the meetings in different international conferences, particularly in the Optica Student Leadership Experience in 2022. I hope our friendship will last forever.

My special love will always be reserved for my undergraduate study batchmate-come friend (from my home country Bangladesh) Adnan Moin, his brother Arman Moin and cousin Shadman Shahriar, who were my roommates throughout most of my graduate student life in Canada. Also, I want to express my love for my other Bangladeshi friends Maruf Billah and Syed Hasan Arif. Without their accompany and support, my life beyond the university campus might have become lonely and boring.

I thank the University of Ottawa and the Ontario Ministry of College and Education for awarding me twice the prestigious 'Ontario Graduate Scholarship (OGS)' in the international student category in 2019 and 2021. In addition, I am also grateful to SPIE, IEEE Photonics Society and Optica for awarding me the student scholarships and travel grants to recognize my contributions to photonics research.

Last but not least, I express my utmost respect, love and gratitude to my Ammu and Abbu (my mother and father), Ms. Sufia Khatun (Alam) and Mr. Md Shamsul Alam. Out of all their selfless contributions and sacrifices for me from birth until today, they may have made the greatest sacrifice in their lives by allowing me to come abroad for my graduate studies. I have only one elder sister, who got married during my childhood; thus, I became the only child who stayed with my parents. Therefore, my parents wanted me to be with them during my childhood. It was hard for me to convince them that I wanted to pursue higher education abroad. Nevertheless, my sister Ms. Shammi Akhtar and my brother-in-law Mr. Nisher Khan came to my support my better career and eventually convinced our parents. I will always be grateful to my sister, brother-in-law and their family for my entire life. Eventually, my parents agreed to send me to Canada for my higher studies. However, in return, they almost become lonely, which often causes me to feel so guilty. My parents' support and sacrifices towards me and my entire career are priceless and incomparable to any other person's support. To my parents, I want to say thank you so much Ammu and Abbu for your endless and selfless love and tremendous support and sacrifices for me, which I never realized before coming abroad. Every day and night, my heart bleeds for you, but I could not fly to visit you every day to stay with you. I truly apologize for the pain that I have given in my childhood and that I am still giving in my adulthood. I am sincerely asking your pardon in the life herein and hereafter. Just you know that Allah the Almighty, the Lord of the universe, is my witness; I love and respect both of you more than anything from the universe!

Dedicated to-

Our Lord: Allah the Exalted, Almighty & Gracious;
who created light and matters (including me).

&

My parents: Sufia Khatun & Md Shamsul Alam;
who brought me in this colorful universe.

&

My all teachers from my childhood to adulthood;
whose advice always resonate with my success.

Contents

List of Abbreviations

ARC	**A**nti-**R**eflection **C**oating
BIC	**B**ound-States **I**n the **C**ontinuum
AR/VR	**A**ugmented **R**eality/**V**irtual **R**eality
CMOS	**C**omplementary **M**etal-**O**xide-**S**emiconductor
DBR	**D**istributed **B**ragg **R**eflector
DO	**D**iffraction **O**rder
DM	**D**ichroic **M**irror
ED	**E**lectric **D**ipole
EM	**E**lectro-**M**agnetic
EQ	**E**lectric **Q**uadrupole
FDTD	**F**inite-**D**ifference **T**ime-**D**omain
F-P	**F**abry-**P**érot
GMR	**G**uided **M**ode **R**esonance
HRS	**H**yper-**R**ayleigh **S**cattering
HWP	**H**alf-**W**ave **P**late
IR	**I**nfra**R**ed
LiDAR	**L**ight **D**etection **A**nd **R**anging
LPF	**L**ong **P**ass **F**ilter
LSP	**L**ocalized **S**urface **P**lasmon
LSPR	**L**ocalized **S**urface **P**lasmon **R**esonance
MD	**M**agnetic **D**ipole
MQ	**M**agnetic **Q**uadrupole
OPO	**O**ptical **P**arametric **A**mplifier
OSA	**O**ptical **S**pectrum **A**nalizer
PMT	**P**hoton **M**ultiplier **T**ube
Q.E.	**Q**uantum **E**fficiency
QD	**Q**uantum-**D**ot
RA	**R**ayleigh **A**nomaly
RWG	**R**esonant **W**aveguide **G**rating
SHG	**S**econd-**H**armonic **G**eneration
SFG	**S**um-**S**requency **G**eneration
SLR	**S**urface **L**attice **R**esonance
SNR	**S**ignal-to-**N**oise **R**atio
SPF	**S**hort **P**ass **F**ilter
SPDC	**S**pontaneous **P**arametric **D**own **C**onversion
SWIR	**S**hort **W**avelength **I**nfrared
TE	**T**ransverse **E**lectric
THG	**T**hird-**H**armonic **G**eneration
TIR	**T**otal **I**nternal **R**eflection

TM	Transverse **M**agnetic

Dissemination of Research

Primary Contribution

References

1. **M. S. Bin-Alam**, J. Baxter, K. M. Awan, A. Kiviniemi, Y. Mamchur, A. Cala'Lesina, K. L. Tsakmakidis, M. J. Huttunen, L. Ramunno and K. Dolgaleva, "Hyperpolarizability of plasmonic meta-atoms in metasurfaces," Nano Lett., **21**, 51–59 (2021).
2. **M. S. Bin-Alam**, O. Reshef, Y. Mamchur, M. Z. Alam, G. Carlow, J. Upham, B. T. Sullivan, J.-M. Ménard, M. J. Huttunen, R. W. Boyd and K. Dolgaleva, "Ultra-high-Q resonances in plasmonic metasurfaces," Nat. Commun., **12**, 1–8 (2021).
3. **M. S. Bin-Alam**, O. Reshef, R. N. Ahmad, J. Upham, M. J. Huttunen, K. Dolgaleva and R. W. Boyd, "Cross-polarized surface lattice resonances in a rectangular lattice plasmonic metasurface," Opt. Lett., **47**, 2105–2108 (2022).
4. O. Reshef, **M. Saad-Bin-Alam**, M. J. Huttunen, G. Carlow, B. Sullivan, J.-M. Ménard, K. Dolgaleva and R. W. Boyd, "Multiresonant high-Q plasmonic metasurfaces," Nano Lett., **19**, 6429–6434 (2019).
5. **M. S. Bin-Alam**, M. Z. Alam, K. Dolgaleva and R. W. Boyd, "Ultra-High-Q Multi-Resonant Metasurface using Plasmonic Lattice in Inhomogeneous Medium," Conference on Lasers and Electro-Optics (CLEO), IEEE, **12**, 1–2 (2022).

Collaborating Contribution

References

1. T.-L. Lim, Y. Vddi, **M. S. Bin-Alam**, L. Cheng, R. Alaee, J. Upham, M. J. Huttunen, K. Dolgaleva, O. Reshef and R. W. Boyd, "Fourier-Engineered Plasmonic Lattice Resonances," ACS Nano, **16**, 5696–5703 (2022).

Chapter 1

Introduction

1.1 Flat Optics for Free-Space Light Manipulation

Light is one of the forms of energy existing in the universe which comprises unlimited packets of massless particles known as photons. Unless they meet an object, waves of light can travel in free space following straight paths called rays with a constant velocity, which is the maximum speed in the universe. As a form of energy, light can be transformed into other types of energy (*e.g.*, electricity) or can be generated from other forms of energy. For example, the atoms of semiconductor materials can absorb the photons of light, which excite the electrons of the atoms; thus, the energy of light transforms into electronic energy. Conversely, such electrons emit photons while returning to their original or ground state; thus, the electronic energy converts into the energy of light again. Based on these principles, semiconductor materials are often used as light sources and detectors in various applications in our everyday life [1]–[3].

The properties of light include its intensity, spectral frequency or wavelength, polarization, and direction of propagation. At its point of origin, intensity, wavelength, and polarization of light can primarily be controlled by the source. Once emitted from the source, the traveling light's propagation direction and the rest of the properties can be manipulated by one or multiple optical elements made of naturally available materials placed at the trajectory of light. The direction of light propagation is affected by its transmission through (and refraction at the interfaces of) dielectric materials, reflection from the surfaces of dielectric or metallic materials, diffraction from optical structures, and scattering off small objects. The scientific branch of knowledge dealing with such light-matter interactions is known as Optics. Besides, the elements which control light's properties via light-matter interaction are often called optical components, or sometimes they are also just called Optics. The common optical elements which are typically used to manipulate light's properties in free space are lenses, mirrors, gratings. Light can also be brought from one point to another through the engineered optical media, such as, for example, optical fibers and waveguides made of natural materials [1]–[3].

The traditional optical elements, such as lenses, polarizers, beam-splitters, diffraction gratings, *etc*. are often required for manipulating free-space light's propagation direction, collimation, focusing, polarization, and temporal and spatial filtering [1]–[3]. Thus, such optical elements are routinely sought in imaging devices, such as cameras, microscopes, telescopes, and free-space optical communication devices, such as transmitters (*i.e.*, sources), modulators, receivers (*i.e.*, photodetectors), *etc*. Nonetheless, due to the rapid development of advanced commercial and military technology, the miniaturization and integration of such optical devices into complex systems are paramount. A common example of such complex systems is mobile smartphones. Just beyond the already existing imaging systems *e.g*. cameras, the latest versions of such smartphones include light detection and ranging systems (LiDARs) comprising lasers, lenses, and mirrors. However, the miniaturization of the traditional bulk optical components has almost reached its limit due to the subwavelength diffraction limit of the natural optical materials [4], [5]. On top of that, further thinning or flattening the optical materials (often called thin films) below the sub-micrometer range does not allow the input and output light signals to achieve phase-matching conditions, which is required for nonlinear optical processes.

Notwithstanding, thanks to the advent of modern nanotechnology, there is "plenty of room at the bottom" to make the miniaturized sub-micron or nanoscale-thick flat thin-film optical elements to be used and integrated into mobile devices like smartphones [6]–[10]. Using the state-of-the-art simulation software and nanofabrication hardware machines, nowadays it is possible to design and fabricate nanostructured flat optical thin films, which are commonly known as metasurfaces [9], [11]. Some specific metasurfaces have also recently been introduced as flat meta-optics [12]–[19]. The core building blocks of the metasurfaces are a bunch of periodically arranged nanowires or nanoparticles, which can confine and control the properties of light in the subwavelength regime by creating strong resonances associated with the interacting light [20]. Such resonances can boost the weak light-matter interaction and can relax the phase-matching condition in the miniaturized flat optical components [21]. In this dissertation, our ultimate goal is to improve the quality-factor (Q-factor) of such types of resonances and to explore their potentials. Thus, understanding and manipulating the resonance features in metasurfaces, henceforth called meta-optic systems are paramount. Below we briefly discuss the fundamentals and different aspects of the resonances corresponding to the flat optical domain.

1.2 Resonant Metasurfaces for Flat Optics

If light undergoes frequent back-to-back reflection or circulation within an optical system, the light intensity reaches its peak when the reflected or circulated light interferes constructively, and it exhibits a minimum when the interference is destructive. Such a phenomenon is called optical resonance, which allows for a confinement and storage of the energy of light within the optical system at resonance frequencies [1]. The specific configuration of the optical system that causes light to be confined and resonated within it is called an optical resonator. The energy of light leaked from the optical resonator at the peak of the resonance frequency or wavelength has greater magnitude than the energy leaked at the other frequencies or wavelengths not matching the resonance peak wavelength.

There are two types of light confinements that can take place in an optical resonator: temporal and spatial light confinements, which are typically characterized by the quality factor, Q, and by the mode volume, V, respectively. The fundamental definition of a Q-factor of a system can be expressed as [22], [23]

$$Q = 2\pi \times \frac{\text{Energy stored}}{\text{Energy dissipated per cycle}}, \tag{1.1}$$

alternatively which can also be expressed by the following relationship [21]

$$Q = \frac{\text{Resonance center wavelength}}{\text{Full width at half maximum (FWHM)}}, \tag{1.2}$$

which clearly indicates that linewidth broadening causes a lowering of the Q-factor. In other words, increasing the Q-factor of a resonator means enhancing the temporal light energy confinement (*i.e.*, storing energy over a longer period of time) in that resonator. On the contrary, increasing the volume size V of the resonator means lowering the spatial confinement in that resonator. If the purpose of using a finite-size resonator is the enhancement of the light energy, according to Purcell factor, $F_P \propto Q/V$, it is imperative to improve the resonator's resonance Q-factor [24].

The common optical resonators are typically consisting of two planar mirrors or two Bragg reflectors, which can be used to excite the Fabry-Pérot resonances by trapping longitudinal modes of light within a system by manipulating the distance between the two mirrors or reflectors. One of the most common applications of such bound optical resonators are bulk lasers where the gain media required for lasing are placed inside the resonators. However, in the flat optics context, the mechanisms of exciting optical resonances are quite different, which allows trapping of light within the subwavelength thin flat regions. The principal component of a resonating flat-optic system is a nanoparticle grating array artificially defined on or embedded inside the medium constituting the flat optics. Such artificially made nanoparticle grating

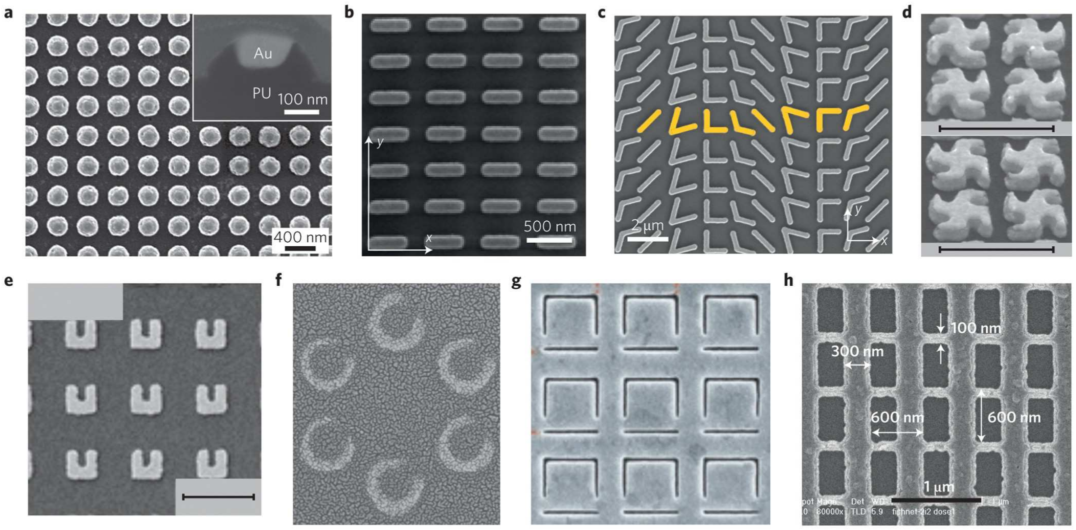

FIGURE 1.1: Examples of metasurfaces comprising meta-atoms. (a) Nanodisks, (b) bar- or rod antennas, (c) V-shaped antennas, (d) gammadions, (e) U-shaped split-ring resonators, (f) split-ring resonators with inner and outer diameters, (g) inverse asymmetric split-ring resonators, (h) double fishnet structures [20]. ©2014 Springer Nature.

arrays, called metasurfaces, are comprised of a series of structured subwavelength unit cells called meta-atoms or meta-molecules, as shown in Fig. 1.1(a-h) [20]. Below we briefly introduce different types of resonances associated with such meta-atoms and metasurfaces, and discuss their physical origin. Such resonant behavior can ultimately govern the functionalities of the flat optics.

1.2.1 Localized Resonances in Meta-Atom Nanostructures

Local-Field Enhancement, Scattering and Absorption Cross-Sections

Meta-atoms are the building blocks of metasurfaces, which can be made either by using subwavelength dielecric or metallic nanostructured particles of the volume V. Let us assume that the particle's radiaus a, the one-dimensional geometrical parameter, a associated with the particle's volume, V such that $V = \frac{4}{3}\pi a^3$, is much smaller than the wavelength of light, λ such that $a << \lambda$. Once it is encountered by an applied light field, E_0, the meta-atomic structure exhibits induced electric dipole (ED), electric quadrupole (EQ), magnetic dipole (MD) and magnetic quadrupole (MQ) moments [25]. Under the electrostatic approximation, the applied field $\mathbf{E_0}$ induces an electric dipole moment $\mathbf{p}$ with the magnitude proportional to $\mathbf{E_0}$ inside the meta-atom structure of the volume V and frequency-dependent, dispersive, complex dielectric constant $\epsilon(\omega) = \mathrm{Re}[\epsilon(\omega)] + \mathrm{Im}[\epsilon(\omega)]$ according to the following relation [26], [27]:

$$\mathbf{p} = 3\epsilon_0\epsilon_d V \frac{\epsilon(\omega) - \epsilon_d}{\epsilon(\omega) + 2\epsilon_d}\mathbf{E_0}. \tag{1.3}$$

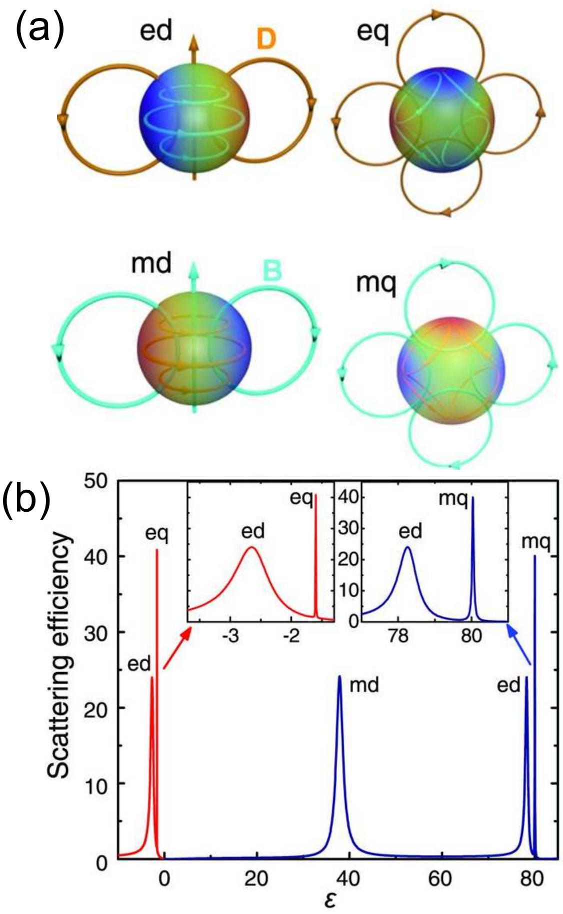

FIGURE 1.2: (a) Illustration of electric and magnetic dipolar and quadrupolar resonances (ED, EQ, MD, and MQ, respectively) supported by a nano-spherical structure [25]. (b) Scattering efficiency as a function of dielectric permittivity $\epsilon < 0$ for plasmonic (red color) and $\epsilon > 0$ for dielectric (blue color) nanostructures [25]. ©2016 American Association for the Advancement of Science. ©2007 Annual Review of Physical Chemistry.

Here ϵ_0 and ϵ_d are the vacuum permittivity and the homogeneous or effective dielectric constant of the media surrounding the structured particle of interest. Here, the term $3V[\epsilon(\omega) - \epsilon_d]/[\epsilon(\omega) + 2\epsilon_d]$ characterizes the particle's ability to become polarized by the applied electric field (the polarizability). Thus, one can define the polarizability $\alpha(\omega)$ of the particle as $\mathbf{p} = \epsilon_0\epsilon_d\alpha\mathbf{E_0}$, where

$$\alpha(\omega) = 3V\frac{\epsilon(\omega) - \epsilon_d}{\epsilon(\omega) + 2\epsilon_d}. \tag{1.4}$$

It is clear from Eq. (1.4) that the polarizability α of the nanoparticle experiences a resonant enhancement under the Fröhlich condition $\epsilon(\omega) = -2\epsilon_d$. The Fröhlich condition thus enhances the field $\mathbf{E_{in}}$ inside the particle in accordance with the following relationship:

$$\mathbf{E_{in}} = \frac{3\epsilon_d}{\epsilon(\omega) + 2\epsilon_d}\mathbf{E_0}. \tag{1.5}$$

The field outside the particle, $\mathbf{E_{out}}$, is also enhanced due to the dipole moment $\mathbf{p}$ according to the following relationship:

$$\mathbf{E_{out}} = \mathbf{E_0} + \frac{\mathbf{u}(\mathbf{u}.\mathbf{p}) - \mathbf{p}}{V\epsilon_0\epsilon_d}. \tag{1.6}$$

Here $\mathbf{u}$ is the unit vector in the direction of the outside field oscillation. Thus, such resonant oscillations cause the local-field enhancement inside and outside the particle locally coupling and confining the light energy within the subwavelength volume of the particle. The resonantly enhanced dipole moment increases the particles' ability to scatter and absorb light. The corresponding scattering and absorption cross sections, C_{sca} and C_{abs}, are characterized based on the Mie theory [28] by the following relationships:

$$C_{\text{sca}} = \frac{k^4}{6\pi}|\alpha(\omega)|^2, \tag{1.7}$$

and

$$C_{\text{abs}} = k\text{Im}[\alpha(\omega)]. \tag{1.8}$$

Here $k = \frac{2\pi}{\lambda}$ is the spatial angular frequency, *i.e.* the angular wave number that describe the number of oscillations that the optical wave completes per unit length. It is clear from Eq. (1.7) that C_{sca} scales as λ^{-4}, whereas C_{abs} scales as λ^{-1}. One can note that C_{sca} and C_{abs} also scale with $|\alpha(\omega)|$ and $\text{Im}[\alpha(\omega)]$, respectively. However, it is clear from Eq. (1.4) that, $\alpha(\omega) \propto V$. Thus, for small particles of volume V, we can write $C_{\text{sca}} \propto V^2$ and $C_{\text{abs}} \propto V$. Henceforth, if the particles' 1D geometrical parameter $a \propto V^{\frac{1}{3}}$ is on the order of magnitude of the wavelength of light, the scattering cross section C_{sca} will be dominant over the absorption cross section C_{abs}. Such scattering is known as Mie Scattering. In contrast, if the particle's 1D geometrical parameter $a \propto V^{\frac{1}{3}}$ is subwavelength, *i.e.* $a << \lambda$, the absorption cross section C_{abs} will be dominant over the scattering cross section, C_{sca}. Such subwavelength scattering is known as Rayleigh Scattering.

Mie and Localized Surface Plasmon Resonances

The illustration shown in Fig. 1.2(a) allows one to grasp an idea of the electric and magnetic dipole- and quadrupole-like localized resonances [25]. As the corresponding scattering cross-sections shown in Fig. 1.2(b), based on the Mie theory [28], both dielectric and metallic spherical particles can exhibit strong scattering resonances termed Mie resonances. These resonances depend on the dielectric permittivity ϵ and the particle size parameter $q = 2\pi a/\lambda$ that is proportional to the ratio between the radius of a spherical particle a and the wavelength of light. If the dimension parameters for both metallic and dielectric structures are the same, the dielectric permittivity, ϵ for a metal nanoparticle is negative, whereas for a dielectric nanoparticle ϵ is positive [25].

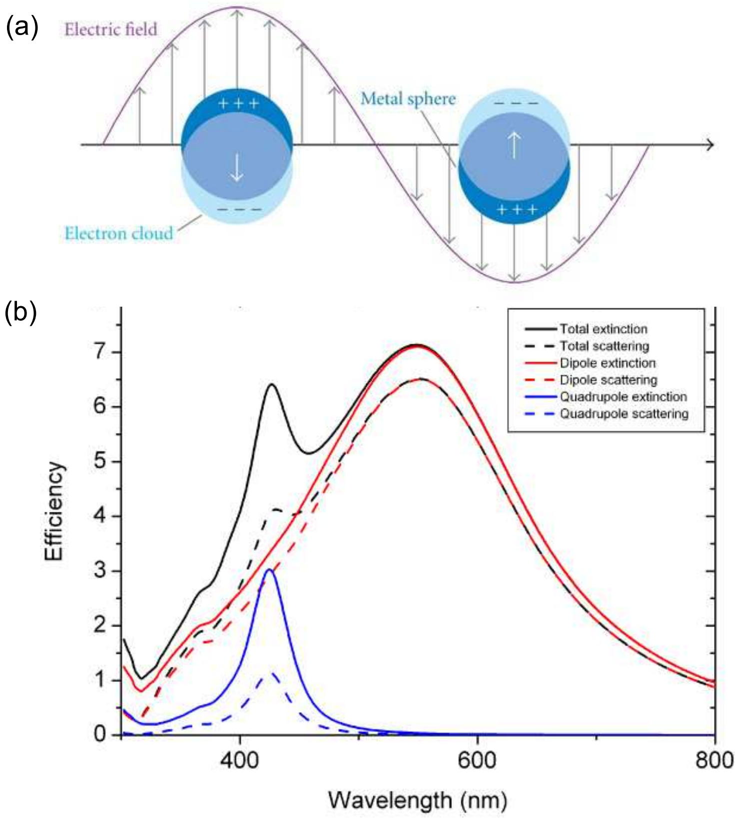

FIGURE 1.3: (a) Illustration of the localized surface plasmon resonances (LSPRs) [26], [29]. (b) Spectra showing the extinction (absorption + scattering) and scattering efficiencies of a plasmonic 100 nm diameter silver sphere surrounded by glass [30]. ©2010 Optical Society of America.

Physically, for the metallic particles, such Mie resonances happen due to the dipole moment oscillations of the free-electron clouds surrounding the metallic particles induced by the applied light of frequency ω_0 that is much smaller than the plasma frequency of the free-electrons ω_p (here, ω_p is the natural frequency of the free electrons in the gaseous state of metals). The oscillation of the free-electron cloud is illustrated in Fig. 1.3(a) [26], [29], which is known as the localized surface plasmon (LSP). Thus, the Mie resonances corresponding to that free-electron cloud oscillation of the metallic particles are called the localized surface plasmon resonances (LSPRs) [26], [27], [29]. Subwavelength metallic structures, for which $a << \lambda$, produce only LSPRs corresponding to the electric dipole (ED) and electric quadrupole (EQ) scattering and extinction (absorption + scattering) cross sections, as shown in Fig. 1.3(b) [25], [30], while the corresponding magnetic dipole (MD) and magnetic quadrupole (MQ) fields vanish inside the metallic structures. Since $a << \lambda$ for the metallic particles of consideration, the scattering demonstrated by such metallic particles is classified as the Rayleigh scattering.

1.2.2 Non-localized Resonances in Metasurface Gratings

So far, we have been discussing the light scattering and absorption incurred by the particles in electrostatic approximation. Nevertheless, apart from the scattering, the resonant particles absorbing applied electromagnetic (EM) light also act as dipole antennas that radiate EM light in free space. Once illuminated by an EM plane wave, the particles scatter that plane wave via dipole radiation. Now, let us consider a collection of nanoparticles arranged in a periodic lattice array with 2D periodicity, as shown in Fig. 1.4. Such lattice arrays comprising structured meta-atoms or meta-molecules are called metasurfaces [20]. The optical properties of such metasurfaces, *e.g.*, the scattering and the extinction (absorption + scattering) cross sections of the individual meta-atom particles, are governed by the localized resonant features [26]. Concurrently, such particles individually suffer from scattering and absorption losses (characterized by scattering and extinction cross sections of the particle). Such losses result in a quick damping of the localized resonances, thus the corresponding Q-factors are restricted to very low values (only on the order of 10). While the absorption loss is dominant in subwavelength metallic nanoparticles, their scattering loss can be suppressed by assembling them in a lattice formation. By engineering the lattice periodicity and the particles' sizes and shapes, one can excite non-localized high-Q resonances. Due to the nature of their origin, such non-localized resonances are known as surface lattice resonances (SLRs) [31]–[34]; below we briefly discuss them.

Surface Lattice Resonances from Radiation and Scattering Coupling

When a metasurface grating is illuminated at normal incidence by a plane wave with the wavelength λ_0, its constituent nanostructured particles exhibit collectively induced dipole moments along the polarization direction of the incident applied light. The array of the collectively oscillating induced dipole moments acts like a series of phased-array radiative antennas, which scatter the plane wave via in-phase radiation towards the orthogonal direction with respect to the polarization of the applied light, as illustrated in Fig. 1.4. The radiation of the scattered light collectively forms a standing grazing wave in the plane of the metasurface. Through constructive and destructive interference, spectral bands of bright and dark modes of the grazing wave, known as Rayleigh anomaly (RA), appear near the diffraction orders (DOs) of the metasurface grating. The radiated scattered light coupled to the RAs

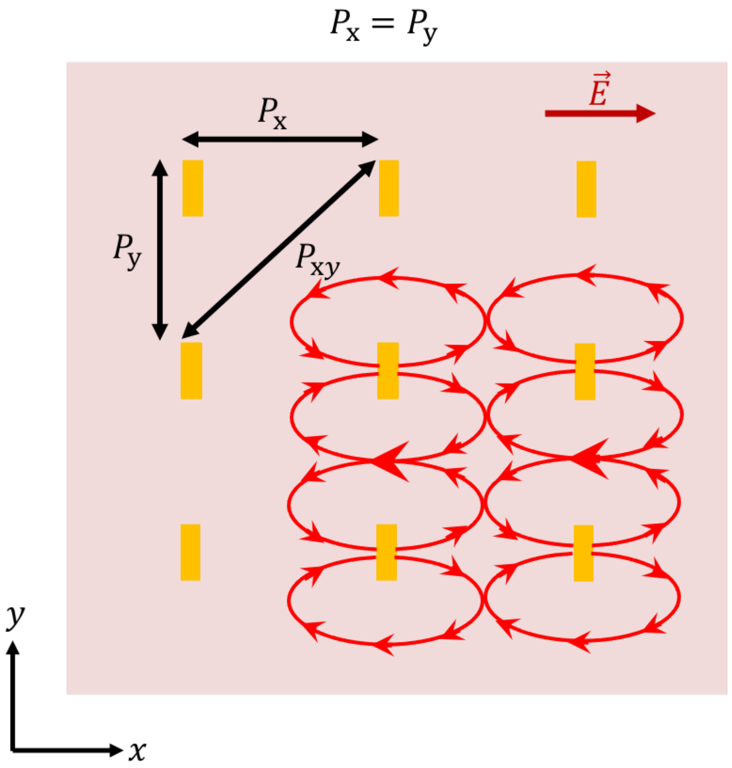

FIGURE 1.4: Illustration of the top view of a metasurface consisting of periodically arranged meta-atom nanoparticles illuminated by an incident light polarized along the x axis incident from the normal angle direction. Here, the periodicity of the nanoparticles' array, P_x and P_y along both x and y axes are equal. Also, P_{xy} is the periodicity in the diagonal direction. Under the x-polarized light, the radiation from the individual nanoparticles towards the y axis are in-phase, and thus can create surface lattice resonances. In contrast, no such a lattice resonance will be created towards the x axis due to the out-of-phase radiation.

results in both the plasmon-like radiation of the hybrid modes near the LSPR wavelengths, as well as the photon-like radiation of the RAs at the wavelengths near the DOs [31]–[34].

The RA wavelengths near the DOs depend on the periodicity of the grating array and the refractive index of the surrounding medium. For the grazing wave travelling in the metasurface array with the reciprocal lattice vector $\mathbf{G} = 2\pi/P \cdot \mathbf{u}$, where P is the array's periodicity and $\mathbf{u}$ is the unit vector along P, the Rayleigh condition requires that [35], [36]

$$\mathbf{k}_{||}^{\text{out}} = \mathbf{k}_{||}^{\text{in}} + \mathbf{G}, \tag{1.9}$$

where $\mathbf{k}_{||}^{\text{in}} = 2\pi n/\lambda_0 \cdot \mathbf{u}$ and $\mathbf{k}_{||}^{\text{out}} = 2\pi n/\lambda_{\text{RA}} \cdot \mathbf{u}$ are the projections of the incident and diffracted wave vectors, respectively, parallel to the array in the medium with the refractive index n surrounding the array. Under the plane-wave illumination at

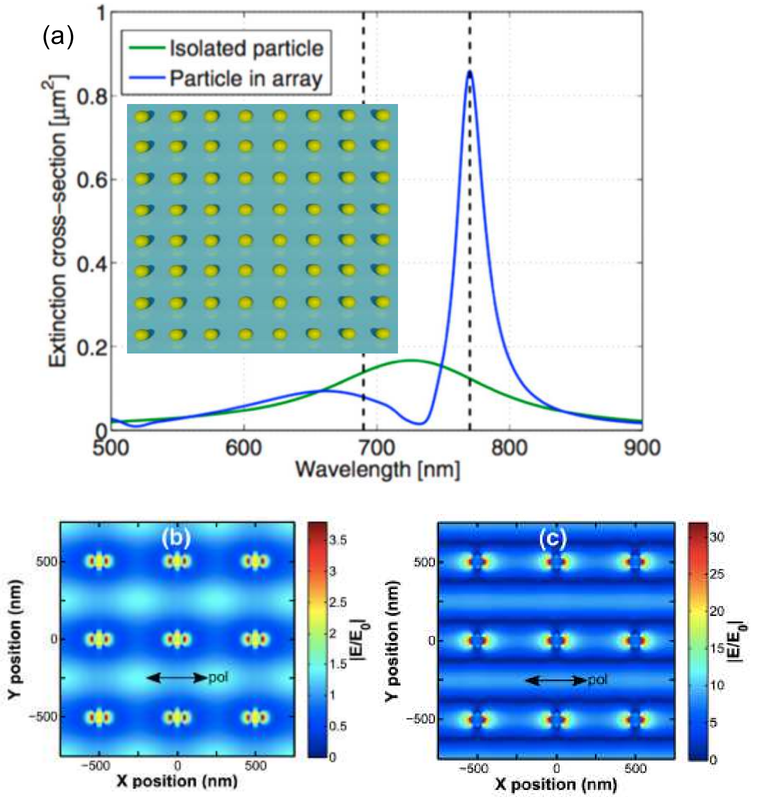

FIGURE 1.5: (a) Extinction cross-section of an isolated plasmonic nanoparticle that exhibits a Lorentz-like localized surface plasmon resonance (green color), and a metasurface comprising a 2D array of plasmonic nanoparticles [21]. (b-c) Normalized electric-field maps showing the field distribution due to the modified radiative LSPRs surrounding the isolated particles, and surface lattice resonances in the form of radiative standing grazing wave, respectively [32]. ©2018 American Chemical Society. ©2016 Optical Society of America.

normal incidence, $\mathbf{k}_{||}^{\text{in}} = 0$, thus, the Rayleigh condition for the normal incidence can be written as

$$\mathbf{k}_{||}^{\text{out}} = \mathbf{G}, \tag{1.10}$$

and can be converted into the expression for the in-plane RA wavelength

$$\lambda_{\text{RA}} = nP. \tag{1.11}$$

The hybridization of the localized resonant modes causes a Fano-like spectral modification of such resonances, slightly suppressing the radiation losses. Fig. 1.5(a) shows a Lorentz-like LSPR (green curve) corresponding to an isolated plasmonic nanoparticle, which is modified into a Fano-like lineshape (blue curve) with a slight blueshifting when such individual plasmonic nanoparticles periodically form a metasurface array [21]. On the other hand, the scattered light coupling with the RAs lacks the material absorption loss exhibiting the radiation loss only. Thus, the resonances excited via such low-loss coupling processes which happen in the plane of the metasurface usually exhibit spectrally narrow lineshapes, that is also shown in Fig. 1.5(a) by the blue curve. Thus, the high-Q (SLRs) are excited in the plane of the metasurface [21], [32]. The normalized electric-field maps in Fig. 1.5(b) and Fig. 1.5(c) demonstrate the typical field distribution corresponding to the localized LSPRs and non-localized SLRs, respectively [32].

In general, SLRs can be excited collectively by both dielectric and metallic nanostructures arranged in a periodic metasurface [31], [36]. Due to the relatively low absorption loss happening locally in the dielectric, one may ideally prefer to use dielectric nanoparticles instead of the metallic ones, *i.e.* plasmonic nanostructures. Nevertheless, if one's purpose is to excite high-Q SLRs with a greater flexibility in tunability, using subwavelength plasmonic nanostructures could be a better choice for that purpose. To protect the SLRs from being affected by the extinction losses associated with the nanostructures, it is paramount to design the metasurface such that it exhibits SLRs far from the localized resonances, in the longer-wavelength region [37]. One of the ways to achieve such spectral distance is to increase the lattice periodicity in the direction of the radiation (*i.e.*, orthogonal to the light polarization) to red-shift the SLRs from the localized resonances. However, in practice, if one needs to excite the SLRs at a particular wavelength, the only approach that can be taken is to blue-shift the localized resonances by reducing the dimensions of the nanostructures [37]. Applying the latter approach to dielectric nanostructures would be tricky, because decreasing the dimensions of a dielectric nanostructure (which is typically its radius) beyond a certain limit would result in disappearance of Mie scattering. In contrast to that, tuning LSPRs in metallic nanostructures is much more flexible. One can blue-shift the LSPRs by reducing the dimension of the metallic structures in the direction of the light polarization. Although such decreasing in one dimension would also reduce the Rayleigh scattering cross-section of the subwavelength metallic structures, one can boost the strength of such scattering by increasing their dimensions in the direction of the radiation of light (*i.e.*, perpendicular to the light polarization). Since SLRs are excited via radiative coupling, the SLR modes are bright modes.

Bound-States in the Continuum with Fano-like Resonances

The radiating modes corresponding to the in-phase dipole-like oscillations are known as the bright modes. Such modes are generally exhibited by the Mie resonances and the LSPRs. Nonetheless, there also exist non-radiating dark modes corresponding to the out-of-phase quadrupole-like oscillations (*i.e.*, the symmetric distributions of the out-of-phase positive and negative charges) in symmetrically shaped nanostructures [40]. Since there is no radiation of energy, such oscillations would have lossless

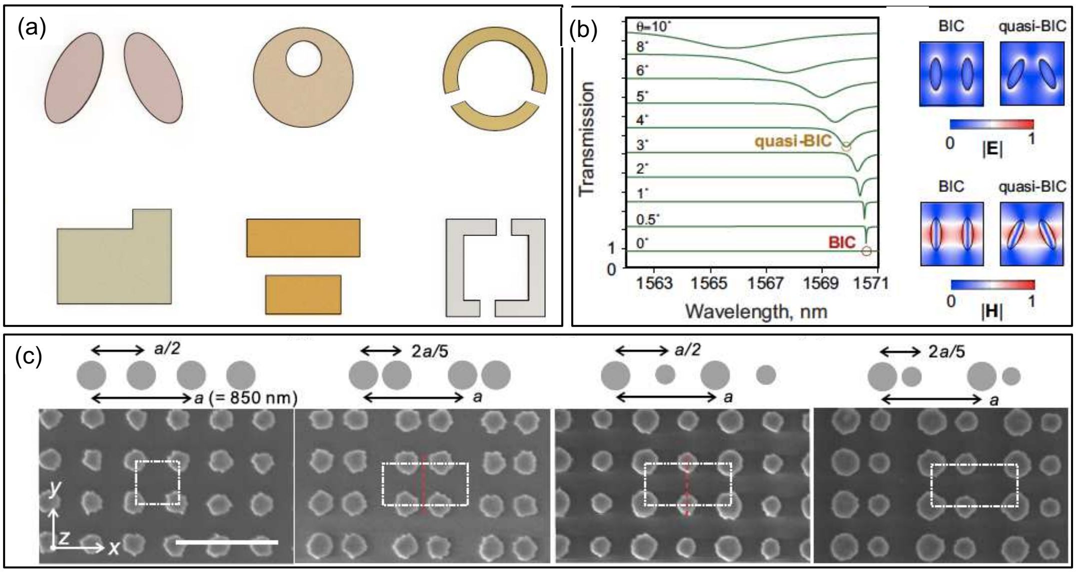

FIGURE 1.6: (a) Meta-atoms/meta-molecules with a broken in-plane inversion symmetry of the typical BIC/quasi-BIC metasurfaces [38]. (b) Evolution of the (d) Transformation of the BIC trasmission spectra into the Quasi-BIC as a function of the symmetry-breaking of the meta-atom/meta-molecule structures presented at the left inside the box. The corresponding electric and magnetic fields for the BICs and quasi-BICs are also presented at the right inside the box [38]. (c) Quasi-BIC metasurfaces with (from the left to right inside the box) the symmetric (Bravais lattice) array, position-detuned (non- Bravais lattice) array, size-detuned (non- Bravais lattice) array and doubly-detuned (non- Bravais lattice) array, respectively [39]. ©2018 American Physical Society. ©2022 John Wiley & Sons, Inc.

resonances with zero spectral linewidth, *i.e.*, infinitely large Q-factors. Such lossless modes are called symmetry-protected bound states in the continuum (BICs) [38].

In reality, since such dark modes cannot be coupled to a system through absorption and radiation, no true BIC resonances can be excited in a practice. Nevertheless, by coupling the localized in-phase bright modes and the out-of-phase dark modes, one can excite spectrally asymmetric Fano resonances in contrast to the Lorentz-like spectrally symmetric localized resonances. In such a way, resonant coupling can suppress the overall localized radiative loss; hence, the corresponding spectral asymmetric lineshape originated in between the dipole- and quadrupole-like oscillations typically has a relatively narrow linewidth, which corresponds to relatively high-Q-factor Fano resonances. Due to the presence of the BIC dark modes in such low-loss high-Q Fano resonances, the resonantly coupled finite narrow-linewidth hybrid modes are also called quasi-BIC modes [38]. To introduce such modes locally in the nanostructures, one may either need to break the geometrical symmetry of the individual nanostructures to create an intra-nanostructure near-field coupling, or to bring more than one nanostructures in a close proximity to create an inter-structure near-field coupling, as shown in Fig. 1.6(a) [38]. Due to the nature of the symmetry-broken structures, such quasi-BIC modes are called the symmetry-broken quasi-BICs. Fig. 1.6(b) shows the transformation of the BIC modes into the quasi-BIC modes due to the transformation of the symmetric structures into the assymetric structures [38].

Quasi-BIC Lattice Resonances

Apart from the bright SLR modes, it is also possible to excite the so-called quasi-BIC resonant modes in a periodic metasurface either by breaking the symmetry of the individual meta-atom nanostructures' geometry or forming the individual meta-molecule unit cells comprising asymmetrically organized nanostructures in symmetrically periodic metasurfaces (*e.g.*, square, rectangular, honeycomb lattice formations, *etc.*; also known as Bravais lattices), or by breaking the symmetry of the periodicity itself (non-Bravais lattices), as shown in Fig. 1.6 [39].

1.2.3 Resonant Waveguide Gratings

So far, we have briefly discussed different types of localized and delocalized resonances which can be excited in the flat-optics platforms using meta-atoms and metasurfaces. While the localized resonances can confine light only near the individual meta-atom structures, the delocalized resonances can trap light in the 2D areas spread across the planar metasurfaces. Furthermore, one can also trap light in the thin films of optical materials by integrating them with resonant metasurfaces. In this case, a thin film-metasurface duo forms a resonant waveguide grating structure, where the metasurface serves as a diffraction grating, as shown in Fig. 1.7(a). Such gratings can couple free-space light into the thin films made of the materials with the refractive indices higher than those of the free space and the host substrates. The coupled light then undergoes total internal reflection repeatedly inside the thin films, thereby creating resonances at the desired wavelengths, which depend on the angle of incidence θ and the free-space wavelength λ of the transverse electric (TE) or transverse magnetic (TM) incident light, the metasurface grating elements' size (for example, height d), shape, lattice formation and periodicity Λ alongside the thin-film thickness t and its refractive index n_{W} as depicted in Fig. 1.7(a). Such resonances are called guided-mode resonances (GMRs) due to the high-index thin-film media acting like slab waveguides. Characteristically, they are similar to the Fabry-Pérot resonances [41]. Fig. 1.7(b) shows an example of the dependency of the resonance

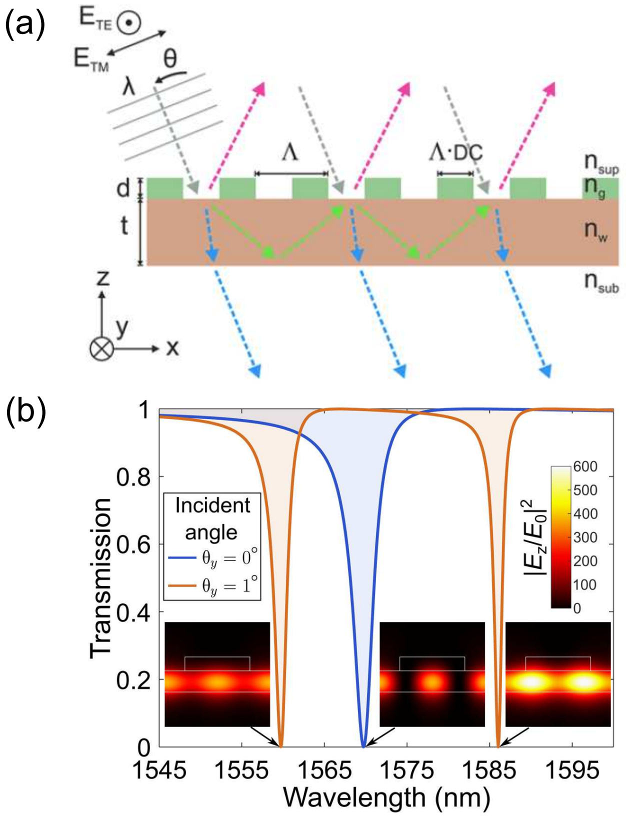

FIGURE 1.7: (a) Illustration of a standard resonant waveguide gratings (RWGs) allowing a complete destructive interference of the propagating light in transmission at a specific angle of incidence and wavelength [41]. (b) Simulated transmission spectra of a glass nanostrips-integrated lithium niobate on-insulator thin film RWG metasurface, which depicts a single guided mode resonance (GMR) for a normal incident light and two GMRs for the light with a nonzero incident angle. The field intensity maps in the insets show strong field enhancement in the thin-film layer. ©2018 John Wiley & Sons, Inc. ©2018 American Association for the Advancement of Science.

position of the GMR transmission spectra on the incidence angle in a GMR metasurface, whereas the insets demonstrate the corresponding large field enhancement inside the metasurface [42].

1.3 Motivation and Objective of the Thesis

1.3.1 Motivation

Metasurface-integrated flat optical materials, which can act as the passive and active optical components for a diverse range of practical applications, are getting their popularity as flat meta-optics. Such structured flat optical components promise to miniaturize and flatten the overall size and shape of devices where they are to be integrated. Due to their compact size and reduced weight, the flat meta-optics-based devices are gradually replacing the traditional bulk optical devices in different applications. One of the examples of the applications that already finds its place in the commercial productions is the metalens [43], which has the ability to diffract, focus and polarize the free-space light within an ultra-thin subwavelength region [44]–[50]. Other applications of the flat meta-optics include the sensors, imaging cameras, detectors, and LiDARs, *etc*, which are currently of growing demand in the big markets for commercial, research and military usage [51], [52]. The list of implementations ranges from biomedical instruments to telecommunication systems to automobile systems, security and surveillance systems to our everyday portable devices, *e.g.*, smartphones, smart headsets and eyewear supporting augmented and virtual reality (AR/VR) [19], [53].

Nonlinear Electro- and All-Optical Modulations

The common functionalities of the flat meta-optics include the modulation and detection of light. Thus, they need to be made using the dielectric or semiconductor materials which have the ability to modulate and detect light characteristics. The light modulation techniques typically involve electro- or all-optical modulation processes, which are governed by the Pockel electro-optical and Kerr nonlinear optical effects. Such effects depend on the materials that naturally exhibit second- and third-order nonlinear optical susceptibilities, $\chi^{(2)}$ and $\chi^{(3)}$, respectively. One of the materials that possesses both strong $\chi^{(2)}$ and $\chi^{(3)}$ is lithium niobate ($LiNbO_3$) [54]. Nevertheless, comparing to the bulk crystalline versions, light matter-interaction within the thin-film versions of the materials including $LiNbO_3$ is relatively weak due to the lack of the required nonlinear interaction length and phase-matching. Thus, it is essential to excite resonances inside the thin films with high Q-factors to relax the phase-matching conditions [55]–[58].

Light Absorption for Photodetection

For the light detection purposes, semiconductor materials are the champion over all other materials that can be used in fabricating photodiodes. Semiconductor photodiodes can absorb the incident photons and convert them into the electrical signal by creating electron-hole pairs in their p-n junction regions. Such processes are typically characterized by two parameters: responsivity and quantum efficiency (Q.E.) of the photodiodes, which depend on the efficiency of photon absorbtion and photocurrent generation. Regarding the choice of materials to determine the spectral dependency of the photodiodes, Silicon (Si) is the best choice for absorbing light in the visible and near-infrared spectral range (300 nm to 900 nm), while indium gallium arsenide phosphate (InGaAs) remains unbeatable for absorbing light in the short-wavelength infrared (SWIR) spectral regime (900 nm to 1700 nm). Typically, an InGaAs thin-film absorber layer is grown on a lattice-matched indium phosphide (InP) substrate [1], [59], [60].

There exist spectral regions which still lack the suitable natural materials that can make a base for efficient photodiodes. One of such spectral ranges that represent challenge for detection techniques is beyond 1700 nm and up to 2400 nm in near-IR, which is known as the extended SWIR regime. Photodetection in the extended SWIR band could be beneficial for the imaging and LiDAR operations in foggy weather, or imaging through smoke or in dark environment. Also, light in the extended SWIR regime is beneficial for eye safety. Due to its energy bandgap limit, InGaAs cannot naturally absorb photons beyond 1700 nm. One can extend the energy bandgap by producing indium-enriched InGaAs. However, In-rich InGaAs is lattice-mismatched with respect to InP, which severely reduces the signal-to-noise ratio (SNR) of the resulting detectors. Another technique for extended-SWIR photodetection could be the use of InGaAs quantum dots to manipulate the energy gap via the intraband transition process, however, that technique comes with a cost of cooling down the device significantly below the room temperature using an expensive and bulky cooling system [61]–[63].

1.3.2 Thesis Objective

Recently, high-*Q* quasi-BIC and GMRs-based dielectric metasurfaces have been demonstrated for efficient free-space light manipulation [12], [14], [15], [41], [64], such as, beam-steering [56], [57], nonlinear harmonic generation [58], [65], quantum entangled photon-pair generation [66], [67], and biosensing [68], [69]. Nonetheless, there still exists the opportunity for improving the efficiency of such processes by maximizing the resonance *Q*-factors and other performance aspects, for example, the multiresonant features.

In parallel, SLRs-based plasmonic metasurfaces have recently demonstrated their potentials and promises in many applications, including nonlinear harmonic generation, nanolasing and imaging. However, the experimentally reported *Q*-factors of plasmonic SLRs did not exceed 10^2, although their theoretically predicted values exceeded 10^3 [21].

Motivated by these existing challenges, in this thesis, we design plasmonic metasurfaces for controlling the characteristics of the SLRs and GMRs, such as the *Q*-factor, polarization dependency, and ability to excite multiple lattice resonances inside the flat optical media. To fulfill our objective, We investigate the interaction of the resonant lattice modes with different types of optical media including transparent, nonlinear and absorptive materials.

1.4 Outline of the Thesis

Apart from this introductory chapter 1, this thesis contains five additional chapters (Chapter 2 to Chapter 6) describing five different projects and followed by Chapter 7 as the concluding chapter. All these chapters and thesis projects are interrelated and represent milestones of the thesis objectives, as specified above. The following five chapters sequentially tell the story of 'resonating' journey of a series of repeated success, failure, climax and again success in our work towards achieving the thesis objectives.

In Chapter 2, we present the experimental observation of the SHG response of the metasurfaces consisting of plasmonic meta-atomic nanoparticles. The project was initially launched during my Master's program, when our primary focus was to develop an analytical nonlinear *RLC* model to estimate hyperpolarizability of the individual nanoparticles which exhibit low-Q LSPRs [70]. Nevertheless, in the very early stage of my Ph.D. program, we experimentally observed that nonlocal high-Q SLRs can significantly enhance the SHG response. Such an important observation, that was included in the **Supporting Information** attached at the end of Chapter 2, ignited our interest in analysing and improving the SLR Q-factors in the following chapters.

In Chapter 3, we present the experimental manifestation of an ultra-high-Q SLR in a plasmonic metasurface operating near 1550 nm telecom wavelength. Following the theoretical predictions, we experimentally realize metasurfaces featuring plasmonic SLRs with Q-factors on the orders of 10^3, reaching a nearly two-decade-long goal pursued by the research community. Earlier experimental efforts at the realization of high-Q SLRs were not very successful due to the lack of optimal design, fabrication and characterization processes. We thoroughly investigated and optimized each process, which ultimately lead us to observe plasmonic SLR with the record-high Q-factor around 2,340.

After discovering the techniques of generating high-Q SLRs discussed in Chapter 3, we set the goal of exciting multiple SLRs at different wavelengths which are expected to match the fundamental and second-harmonic (SH) wavelengths in the SHG process. Such an investigation, particularly for the applications involving more than one spectral wavelength regions, is paramount for achieving high-efficiency SHG facilitated by SLRs. Thus, in Chapter 4, we experimentally demonstrate a polarization-controlled dual-SLR metasurface by manipulating the dimension parameters and the periodicity of a 2D lattice of 'V'-shaped nanoparticles. In this work, we successfully excite two periodicity-dependent SLRs alongside two geometry-dependent LSPRs, where one ultra-high-Q SLR is excited in the infrared and another low-Q SLR is excited in the visible wavelength range. This experimental work serves an important step towards the experimental demonstration of SHG enhancement by SLRs at both the fundamental and SH wavelengths.

While working on the projects discussed in Chapter 3 and Chapter 4, we needed to ensure that the surrounding media of the metasurface nanoparticles arrays are homogeneous; in other words, the refractive index surrounding the nanoparticles should be uniform to excite the SLRs by a light illuminating the array at normal incidence. Although one can create such a system in the lab environment by covering the nanoparticles fabricated on a fused silica glass substrate by a glass microscope cover slip using a commercially available refractive-index-matching oil, such a system is often not user-friendly for practical applications. To eliminate this issue, we decided to replace the cover slip-index matching oil duo by a permanent ultra-thin fused silica layer deposited on the substrate by thermal evaporation technique. Nevertheless, we could deposit such a cladding layer only with a thickness on the order of the wavelength of light (*i.e.*, on the order of a micrometer). Surprisingly, such a thin-film cladding layer of material with the refractive index matching that of the substrate exhibited multiple additional narrow resonances alongside the SLR. We explored the nature of this observation by performing numerical simulations. In Chapter 5, we report and analyze the results, which eventually lead us to realize that such additional resonances are created by the out-of-plane lattice modes trapped inside the cladding layer. Such out-of-plane modes are collectively scattered by the periodic nanoparticles and then repeatedly undergo the total internal reflection within the thin-film cladding layer at the air-dielectric interface. Thus, those lattice-controlled out-of-plane modes create multiple Fabry-Pérot-like guided-wave narrow resonances. In addition, due to the overlapping with the LSPRs, such out-of-plane lattice resonances could also suppress the scattering losses of the individual metal nanoparticles corresponding to the LSPRs. The resulting quality factors of these resonances are considerably higher compared to the typical Q-factor values for ordinary LSPRs.

As already mentioned above, our ultimate goal is to excite multiple high-Q resonances by coupling free-space light into flat nonlinear, electro-optic and absorptive materials. The results discussed in Chapter 5, which is coincidentally obtained using a plasmonic metasurface embedded in a homogeneous glass medium, open a great opportunity to explore similar features in other types of media. Nevertheless, unlike the case with glasses, it is not possible to deposit same-index material layers on top of many useful dielectric and semiconductor materials. As we mentioned earlier, such index-matching is required to excite SLRs at a normal incidence. To overcome this bottleneck, in one of the projects described in Chapter 6, we adopt the concept of lattice diffraction grating-coupled GMRs in flat optical thin films. Here, instead of covering the nanoparticles array by a thin-film cladding layer, we place the nanoparticles array on top of a high-refractive-index lithium niobate thin film. We design in such a manner a metasurface-integrated lithium niobate thin film-on-insulator flat optical system, such that multiple out-of-plane lattice modes-controlled ultra-high-Q GMRs spanning infrared-to-visible octave-band can be excited. Here, we choose lithium niobate since, as already mentioned earlier in the previous section, it is a broadly transparent highly nonlinear medium with a strong electro-optic effect.

The results obtained in the first project in Chapter 6 also inspired us to explore the potentiality of lattice-controlled GMRs in a different thin-film material platform for a different application. In particular, we explored a photon absorption enhancement process inside thin-film semiconductor absorber layers in photodiodes in extended-SWIR regime. Thus, in another project described in Chapter 6, we enhance the light absorption within an InGaAs quantum-dot photodetector diode operating around 1900 nm within extended-SWIR band by exploiting the lattice-controlled guided modes using a plasmonic metasurface diffraction grating.

Finally, we draw the conclusion of our research contributions in Chapter 7 by discussing the challenges and obstacles we meet in each project which yet require to be solved. Last but not least, we briefly discuss the possibility of future research that could be conducted based on the progress demonstrated in this Ph.D. dissertation. We believe that design improvement and practical implementation of the metasurfaces demonstrated in this thesis could dramatically boost up the field intensity in a nonlinear dielectric medium and absorption inside a semiconductor absorber flat-optical systems used for electro-optical and all-optical modulation, frequency-mixing and conversion, entangled photon pair generation, photodetection and imaging in free-space communications and biomedical systems.

Chapter 2

Nonlinear Plasmonic Meta-Atoms and Metasurfaces

2.1 Summary

Although the primary focus of this chapter was to analyze the microscopic nonlinear optical response of plasmonic nanoparticles in a metasurface environment, at the end, it contains an exciting result that was ultimately turned into the main motivation of the whole thesis.

Primarily, in this project we theoretically and experimentally determined the second-order nonlinear response, *i.e.* hyperpolarizability of individual plasmonic meta-atom nanoparticles. At first, we performed a second-harmonic generation (SHG) experiment in a metasurface consisting of randomly organized but identically oriented elongated nanoprism gold meta-atoms, from which we extracted the hyperpolarizability of the individual meta-atoms. Next, we analytically derived a formula to estimate the hyperpolarizability based on the RLC equivalent-circuit model of the localized surface plasmon resonances (LSPRs) associated with the individual plasmonic nanoparticles. While both the experimental and analytical hyperpolarizabilities agreed well, our collaborator Prof. Lora Ramunno and Dr. Mikko J. Huttunen's gr plasma m and nonlinear scattering theory-based simulations.

Nevertheless, this project became an interesting work when we repeated the SHG experiment on the periodically organized plasmonic meta-atoms. Such organization led to excite nonlocalized surface lattice resonances (SLRs) close to the LSPRs with relatively narrow linewidth (*i.e.*, high-Q-factors). The excited SLRs significantly enhance the SHG response minimum by one to two orders of magnitude, as reported in the **Supporting Information**. This exciting result ultimately sparked our curiosity for investigating the nature of the high-Q SLRs in the metasurface platforms in the following chapters.

2.2 Contribution

The results provided in this chapter have been published in *Nano Letters* [71]. In this project that is a brainchild of Prof. Ksenia Dolgaleva, as per the suggestion of Prof. Kosmas L. Tsakmakidis, I treated the individual meta-atom as an *RLC* circuit to predict its nonlinear optical response, and thus developed the analytical nonlinear *RLC* model for a plasmonic structured meta-atoms. To support my analytical model, I also performed linear simulation using Lumerical software, based on which Dr. Kashif M. Awan fabricated a metasurface. As a part of the collaboration, I went to Finland to work with Dr. Mikko J. Huttunen and Dr. Antti Kiviniemi to carry out the measurements at Tampere University. Mr. Joshua Baxter performed the linear and nonlinear hydrodynamic-FDTD model simulations. Mr. Joshua Baxter and Prof. Lora Ramunno derived an expression for the nonlinear coefficient a using intuitive physical arguments. Ms. Yaryna Mamchur prepared an illustration for the journal article. Last but not least, Prof. Ksenia Dolgaleva, Prof. Lora Ramunno, Dr. Mikko J. Huttunen, Prof. Kosmas L. Tsakmakidis, and Prof. Antonio Calà Lesina supervised the research and the development of the manuscript. Dr. Mikko J. Huttunen, Mr. Joshua Baxter, and I wrote the first draft of the manuscript. All coauthors subsequently took part in the revision process and approved the final copy of the manuscript.

2.3 Article

The published article follows verbatim.

NANO LETTERS

pubs.acs.org/NanoLett Letter

Hyperpolarizability of Plasmonic Meta-Atoms in Metasurfaces

M. Saad Bin-Alam, Joshua Baxter, Kashif M. Awan, Antti Kiviniemi, Yaryna Mamchur, Antonio Calà Lesina, Kosmas L. Tsakmakidis, Mikko J. Huttunen, Lora Ramunno, and Ksenia Dolgaleva*

Cite This: *Nano Lett.* 2021, 21, 51−59 Read Online

ACCESS | Metrics & More | Article Recommendations | SI Supporting Information

ABSTRACT: Plasmonic metasurfaces are promising as enablers of nanoscale nonlinear optics and flat nonlinear optical components. Nonlinear optical responses of such metasurfaces are determined by the nonlinear optical properties of individual plasmonic meta-atoms. Unfortunately, no simple methods exist to determine the nonlinear optical properties (hyperpolarizabilities) of the meta-atoms hindering the design of nonlinear metasurfaces. Here, we develop the equivalent *RLC* circuit (resistor, inductor, capacitor) model of such meta-atoms to estimate their second-order nonlinear optical properties, that is, the first-order hyperpolarizability in the optical spectral range. In parallel, we extract from second-harmonic generation experiments the first-order hyperpolarizabilities of individual meta-atoms consisting of asymmetrically shaped (elongated) plasmonic nanoprisms, verified with detailed calculations using both nonlinear hydrodynamic-FDTD and nonlinear scattering theory. All three approaches, analytical, experimental, and computational, yield results that agree very well. Our empirical *RLC* model can thus be used as a simple tool to enable an efficient design of nonlinear plasmonic metasurfaces.

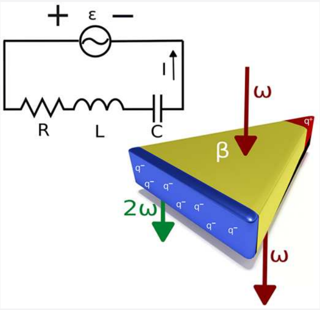

KEYWORDS: *Plasmonics, Meta-atoms, Nonlinear Optics, Hyperpolarizability, Anharmonic RLC oscillator*

Photonic metamaterials are artificial structures exhibiting optical properties that in natural materials are either very weak or entirely lacking. Among these properties are phase mismatched light-propagation, optical magnetism, strong chirality, and epsilon-near-zero behavior.[1−5] There is a growing interest in understanding and harnessing the nonlinear optical responses of metasurfaces.[6−14] Many photonic applications including frequency conversion, THz generation, photon-pair generation, ultrashort-pulse generation, frequency-comb generation, and all-optical switching[15−19] rely on nonlinear optics occurring in large bulky devices where one must contend with phase mismatching. In contrast, the small footprint of metasurfaces virtually guarantees phase matching, and moreover, the nonlinear emission can be precisely controlled.[2,3,20,21]

Plasmonic metasurfaces have recently emerged as a promising candidate for enabling nanoscale nonlinear optics.[6] The optical responses of plasmonic meta-atoms serving as unit cells of metasurfaces are dictated by the collective movement of the conduction electrons giving rise to localized surface plasmons (LSPs). Therefore, it is imperative to investigate the conduction electron dynamics and the nonlinear response of the constituting meta-atoms. Such investigations can be performed, for example, by using the hydrodynamic plasma model[22−25] and the nonlinear scattering theory.[26] However, relying on computational tools is not always convenient due to their complexity and the large amount of computational resources they often require.

Linear and nonlinear optical responses of plasmonic meta-atoms can also be predicted by equivalent *RLC* circuit (resistor, inductor, capacitor) theory.[27−31] This approach has correctly described the nonlinear and magnetic responses of split-ring resonators operating at microwave frequencies.[32] Nevertheless, it remained unclear whether the *RLC* approach could describe conduction electron dynamics in plasmonic meta-atoms adequately enough to accurately predict their nonlinear responses at optical wavelengths as well. In this Letter, we derive the first-order hyperpolarizability of individual plasmonic meta-atoms by adapting the equivalent *RLC* model that we find can, indeed, be used to predict collective second-order nonlinear responses of large metasurfaces. First, we derive an expression for the first-order hyperpolarizability with an unknown nonlinear coefficient a that represents the strength of the nonlinear charge oscillation in an individual meta-atom. Our goal is to determine the value of a through physical arguments and to validate our approach through rigorous experiments and numerical calculations. Next, we describe our second-harmonic generation (SHG) experiments, where we measured SHG emission from metasurfaces consisting of randomly arranged gold elongated nanoprisms. From these measurements, we extract the

Received: July 21, 2020
Revised: December 17, 2020
Published: December 24, 2020

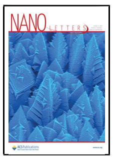

https://dx.doi.org/10.1021/acs.nanolett.0c02991
Nano Lett. 2021, 21, 51−59

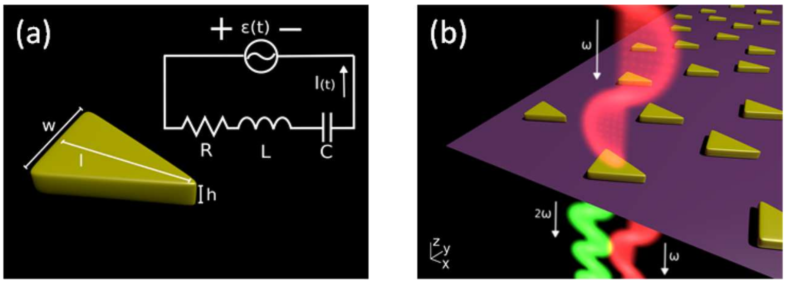

Figure 1. An artist's depiction of (a) an equivalent *RLC* circuit diagram for the investigated nanoprisms, and (b) metasurface consisting of a random array of elongated gold nanoprisms.

spectrum of their first-order hyperpolarizability. This result is then validated by two sets of finite-difference time domain (FDTD) calculations. In the first, the material nonlinearities are directly implemented within the code via a nonlinear hydrodynamic plasma model. The second is based on nonlinear scattering theory where the experimentally determined second-order nonlinear permittivity of gold is used.

Finally, we present a simple empirical derivation for the unknown *RLC*-model nonlinear coefficient a, which we then use to perform an order-of-magnitude estimate of the first-order hyperpolarizability. Our intuitive physical interpretation of a is such that the *RLC* circuit model we present can be extended to describe metasurfaces with different meta-atoms without requiring a priori experimental validation. This simple analytical tool, capable of predicting the hyperpolarizabilities of meta-atoms based on their shapes, dimensions, and material compositions, will prove indispensable in the realization of metasurfaces with tailored nonlinear optical responses.

Because of its resonant nature, a plasmonic meta-atom behaves as an *RLC* circuit, illustrated in Figure 1a, whose dynamics can be described via[32]

$$L\dot{\tilde{I}} + R\tilde{I} + \tilde{V}_{\mathrm{C}}(\tilde{q}) = \tilde{\varepsilon}(t) \tag{1}$$

where $\tilde{I}$ is the free charge current, L is the distributed inductance, R is the distributed resistance, and $\tilde{V}_{\mathrm{C}}$ is the induced voltage due to the effective capacitance C of the circuit. We use a tilde to represent time-varying quantities and an overdot to represent time derivatives.

The free charges of a rodlike plasmonic meta-atom, in the presence of an incident field $\tilde{E}_{\mathrm{inc}} = E_0 \exp(-i\omega t)$ polarized along its length l, will accumulate at a facet resulting in a charge separation and an effective capacitance C. The incident field drives the *RLC* circuit by creating an electromotive force, which in the dipole approximation, takes the form $\tilde{\varepsilon} = \tilde{E}_{\mathrm{inc}}l$. The dynamics of the free charge is described by the current $\dot{\tilde{q}} = \tilde{I}$, where $\pm q$ is the induced charge at opposing facets of the nanostructure. We assume that the nonlinearity is sufficiently weak, allowing us to write the nonlinear voltage as[32]

$$V_{\mathrm{C}}(\tilde{q}) = (\tilde{q} + a\tilde{q}^2)/C \tag{2}$$

where a quantifies the strength of the nonlinearity. Note that the nonlinear perturbation we assumed here is valid at least up to ~10 GW/cm^2 incident field intensities.[33] Inserting these expressions into eq 1, we obtain

$$\ddot{\tilde{q}} + 2\gamma\dot{\tilde{q}} + \omega_0^2\tilde{q} + a\omega_0^2\tilde{q}^2 = C\omega_0^2 l\tilde{E}_{\mathrm{inc}} \tag{3}$$

where $\omega_0 = 1/\sqrt{LC}$ is the resonance frequency of the circuit and $\gamma = R/2L$ is the free-electron damping constant of metals.[32] This model accounts for the dispersive nature of metals by implicitly considering a Drude model with γ in eq 3 and ω_{p} in eq 10b which are given for gold in Methods.[32] The *RLC* model is valid in the same wavelength ranges as the Drude model. Typically for plasmonics, this is when the pump wavelength is in the infrared.

When the excitation wavelengths are close to the LSP resonance of the meta-atom, the conduction electron dynamics are well described using the *RLC* approach.[28] A steady-state solution to eq 3 is found by implementing perturbation theory[34]

$$\tilde{q} = \frac{C\omega_0^2 l}{D(\omega)}E_{\mathrm{inc}}\mathrm{e}^{-i\omega t} - \frac{aC^2\omega_0^6 l^2}{D^2(\omega)D(2\omega)}E_{\mathrm{inc}}^2\mathrm{e}^{-i2\omega t} \tag{4}$$

where $D(\omega') = (\omega_0^2 - \omega'^2 - 2i\gamma\omega')$. We write the total induced dipole moment as $\tilde{p} = \tilde{q}l$, and recall that the dipole moment can be expressed in the frequency domain as[34]

$$p = \epsilon_0\alpha E_{\mathrm{inc}} + \epsilon_0\beta E_{\mathrm{inc}}^2 \tag{5}$$

where α is the linear polarizability and β is the first-order hyperpolarizability of the meta-atom. Combining eqs 4 and 5, we obtain

$$\alpha(\omega) = -\frac{C\omega_0^2 l^2}{\epsilon_0 D(\omega)} \tag{6a}$$

$$\beta(2\omega;\, \omega) = -a\frac{C^2\omega_0^6 l^3}{\epsilon_0 D(2\omega)D^2(\omega)} \tag{6b}$$

As the lengths of the meta-atoms can be a significant fraction of the exciting wavelength, higher-order multipoles can be excited, and one must consider this possibility in general, especially for nonlinear emission at shorter wavelengths.[35] However, in this study our goal is to create a model that gives an order of magnitude estimate of SHG emission, and we therefore consider only the electric dipole term. The hyperpolarizability in eq 6b can be considered an "effective" hyperpolarizability that helps us to achieve this goal. In what follows, we use experimentally and computationally derived hyperpolarizability spectra to determine a quantitative value for the nonlinear coefficient a.

We first need to consider a geometry for our meta-atom. SHG is a coherent second-order nonlinear process, and therefore, very sensitive to the symmetry of the object under investigation.[34] In fact, centrosymmetric-shaped structures exhibit very weak electric-dipole SHG responses[36] (see also Figure S1 in Supporting Information Section S1). Nanostructures with low symmetry, such as split-ring resonators, L-

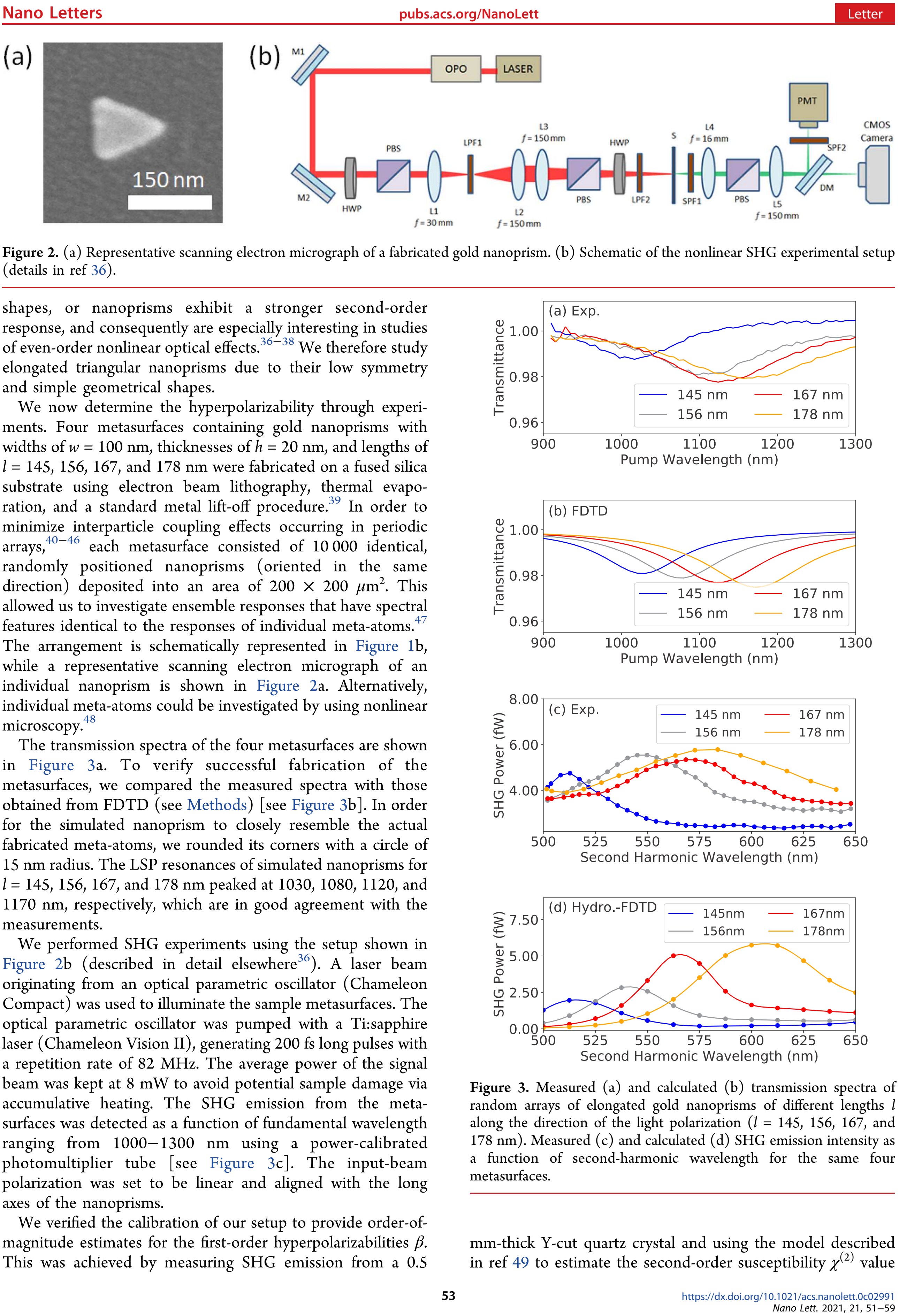

Figure 2. (a) Representative scanning electron micrograph of a fabricated gold nanoprism. (b) Schematic of the nonlinear SHG experimental setup (details in ref 36).

shapes, or nanoprisms exhibit a stronger second-order response, and consequently are especially interesting in studies of even-order nonlinear optical effects.[36−38] We therefore study elongated triangular nanoprisms due to their low symmetry and simple geometrical shapes.

We now determine the hyperpolarizability through experiments. Four metasurfaces containing gold nanoprisms with widths of w = 100 nm, thicknesses of h = 20 nm, and lengths of l = 145, 156, 167, and 178 nm were fabricated on a fused silica substrate using electron beam lithography, thermal evaporation, and a standard metal lift-off procedure.[39] In order to minimize interparticle coupling effects occurring in periodic arrays,[40−46] each metasurface consisted of 10 000 identical, randomly positioned nanoprisms (oriented in the same direction) deposited into an area of 200 × 200 μm^2. This allowed us to investigate ensemble responses that have spectral features identical to the responses of individual meta-atoms.[47] The arrangement is schematically represented in Figure 1b, while a representative scanning electron micrograph of an individual nanoprism is shown in Figure 2a. Alternatively, individual meta-atoms could be investigated by using nonlinear microscopy.[48]

The transmission spectra of the four metasurfaces are shown in Figure 3a. To verify successful fabrication of the metasurfaces, we compared the measured spectra with those obtained from FDTD (see Methods) [see Figure 3b]. In order for the simulated nanoprism to closely resemble the actual fabricated meta-atoms, we rounded its corners with a circle of 15 nm radius. The LSP resonances of simulated nanoprisms for l = 145, 156, 167, and 178 nm peaked at 1030, 1080, 1120, and 1170 nm, respectively, which are in good agreement with the measurements.

We performed SHG experiments using the setup shown in Figure 2b (described in detail elsewhere[36]). A laser beam originating from an optical parametric oscillator (Chameleon Compact) was used to illuminate the sample metasurfaces. The optical parametric oscillator was pumped with a Ti:sapphire laser (Chameleon Vision II), generating 200 fs long pulses with a repetition rate of 82 MHz. The average power of the signal beam was kept at 8 mW to avoid potential sample damage via accumulative heating. The SHG emission from the metasurfaces was detected as a function of fundamental wavelength ranging from 1000−1300 nm using a power-calibrated photomultiplier tube [see Figure 3c]. The input-beam polarization was set to be linear and aligned with the long axes of the nanoprisms.

We verified the calibration of our setup to provide order-of-magnitude estimates for the first-order hyperpolarizabilities β. This was achieved by measuring SHG emission from a 0.5 mm-thick Y-cut quartz crystal and using the model described in ref 49 to estimate the second-order susceptibility $\chi^{(2)}$ value

Figure 3. Measured (a) and calculated (b) transmission spectra of random arrays of elongated gold nanoprisms of different lengths l along the direction of the light polarization (l = 145, 156, 167, and 178 nm). Measured (c) and calculated (d) SHG emission intensity as a function of second-harmonic wavelength for the same four metasurfaces.

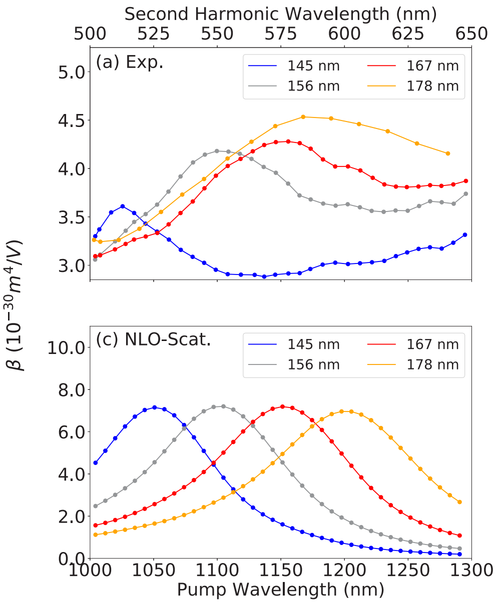

Figure 4. (a) Experimentally extracted values of β for the investigated nanoprism samples. Corresponding values of β, predicted by (b) hydrodynamic-FDTD, (c) nonlinear scattering theory, and (d) the introduced nonlinear *RLC* model.

for the quartz crystal. Our estimate ($\chi^{(2)}_{xxx} = 0.53$ pm/V) is in excellent agreement with the literature.[34]

To estimate the values of β for the nanoprisms from the experimental data, we calculated the macroscopic $\chi^{(2)}$ using the same approach as we used for quartz.[49] We estimated the meta-atom number density of the metasurfaces to be $n = 10\,000/(200\ \mu\text{m} \times 200\ \mu\text{m} \times 20\ \text{nm}) = 1.25 \times 10^{19}\ \text{m}^{-3}$, then linked the detected SHG intensities to the hyperpolarizabilities using the relation $\beta = \chi^{(2)}/n$. The extracted values of β as a function of the incident fundamental wavelength are plotted for the four investigated nanoprisms in Figure 4a.

Next we wish to determine the hyperpolarizability using numerical computations via the hydrodynamic plasma model.[22−25] This was used in conjunction with the two-critical-points model[50] for gold in an in-house 3D-FDTD code.[51] As the metasurface contains randomly positioned nanoprisms, periodic boundary conditions could not be used to simplify the calculation. Further, the metasurfaces were too large for a single FDTD simulation. We therefore developed a new method for quantitative approximation of the power. First, we calculated the nonlinear scattered power in the forward direction of a single nanoprism resulting from a Gaussian pulse with duration and peak intensity as in the experiments. For each nanoprism in the random metasurface, the forward-scattered power was scaled to the laser field incident on that particular nanoprism. The individual powers from all nanoprisms in the metasurface were then incoherently summed. The calculated second-harmonic power spectrum, shown in Figure 3d shows excellent quantitative agreement with experimental measurements.

To estimate β using the hydrodynamic plasma model, we first calculate the nonlinear scattered power from a single nanoprism by integrating the nonlinear scattering spectrum from a single pulse and multiplying it by the repetition rate of the laser. If the nonlinear scattered power P_{NL} was purely from a dipole, we can approximate the magnitude of nonlinear dipole moment $|p|$ by $|p|^2 = 12\pi P_{\text{NL}}/(nc_0^2 Z_0 k_0^4)$,[52] where c_0 is the speed of light in vacuum, k_0 is the vacuum wavenumber, Z_0 is the vacuum impedance, and n is the refractive index of the surrounding medium. We calculate β using eq 5 and plot it in Figure 4b. One can see excellent quantitative and qualitative agreement between the simulation and experimental results.

Finally we use another numerical approach based on the nonlinear scattering theory[53,54] to determine the nonlinear coefficient a. Though not as rigorous as the hydrodynamic plasma model, it is a simpler and more computationally efficient technique for calculating nonlinear emission from nanostructures. Because the SHG emission was detected only in one direction, and the detector was in the far-field, we were able to use the Lorentz reciprocity theorem.[26,55] First, we obtained the local field distributions for both the fundamental and SHG wavelengths of interest via linear simulations. The excitation field was assumed to be a normally incident plane wave polarized along the long axis of the nanoprism. The dimensions of the simulated nanoprism were matched with the experimental values, and the sharp corners of the meta-atoms were again rounded.

Then we calculated the generated nonlinear source polarization present on the surface of the meta-atom, where we used the experimentally extracted local nonlinear susceptibility values for gold.[56] The local field was transformed into the surface coordinate system by reconstructing the surface of the meta-atom by using a Delaunay triangulation mesh and performing subsequent field interpolation onto that surface. Once the nonlinear surface polarization was calculated, we used the Lorentz reciprocity theorem to predict the emitted SHG field from the meta-atom (in the forward direction) by calculating the mode overlap integral between the SHG source polarization and the local field distribution at the SHG wavelength.[26,57] The last step was to use eq 5 to calculate β. The values of β are plotted in Figure 4c and agree in resonance position and in the order-of-magnitude values with the experimental and hydrodynamic plasma model results.

Now that we have obtained agreement for the values of β from the experimental data and the two numerical approaches, we can estimate the value of the nonlinear coefficient a

required for the *RLC* model from eq 6b. We find that $a \approx 10^{14}$ C^{-1}, and plot eq 6b, our *RLC* model prediction, in Figure 4d.

While we are confident in the order of magnitude of a, it was quite labor intensive to obtain. We now present a physically intuitive explanation for the order of magnitude of a that we have obtained. In the discussion surrounding Miller's rule presented by Boyd,[34] it is argued that for a bulk material, the linear and nonlinear restoring forces felt by an electron are comparable in magnitude when the charge displacement is approximately equal to the interatomic spacing d. This is then used to estimate the strength of the nonlinear restoring force.

In contrast, the polarization of a meta-atom results from an accumulation of free charge on the surface. The charge buildup occurs at the facet within a thin layer with thickness on the order of the Fermi wavelength ($\lambda_F \approx 0.5$ nm for gold). In the absence of external fields, the density of free electrons in this layer would be n_0, the equilibrium free electron density, and thus there is no excess charge at the surface.

In the presence of an external field, it is reasonable to assume that at most two electrons (with different spins) can reside within λ_F of each other. This would lead to a surface charge density of

$$\sigma \approx \pm e n_0 \lambda_F \tag{7}$$

where the sign depends on which side of the meta-atom is being considered. Under this condition one would expect the linear and nonlinear responses to be comparable, in a similar spirit to ref 34; in fact, $\lambda_F \approx d$, the interatomic spacing in gold. From eq 2, the linear and nonlinear terms of V_C are equal when $\tilde{q} = a\tilde{q}^2$, giving $a = 1/\tilde{q}$, where $\tilde{q} = \sigma A$ and A is the surface area containing σ on one side of the meta-atom.

For the nanoprisms considered in this paper, our simulations showed that the region over which there is significant charge density covers a perimeter of approximately 100 nm both at the tip end and at the base end. Given the height of the nanoprism is 20 nm, we obtain

$$a = \frac{1}{e n_0 A \lambda_F} = 1.1 \times 10^{14}\ \mathrm{C}^{-1} \tag{8}$$

where $n_0 = 5.9 \times 10^{28}$ m^{-3} in gold. This is remarkably close to what the detailed simulations and measurements predict.

It is also worth mentioning that from the *RLC* model we can obtain the ratio

$$\frac{\beta(2\omega, \omega)}{\alpha^2(\omega)\alpha(2\omega)} = \frac{a\varepsilon_0^2}{Cl^3} \tag{9}$$

which is, in essence, a form of Miller's rule for meta-atoms. It is frequency independent and only depends on the geometry of the particle. This is similar to the anharmonic oscillator model of ref 34 where the ratios of the susceptibility functions are also only dependent on the effective mass and the number density of the electrons.

From Figure 4, we see that all four approaches yield values of β within the same order of magnitude $\sim 10^{-30}$ m^4/V. This agreement is very encouraging because it has been notoriously difficult to make quantitative predictions of nonlinear optical processes occurring in plasmonic materials.[9,36] The simpler methods (*RLC* and nonlinear scattering theory), though predicting the correct spectral peak positions, are missing some features that are visible in the experimental results and hydrodynamic calculation, such as the oscillations at longer wavelengths. These features are believed to be caused by a secondary resonance of the nanoprisms and interband transitions in gold.

Despite the great amount of previous work on nonlinear metasurfaces, only a handful of investigations have provided order-of-magnitude estimates of meta-atom's hyperpolarizabilities.[35,58−61] Our values of hyperpolarizability are 2−3 orders of magnitude smaller than previous estimates of somewhat similar meta-atoms; this discrepancy is not unexpected, because the experimental setups, the wavelength ranges considered, and the investigated meta-atoms have all been different. While we investigated the coherent SHG emission, earlier investigations measured incoherent hyper-Rayleigh scattering (HRS) signals, and estimated the values of β indirectly by comparing the HRS signals from meta-atoms with HRS signals measured from known solvents. Furthermore, the earlier HRS experiments performed at shorter excitation wavelengths than what we considered. Because the interband transitions of gold start playing a role at wavelengths shorter than 550 nm,[62] these earlier-extracted hyperpolarizability values may have contained an additional contribution arising from the interband transitions.[34]

Our results also demonstrate the usefulness of the nonlinear *RLC* approach. Although simple and intuitive, it describes the dynamics of conduction electrons adequately enough to predict the strength of nonlinear optical responses of plasmonic meta-atoms. Nonlinear *RLC* model had earlier been found to accurately describe nonlinear responses of metamaterials at the microwave wavelengths.[32] We show here that it can be adapted for optical wavelengths as well. This model can also be applied to meta-atoms of any other geometry made of any other plasmonic material, which will be demonstrated in an upcoming publication.

To conclude, we have derived a nonlinear equivalent *RLC* circuit model that can be used to quickly and accurately predict the nonlinear optical responses of meta-atoms in the visible and near-IR spectral ranges. We fabricated four metasurfaces consisting of randomly positioned gold nanoprisms and characterized their second-harmonic generation emissions. We compared the experimental results with the predictions based on the hydrodynamic plasma model, nonlinear scattering theory, and our nonlinear *RLC* model. All of the results were found to be in good agreement. Our *RLC* approach provides new insights into understanding the nonlinear responses of meta-atoms and opens new possibilities for application-oriented efficient nonlinear metasurface design.[36,38,63−66]

■ METHODS

Parameters for the Nonlinear *RLC* Model. In order to find the expressions for the capacitance C and inductance L for an elongated nanoprism [shown in Figure 1a], we first calculated the capacitance C and inductance L of a rectangular nanobar from its geometrical dimensions using the following formulas

$$C = \pi \epsilon_0 \epsilon_r r_0 \tag{10a}$$

$$L = \frac{\mu_0 l}{2\pi} \log \frac{4l}{h} + \frac{\mu_0 l}{\frac{\omega_p^2}{c_0^2} wh} \tag{10b}$$

In eq 10a, the capacitance C can be defined as the electric charge divided by the potential difference between the two facets of a rectangular nanobar (similar to ref 28 for a plasmonic cylindrical nanorod).

To keep similarity with the formula for C given in ref 28, we assumed $r_0 \approx 10^{-9}$ nm in eq 10a as a constant parameter mimicking the radius of a cylinder encircling the nanobar. However, due to the geometrical difference between the cylinder and rectangular nanobar, we slightly modified eq 10b for the inductance L to match the LSPR spectral position with the simulation and experimental linear transmission data.

In eq 10b, the self-inductance is given by

$$L_{\text{self}} = \frac{\mu_0 l}{2\pi} \log \frac{4l}{h} \tag{11}$$

the kinetic inductance is given by

$$L_{\text{kinetic}} = \frac{\mu_0 l}{\frac{\omega_p^2}{c_0^2} wh} \tag{12}$$

ϵ_0 is the vacuum permittivity (8.85×10^{-12} F/m), the relative permittivity of glass is $\epsilon_r \approx 3.9$, μ_0 is the vacuum permeability (1.257×10^{-6} H/m), $\omega_p = 13.8 \times 10^{15}$ rad/s is the plasma frequency for gold in the optical regime,[67] and $c_0 = 3 \times 10^8$ m/s is the speed of light in vacuum.

Simulations. *Linear FDTD Simulations.* Linear FDTD simulations were performed to calculate the linear transmission spectra of the metasurface using an in-house FDTD solver.[51] The spectra were calculated by subtracting the absorption and backscattering cross sections of all the meta-atoms on the metasurface from the total area of the metasurface. The transmission spectrum is then $T = (A_{\text{metasurface}} - (A_{\text{back-scatt}} + A_{\text{abs}}))/A_{\text{metasurface}}$. The cross-sectional data is calculated from a single meta-atom and scaled by the number of meta-atoms on the metasurface. A standard total-field/scattered-field layout is used to calculate the cross sections and the simulation domain is truncated by convolutionaly perfectly matched layers. The linear Drude +2 critical points model[50] is used for the optical properties of gold and accounts for contributions from the conduction electrons and interband transitions. A broadband raised cosine pulse[51] is used as a source excitation.

Hydrodynamic FDTD Simulations. Hydrodynamic FDTD calculations were conducted using the same in-house FDTD solver. The simulation setup is identical to that used in the linear transmission spectra, except that the hydrodynamic model (solved via centered finite differences) replaces the Drude model (in the Drude +2 critical points model), and the source excitation is replaced with a 200 fs Gaussian pulse centered at wavelengths ranging from 1000 to 1300 nm. All simulations using the in-house FDTD solver were run on the Graham cluster operated by Compute Canada.[68]

Nonlinear Scattering Theory. The nonlinear response of a meta-atom was estimated also by using calculations based on the nonlinear scattering theory and the Lorentz reciprocity theorem.[26,57] The strength of the SHG emission in the direction of interest was evaluated by calculating a mode overlap integral over the fundamental excitation and SHG emission modes. The relevant field profiles for the fundamental and SHG fields were calculated using the Lumerical FDTD software, and the mode overlap integrals were calculated numerically using Matlab. In the FDTD simulations the optical constant of gold was taken from ref 67. The fields on the surface of the meta-atom were estimated by using Delaunay triangulation, and only the surface contributions were considered when calculating the nonlinear response of the gold.[56]

Fabrication. We used 2 cm × 2 cm fused silica chips as substrates. The chips were coated with bilayer electron-beam resist, consisting of 50 nm thick PMMA with a molecular weight of 495 k as the bottom layer and 25 nm thick PMMA with a molecular weight of 950 k as the top resist layer. The plasmonic nanostructures were then patterned using 30 kV Raith electron-beam lithography system (CRPuO, uOttawa) with a dose of 550 μC/cm^2. The patterned resist was then developed for 2 min in 3:1 MIBK/IPA (methyl isobutyl ketone/isopropyl alcohol), followed by depositing a 20 nm layer of gold by electron-beam evaporation and, finally, a lift-off by immersion in acetone. A computer-aided layout of a randomly arranged elongated nanoprism array that was used to create the resist mask and a schematic of the fabrication process flow are shown in Figure S2 and Figure S3, respectively, in Supporting Information Sections S2 and S3. More details are described in ref 39.

Characterization. *Linear Characterization.* Linear transmission spectra of the samples were measured using a collimated tungsten-halogen light source (experimental setup is shown in Figure S4 in the Supporting Information Section S4). The incident polarization was controlled using a broadband linear polarizing filter. The entire sample was illuminated, and the transmission from a single device was measured by first using a lens to image the sample plane into an intermediate image plane. The transmission from the correct device was then selected by a translating a variable aperture in this image plane, and by using a second lens to guide the transmitted light into the spectrometer.

Nonlinear Characterization. Signal beam from an optical parametric oscillator (Chameleon Compact) was used to illuminate the sample metasurfaces using a spectral SHG setup described in Supporting Information Section S5 (shown in Figure S5). The optical parametric oscillator was pumped using a Ti:sapphire laser (Chameleon Vision II) generating 200 fs long pulses with a repetition rate of 82 MHz. The average power of the signal beam was kept at 8 mW to avoid potential sample damage via accumulative heating. The SHG emission from the metasurfaces was detected as a function of the fundamental wavelength ranging between 1000 and 1300 nm using a power-calibrated photomultiplier tube (see Figure S5 in the Supporting Information Section S5). The input beam polarization was set to be linear and aligned with the long axes of the nanoprisms.

■ ASSOCIATED CONTENT

Supporting Information

The Supporting Information is available free of charge at https://pubs.acs.org/doi/10.1021/acs.nanolett.0c02991.

> Symmetric and nonsymmetric nanostructures' SHG response, computer-aided design of the layout of the randomly oriented elongated nanoprisms, plasmonic metasurface fabrication process, experimental setup for linear transmittance measurement, details of nonlinear experimental setup (PDF)

■ AUTHOR INFORMATION

Corresponding Author

Ksenia Dolgaleva – *School of Electrical Engineering and Computer Science, University of Ottawa, Ottawa, Ontairo K1N 6N5, Canada; Department of Physics, University of*

Ottawa, Ottawa, Ontario K1N 6N5, Canada;
Email: ksenia.dolgaleva@uottawa.ca

Authors

M. Saad Bin-Alam − *School of Electrical Engineering and Computer Science, University of Ottawa, Ottawa, Ontairo K1N 6N5, Canada;* orcid.org/0000-0002-0208-4004
Joshua Baxter − *Department of Physics, University of Ottawa, Ottawa, Ontario K1N 6N5, Canada;* orcid.org/0000-0002-1498-9361
Kashif M. Awan − *Stewart Blusson Quantum Matter Institute, University of British Columbia, Vancouver, British Columbia V6T 1Z4, Canada; School of Electrical Engineering and Computer Science, University of Ottawa, Ottawa, Ontairo K1N 6N5, Canada*
Antti Kiviniemi − *Laboratory of Photonics, Tampere University, FI-33014 Tampere, Finland*
Yaryna Mamchur − *National Technical University of Ukraine, "Igor Sikorsky Kyiv Polytechnic Institute", 03056 Kyiv, Ukraine; School of Electrical Engineering and Computer Science, University of Ottawa, Ottawa, Ontairo K1N 6N5, Canada*
Antonio Calà Lesina − *Hannover Centre for Optical Technologies, Cluster of Excellence PhoenixD (Photonics, Optics, and Engineering − Innovation Across Disciplines), and Fakultät für Maschinenbau (Institut für Transport- und Automatisierungstechnik), Leibniz Universität Hannover, 30167 Hannover, Germany;* orcid.org/0000-0002-9384-6245
Kosmas L. Tsakmakidis − *Section of Condensed Matter Physics, Department of Physics, National and Kapodistrian University of Athens, Panepistimioupolis, GR-157 84 Athens, Greece*
Mikko J. Huttunen − *Laboratory of Photonics, Tampere University, FI-33014 Tampere, Finland*
Lora Ramunno − *Department of Physics, University of Ottawa, Ottawa, Ontario K1N 6N5, Canada*

Complete contact information is available at:
https://pubs.acs.org/10.1021/acs.nanolett.0c02991

Author Contributions

K.D. conceived the basic idea for the whole work. K.L.T. conceived the idea of implementing the *RLC* model. M.S.B.-A. derived the analytical nonlinear *RLC* model. K.M.A. fabricated the metasurface substrate. M.J.H., M.S.B.-A., and A.K. carried out the measurements. J.B. performed the linear and nonlinear hydrodynamic-FDTD model simulations. J.B. and L.R. derived an expression for the nonlinear coefficient *a* using intuitive arguments. Y.M. made the illustration. K.D., L.R., M.J.H., K.L.T., and A.C.L. supervised the research and the development of the manuscript. M.S.B.A., J.B., and M.J.H. wrote the first draft of the manuscript. All coauthors subsequently took part in the revision process and approved the final copy of the manuscript.

Notes

The authors declare no competing financial interest.

■ ACKNOWLEDGMENTS

The authors thank Robert W. Boyd, Ekaterina Poutrina, John E. Sipe, and Gerd Leuchs for their valuable feedback and suggestions. The authors also thank Martti Kauranen for providing his lab at Tampere University in Finland to perform the experiment. K.D. and L.R. acknowledge support from the Canada Research Chairs (CRC) Program. K.D. acknowledges the financial support of the Natural Sciences and Engineering Research Council of Canada (NSERC) Discovery program. M.S.B.-A. acknowledges the support of the Ontario Graduate Scholarship (OGS), the University of Ottawa Excellence Scholarship, and the University of Ottawa International Experience Scholarship. J.B. acknowledges the financial support of NSERC Canada Graduate Scholarship-Master's (CGSM) Program and the University of Ottawa Excellence Scholarship, and the computational resources of Compute Canada. M.J.H. acknowledges the support of the Academy of Finland (Grant 308596) and the Flagship of Photonics Research and Innovation (PREIN) funded by the Academy of Finland (Grant 320165). K.L.T. acknowledges support from the General Secretariat for Research and Technology(GSRT) and the Hellenic Foundation for Research and Innovation (HFRI) under Grant 1819. A.C.L. acknowledges the Bundesministerium für Buldung und Furschung (German Federal Ministry of Education and Research) under the Tenure-Track Programme, and the Deutsche Forschungsgemeinschaft (DFG, German Research Foundation) under Germany's Excellence Strategy within the Cluster of Excellence PhoenixD (EXC 2122, Project ID 390833453).

■ REFERENCES

(1) Kildishev, A. V.; Boltasseva, A.; Shalaev, V. M. Planar photonics with metasurfaces. *Science* **2013**, *339*, 1232009.

(2) Yu, N.; Genevet, P.; Kats, M. A.; Aieta, F.; Tetienne, J.-P.; Capasso, F.; Gaburro, Z. Light propagation with phase discontinuities: generalized laws of reflection and refraction. *Science* **2011**, *334*, 333−337.

(3) Alù, A.; Silveirinha, M. G.; Salandrino, A.; Engheta, N. Epsilon-near-zero metamaterials and electromagnetic sources: Tailoring the radiation phase pattern. *Phys. Rev. B: Condens. Matter Mater. Phys.* **2007**, *75*, 155410.

(4) Zhang, S.; Park, Y.-S.; Li, J.; Lu, X.; Zhang, W.; Zhang, X. Negative index in chiral metamaterials. *Phys. Rev. Lett.* **2009**, *102*, 023901.

(5) Soukoulis, C. M.; Wegener, M. Past achievements and future challenges in the development of three-dimensional photonic metamaterials. *Nat. Photonics* **2011**, *5*, 523.

(6) Kauranen, M.; Zayats, A. V. Nonlinear plasmonics. *Nat. Photonics* **2012**, *6*, 737−748.

(7) Lapine, M.; Shadrivov, I. V.; Kivshar, Y. S. Colloquium: Nonlinear metamaterials. *Rev. Mod. Phys.* **2014**, *86*, 1093−1123.

(8) Minovich, A. E.; Miroshnichenko, A. E.; Bykov, A. Y.; Murzina, T. V.; Neshev, D. N.; Kivshar, Y. S. Functional and nonlinear optical metasurfaces. *Laser & Photonics Reviews* **2015**, *9*, 195−213.

(9) Butet, J.; Brevet, P. F.; Martin, O. J. Optical Second Harmonic Generation in Plasmonic Nanostructures: From Fundamental Principles to Advanced Applications. *ACS Nano* **2015**, *9*, 10545−10562.

(10) Li, G.; Zhang, S.; Zentgraf, T. Nonlinear photonic metasurfaces. *Nat. Rev. Mater.* **2017**, *2*, 1−14.

(11) Rahimi, E.; Gordon, R. Nonlinear Plasmonic Metasurfaces. *Adv. Opt. Mater.* **2018**, *6*, 1800274.

(12) Keren-Zur, S.; Michaeli, L.; Suchowski, H.; Ellenbogen, T. Shaping light with nonlinear metasurfaces. *Adv. Opt. Photonics* **2018**, *10*, 309−353.

(13) Pertsch, T.; Kivshar, Y. Nonlinear optics with resonant metasurfaces. *MRS Bull.* **2020**, *45*, 210−220.

(14) Lesina, A. C.; Berini, P.; Ramunno, L. Origin of third harmonic generation in plasmonic nanoantennas. Optical Materials Express. *Opt. Mater. Express* **2017**, *7*, 1575−1580.

(15) Kwiat, P. G.; Mattle, K.; Weinfurter, H.; Zeilinger, A.; Sergienko, A. V.; Shih, Y. New high-intensity source of polarization-entangled photon pairs. *Phys. Rev. Lett.* **1995**, *75*, 4337.

(16) Rasekh, P.; Saliminabi, M.; Yildirim, M.; Boyd, R. W.; Ménard, J.-M.; Dolgaleva, K. Propagation of broadband THz pulses: effects of dispersion, diffraction and time-varying nonlinear refraction. *Opt. Express* **2020**, *28*, 3237−3248.

(17) Brabec, T.; Krausz, F. Intense few-cycle laser fields: Frontiers of nonlinear optics. *Rev. Mod. Phys.* **2000**, *72*, 545.

(18) Kippenberg, T. J.; Holzwarth, R.; Diddams, S. A. Micro-resonator-Based Optical Frequency Combs. *Science* **2011**, *332*, 555−560.

(19) Shcherbakov, M. R.; Vabishchevich, P. P.; Shorokhov, A. S.; Chong, K. E.; Choi, D. Y.; Staude, I.; Miroshnichenko, A. E.; Neshev, D. N.; Fedyanin, A. A.; Kivshar, Y. S. Ultrafast All-Optical Switching with Magnetic Resonances in Nonlinear Dielectric Nanostructures. *Nano Lett.* **2015**, *15*, 6985−6990.

(20) Minerbi, E.; Keren-Zur, S.; Ellenbogen, T. Nonlinear metasurface fresnel zone plates for terahertz generation and manipulation. *Nano Lett.* **2019**, *19*, 6072−6077.

(21) Lin, Z.; Huang, L.; Xu, Z. T.; Li, X.; Zentgraf, T.; Wang, Y. Four-Wave Mixing Holographic Multiplexing Based on Nonlinear Metasurfaces. *Adv. Opt. Mater.* **2019**, *7*, 1900782.

(22) Sipe, J. E.; So, V. C. Y.; Fukui, M.; Stegeman, G. I. Analysis of second-harmonic generation at metal surface. *Phys. Rev. B: Condens. Matter Mater. Phys.* **1980**, *21*, 4389.

(23) Scalora, M.; Vincenti, M. A.; De Ceglia, D.; Roppo, V.; Centini, M.; Akozbek, N.; Bloemer, M. J. Second- and third-harmonic generation in metal-based structures. *Phys. Rev. A: At., Mol., Opt. Phys.* **2010**, *82*, 1−14.

(24) Ciracì, C.; Poutrina, E.; Scalora, M.; Smith, D. R. Second-harmonic generation in metallic nanoparticles: Clarification of the role of the surface. *Phys. Rev. B: Condens. Matter Mater. Phys.* **2012**, *86*, 1−10.

(25) Ginzburg, P.; Krasavin, A. V.; Wurtz, G. A.; Zayats, A. V. Nonperturbative hydrodynamic model for multiple harmonics generation in metallic nanostructures. *ACS Photonics* **2015**, *2*, 8−13.

(26) O'Brien, K.; Suchowski, H.; Rho, J.; Salandrino, A.; Kante, B.; Yin, X.; Zhang, X. Predicting nonlinear properties of metamaterials from the linear response. *Nat. Mater.* **2015**, *14*, 379−383.

(27) Engheta, N.; Salandrino, A.; Alu, A. Circuit Elements at Optical Frequencies: Nanoinductors, Nanocapacitors, and Nanoresistors. *Phys. Rev. Lett.* **2005**, *95*, 095504.

(28) Huang, C.-p.; Yin, X.-g.; Huang, H.; Zhu, Y.-y. Study of plasmon resonance in a gold nanorod with an LC circuit model. *Opt. Express* **2009**, *17*, 6407.

(29) Zhou, J.; Koschny, T.; Kafesaki, M.; Economou, E. N.; Pendry, J. B.; Soukoulis, C. M. Saturation of the Magnetic Response of Split-Ring Resonators at Optical Frequencies. *Phys. Rev. Lett.* **2005**, *95*, 223902.

(30) Tretyakov, S. On geometrical scaling of split-ring and double-bar resonators at optical frequencies. *Metamaterials* **2007**, *1*, 40−43.

(31) Staffaroni, M.; Conway, J.; Vedantam, S.; Tang, J.; Yablonovitch, E. Circuit analysis in metal-optics. *Photonics Nanostructures - Fundam. Appl.* **2012**, *10*, 166−176.

(32) Poutrina, E.; Huang, D.; Smith, D. R. Analysis of nonlinear electromagnetic metamaterials. *New J. Phys.* **2010**, *12*, 093010.

(33) Lippitz, M.; Van Dijk, M. A.; Orrit, M. Third-harmonic generation from single gold nanoparticles. *Nano Lett.* **2005**, *5*, 799−802.

(34) Boyd, R. W. *Nonlinear optics*, 4th ed.; Academic Press: San Diego, 2020.

(35) Butet, J.; Duboisset, J.; Bachelier, G.; Russier-Antoine, I.; Benichou, E.; Jonin, C.; Brevet, P. F. Optical second harmonic generation of single metallic nanoparticles embedded in a homogeneous medium. *Nano Lett.* **2010**, *10*, 1717−1721.

(36) Czaplicki, R.; Kiviniemi, A.; Huttunen, M. J.; Zang, X.; Stolt, T.; Vartiainen, I.; Butet, J.; Kuittinen, M.; Martin, O. J. F.; Kauranen, M. Less is more − enhancement of second-harmonic generation from metasurfaces by reduced nanoparticle density. *Nano Lett.* **2018**, *18*, 7709−7714.

(37) Klein, M. W.; Enkrich, C.; Wegener, M.; Linden, S. Second-harmonic generation from magnetic metamaterials. *Science* **2006**, *313*, 502−504.

(38) Huttunen, M. J.; Rasekh, P.; Boyd, R. W.; Dolgaleva, K. Using surface lattice resonances to engineer nonlinear optical processes in metal nanoparticle arrays. *Phys. Rev. A: At., Mol., Opt. Phys.* **2018**, *97*, 053817.

(39) Awan, K. *Fabrication of III-V Integrated Photonic Devices*. Ph.D. Thesis, Université d'Ottawa/University of Ottawa, Ottawa, 2018.

(40) Auguié, B.; Barnes, W. L. Collective resonances in gold nanoparticle arrays. *Phys. Rev. Lett.* **2008**, *101*, 143902.

(41) Meinzer, N.; Barnes, W. L.; Hooper, I. R. Plasmonic meta-atoms and metasurfaces. *Nat. Photonics* **2014**, *8*, 889−898.

(42) Kataja, M.; Hakala, T. K.; Julku, A.; Huttunen, M. J.; van Dijken, S.; Törmä, P. Surface lattice resonances and magneto-optical response in magnetic nanoparticle arrays. *Nat. Commun.* **2015**, *6*, 7072.

(43) Huttunen, M. J.; Dolgaleva, K.; Törmä, P.; Boyd, R. W. Ultra-strong polarization dependence of surface lattice resonances with out-of-plane plasmon oscillations. *Opt. Express* **2016**, *24*, 28279.

(44) Kravets, V. G.; Kabashin, A. V.; Barnes, W. L.; Grigorenko, A. N. Plasmonic Surface Lattice Resonances: A Review of Properties and Applications. *Chem. Rev.* **2018**, *118*, 5912−5951.

(45) Reshef, O.; Saad-Bin-Alam, M.; Huttunen, G.; Carlow, M.; Sullivan, B. T.; Ménard, J.-M.; Dolgaleva, K.; Boyd, R. W. Multiresonant High-Q Plasmonic Metasurfaces. *Nano Lett.* **2019**, *19*, 6429−6434.

(46) Bin-Alam, M. S.; Reshef, O.; Mamchur, Y.; Alam, M. Z.; Carlow, G.; Upham, J.; Sullivan, B. T.; Ménard, J.-M.; Huttunen, M. J.; Boyd, R. W.; Dolgaleva, K. Ultra-high-Q resonances in plasmonic metasurfaces. *arXiv* 2020, https://arxiv.org/abs/2004.05202v2 (accessed July 10, 2020).

(47) Shi, L.; Hakala, T. K.; Rekola, H. T.; Martikainen, J.-P.; Moerland, R. J.; Torma, P. Spatial Coherence Properties of Organic Molecules Coupled to Plasmonic Surface Lattice Resonances in the Weak and Strong Coupling Regimes. *Phys. Rev. Lett.* **2014**, *112*, 153002.

(48) Bautista, G.; Huttunen, M. J.; Mäkitalo, J.; Kontio, J. M.; Simonen, J.; Kauranen, M. Second-harmonic generation imaging of metal nano-objects with cylindrical vector beams. *Nano Lett.* **2012**, *12*, 3207−3212.

(49) Herman, W. N.; Hayden, L. M. Maker fringes revisited: second-harmonic generation from birefringent or absorbing materials. *J. Opt. Soc. Am. B* **1995**, *12*, 416.

(50) Prokopidis, K. P.; Zografopoulos, D. C. A Unified FDTD/PML Scheme Based on Critical Points for Accurate Studies of Plasmonic Structures. *J. Lightwave Technol.* **2013**, *31*, 2467−2476.

(51) Lesina, A. C.; Vaccari, A.; Berini, P.; Ramunno, L. On the convergence and accuracy of the FDTD method for nanoplasmonics. *Opt. Express* **2015**, *23*, 10481−10497.

(52) Jackson, J. D. *Classical electrodynamics*, 3rd ed.; John Wiley: New York, 1999.

(53) de Beer, A. G. F.; Roke, S.; Dadap, J. I. Theory of optical second-harmonic and sum-frequency scattering from arbitrarily shaped particles. *J. Opt. Soc. Am. B* **2011**, *28*, 1374−1384.

(54) Mäkitalo, J.; Suuriniemi, S.; Kauranen, M. Boundary element method for surface nonlinear optics of nanoparticles: erratum. *Opt. Express* **2013**, *21*, 10205.

(55) Roke, S.; Bonn, M.; Petukhov, A. V. Nonlinear optical scattering: The concept of effective susceptibility. *Phys. Rev. B: Condens. Matter Mater. Phys.* **2004**, *70*, 1−10.

(56) Wang, F. X.; Rodríguez, F. J.; Albers, W. M.; Ahorinta, R.; Sipe, J. E.; Kauranen, M. Surface and bulk contributions to the second-order nonlinear optical response of a gold film. *Phys. Rev. B: Condens. Matter Mater. Phys.* **2009**, *80*, 4−7.

(57) De Beer, A. G.; Roke, S. Nonlinear Mie theory for second-harmonic and sum-frequency scattering. *Phys. Rev. B: Condens. Matter Mater. Phys.* **2009**, *79*, 1−9.

(58) Vance, F. W.; Lemon, B. I.; Hupp, J. T. Enormous Hyper-Rayleigh Scattering from Nanocrystalline Gold Particle Suspensions. *J. Phys. Chem. B* **1998**, *102*, 10091−10093.

(59) Russier-antoine, I.; Jonin, C.; Nappa, J.; Benichou, E.; Brevet, P. F. Wavelength dependence of the hyper Rayleigh scattering response from gold nanoparticles. *J. Chem. Phys.* **2004**, *120*, 10748.

(60) Nappa, J.; Revillod, G.; Russier-Antoine, I.; Benichou, E.; Jonin, C.; Brevet, P. F. Electric dipole origin of the second harmonic generation of small metallic particles. *Phys. Rev. B: Condens. Matter Mater. Phys.* **2005**, *71*, 165407.

(61) Duboisset, J.; Russier-Antoine, I.; Benichou, E.; Bachelier, G.; Jonin, C.; Brevet, P. F. Single Metallic Nanoparticle Sensitivity with Hyper Rayleigh Scattering. *J. Phys. Chem. C* **2009**, *113*, 13477−13481.

(62) Novotny, L.; Hecht, B. *Principles of nano-optics*, 1st ed.; Cambridge University Press: New York, 2006.

(63) Michaeli, L.; Keren-Zur, S.; Avayu, O.; Suchowski, H.; Ellenbogen, T. Nonlinear Surface Lattice Resonance in Plasmonic Nanoparticle Arrays. *Phys. Rev. Lett.* **2017**, *118*, 970.

(64) Huttunen, M. J.; Reshef, O.; Stolt, T.; Dolgaleva, K.; Boyd, R. W.; Kauranen, M. Efficient nonlinear metasurfaces by using multiresonant high-Q plasmonic arrays. *Journal of the Optical Society of America B* **2019**, *36*, 118.

(65) Chen, S.; Reineke, B.; Li, G.; Zentgraf, T.; Zhang, S. Strong nonlinear optical activity induced by lattice surface modes on plasmonic metasurface. *Nano Lett.* **2019**, *19*, 6278−6283.

(66) Hooper, D. C.; Kuppe, C.; Wang, D.; Wang, W.; Guan, J.; Odom, T. W.; Valev, V. K. Second harmonic spectroscopy of surface lattice resonances. *Nano Lett.* **2019**, *19*, 165−172.

(67) Johnson, P. B.; Christy, R. W. Optical Constants of the Noble Metals. *Phys. Rev. B - Condens. Matter Mater. Phys.* **1972**, *6*, 4370.

(68) Graham - CC Doc. https://docs.computecanada.ca/wiki/Graham (accessed Sept. 4, 2019).

Supporting Information

Hyperpolarizability of plasmonic meta-atoms in metasurfaces

M. Saad Bin-Alam,[†] Joshua Baxter,[‡] Kashif M. Awan,[¶,†] Antti Kiviniemi,[§]
Yaryna Mamchur,[‖,†] Antonio Calà Lesina,[⊥] Kosmas L. Tsakmakidis,[#]
Mikko J. Huttunen,[§] Lora Ramunno,[‡] and Ksenia Dolgaleva[*,†,‡]

†*School of Electrical Engineering and Computer Science, University of Ottawa, Ottawa, ON, K1N 6N5, Canada*

‡*Department of Physics, University of Ottawa, Ottawa, ON, K1N 6N5, Canada*

¶*Stewart Blusson Quantum Matter Institute, University of British Columbia, Vancouver, BC, V6T 1Z4, Canada*

§*Laboratory of Photonics, Tampere University, FI-33014 Tampere, Finland*

‖*National Technical University of Ukraine, "Igor Sikorsky Kyiv Polytechnic Institute," Kyiv, Ukraine*

⊥*Hannover Centre for Optical Technologies, Cluster of Excellence PhoenixD (Photonics, Optics, and Engineering – Innovation Across Disciplines), and Fakultät für Maschinenbau (Institut für Transport- und Automatisierungstechnik), Leibniz Universität Hannover, 30167, Hannover, Germany*

#*Section of Condensed Matter Physics, Department of Physics, National and Kapodistrian University of Athens, Panepistimioupolis, GR-157 84 Athens, Greece*

E-mail: ksenia.dolgaleva@uottawa.ca

In Sec. S1, Fig. 1 shows a comparison between the symmetric and non-symmetric nanostructures' SHG response. In Sec. S2, Fig. 2 shows a computer-aided design of the layout of the randomly oriented elongated nanoprisms prior to the electron-beam lithography process of the plasmonic metasurfaces. In Sec. S3, Fig. 3 shows a schematic of the fabrication process of the plasmonic metasurfaces. In Sec. S4, Fig. 4 shows the experimental setup (a short description is also provided) we used to measure the linear transmittance of the fabricated metasurfaces. In Sec. S5, we elaborately describe the details of the experimental setup (shown in Fig. 5) used in SHG power measurement.

S1: Symmetric vs. non-symmetric nanostructures, the lattice arrangement, geometric vs. surface contributions on Second-Harmonic Generation (SHG)

Symmetric vs. non-Symmetric nanostructures, and the lattice arrangement:

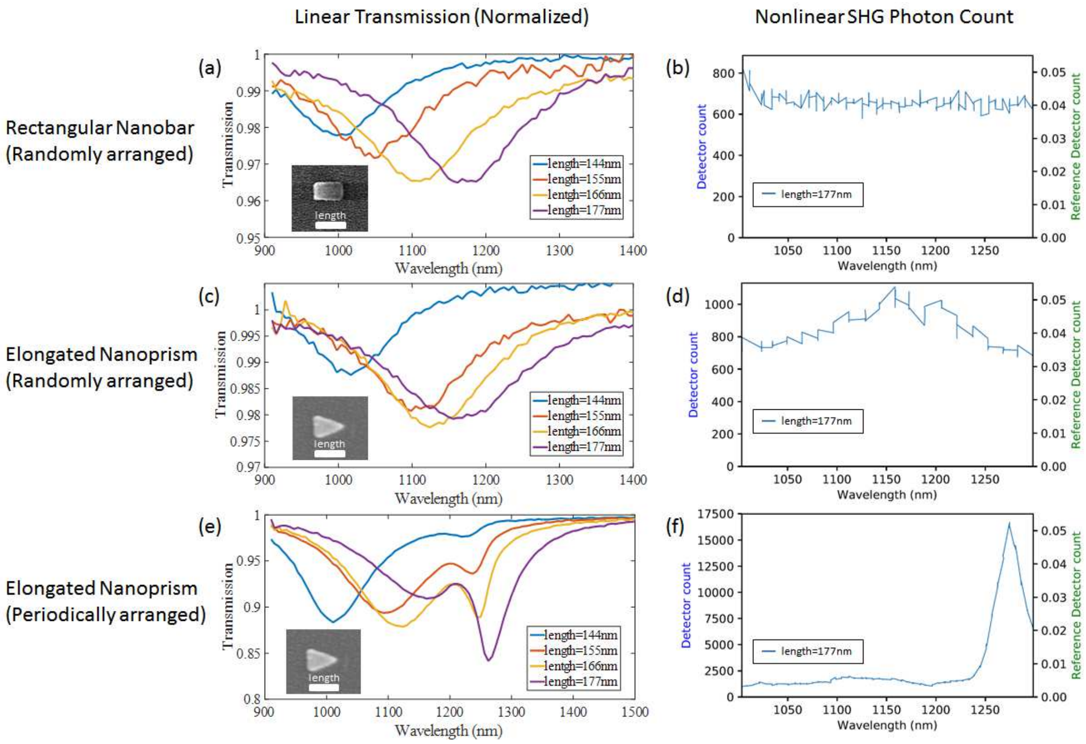

Fig. 1 — Symmetric (randomly positioned) vs. non-Symmetric (periodically positioned) meta-atoms. Linear transmission (a, c, e) and SHG photon-count (b, d, f) as a function of incident wavelength for (a-b) rectangular nanobars arranged randomly, (c-d) elongated nanoprisms arranged randomly, and (e-f) elongated nanoprisms arranged periodically in the metasurface arrays. For randomly positioned rectangular nanobars, there is no SHG peak enhancement (b) at the LSPRs identified in (a) even though they were after pumped by 40 mW input laser power. For randomly positioned elongated nanoprisms, there is a clear SHG peak enhancement in (d) at the LSPRs evedent in (c) even with much lower input laser power within 5 to 8 mW. This comparison between (b) and (d) clearly depicts that, under electric-dipole approximation, SHG signals generated from the geometrically symmetric nanostructures is weaker than its geometrically non-symmetric counterparts. A large SHG peak enhancement occurs in the array of periodic elongated nanoprisms (f) due to the narrow plasmonic surface lattice resonances at longer wavelengths than the LSPRs, as evident in (e).

S2: Computer-aided design (CAD) layout of the array of the randomly arranged elongated nanoprisms

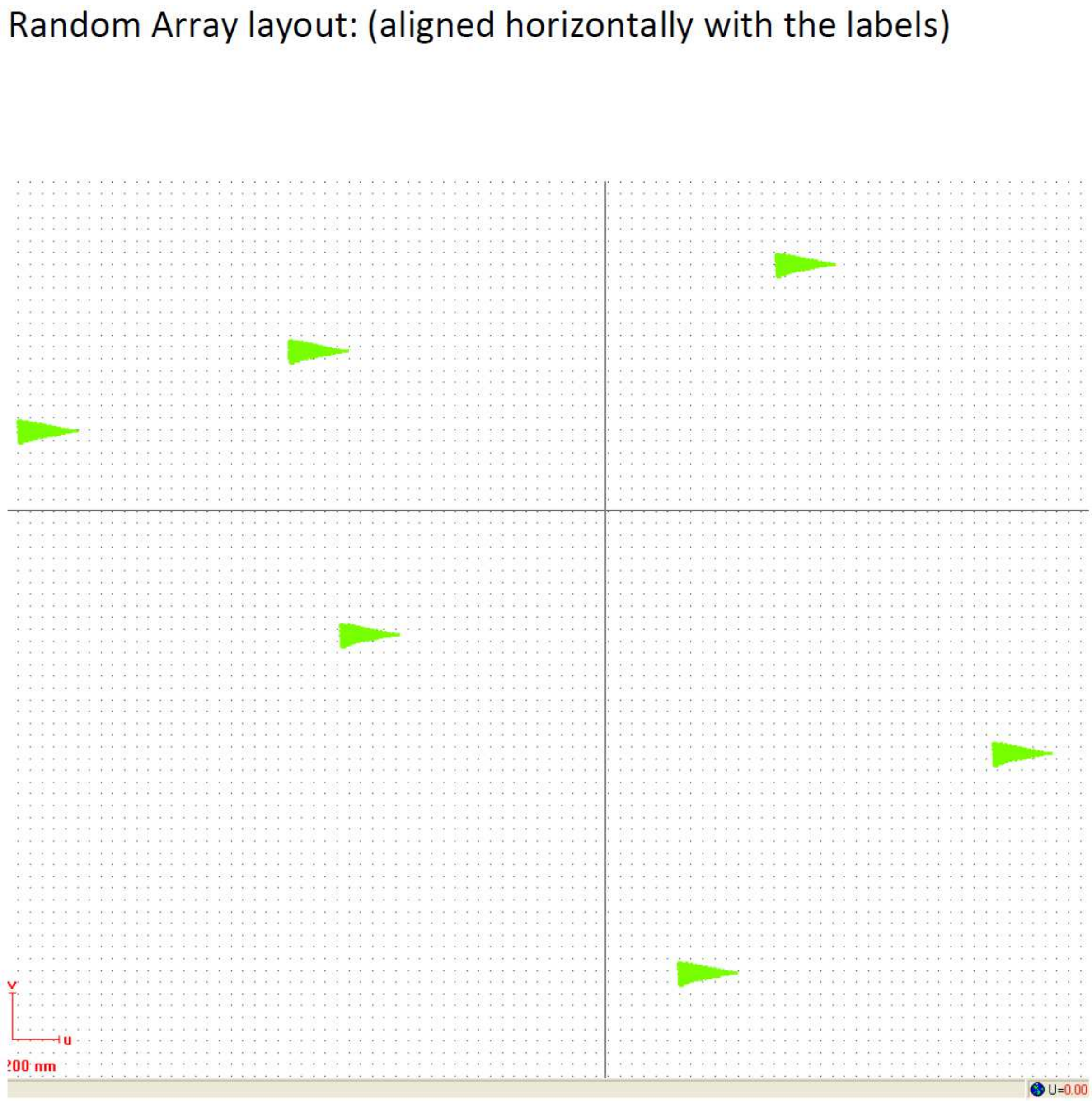

Random Array layout: (aligned horizontally with the labels)

Fig. 2 — Computer-Aided Design (CAD) Image. Close-up of a computer-aided layout of a randomly arranged elongated nanoprism array that is used to create the resist mask in the Electron-beam lithography.

S3: Plasmonic metasurface fabrication process

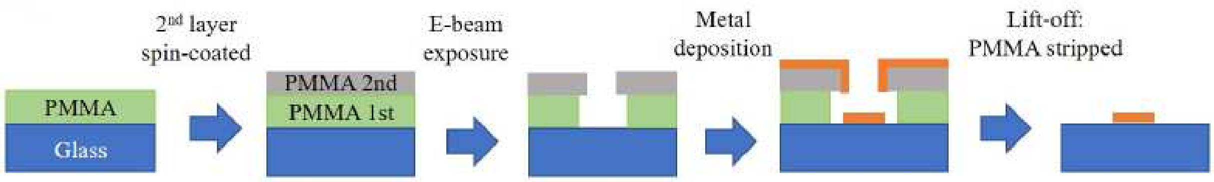

Fig. 3 — Fabrication Process. Schematic of the fabrication process flow.

S4: Experimental setup for linear transmittance measurement

Fig. 4(a) shows the schematic of the linear transmittance measurement setup. A broadband source is collimated and is polarized using a broadband linear polarizing filter. A first iris is optionally placed to help align the sample in the center of the beam. The beam is then passed through the sample. The surface of the device is imaged using a lens, and a pinhole is placed in the image plane to select the desired array. The transmitted light is collected in a large core multimode fiber and is analyzed using an optical spectrum analyzer. Fig. 4(b-c) shows the SEM images of a Rectangular nanobar and an elongated nanoprism. Fig. 4(d-e) shows the corresponding transmission spectra of varying lengths (average lengths for both shapes: $l = 145$, 156, 167 and 178 nm)

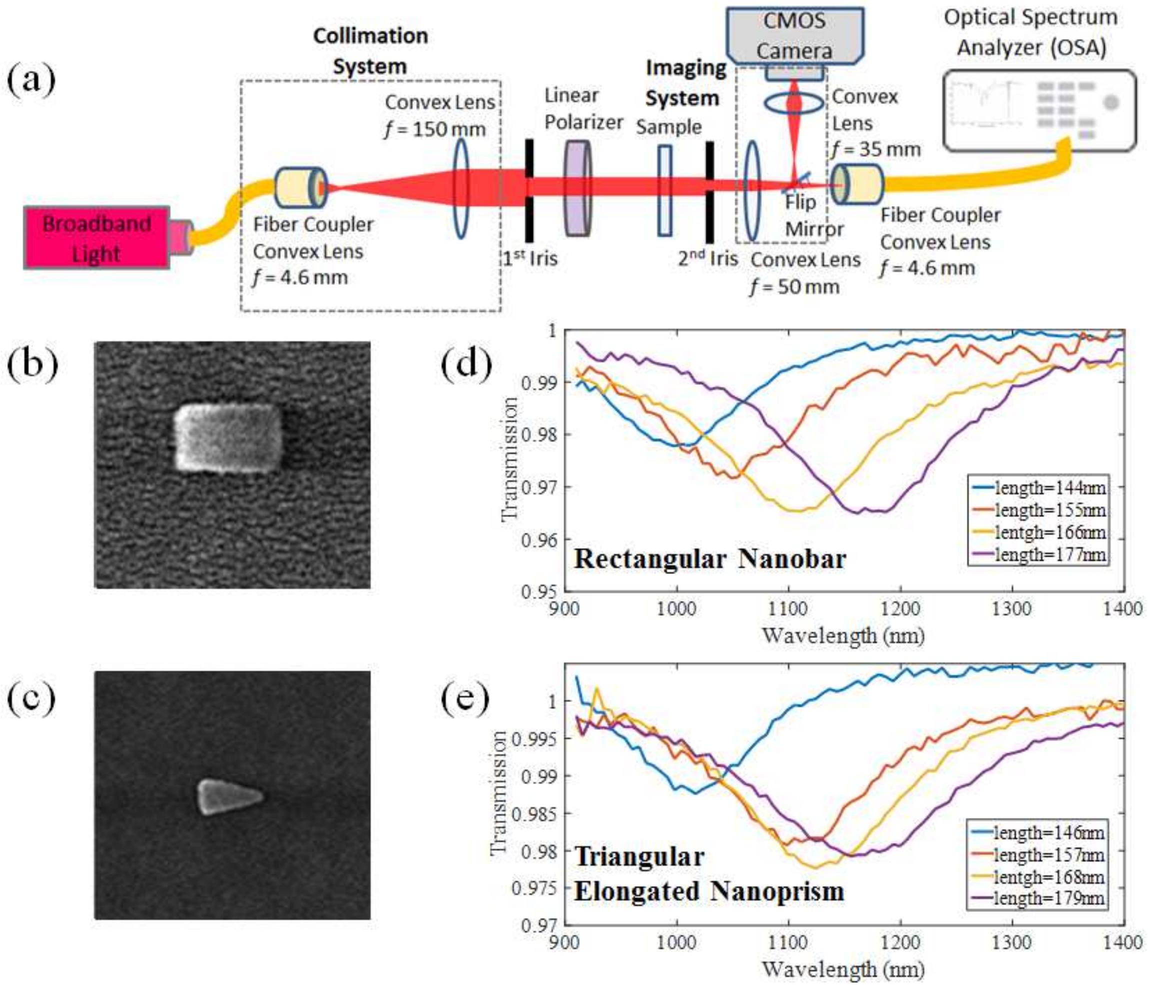

Fig. 4 — Linear Setup and Measurement. (a) Experimental setup for the linear transmission measurement. (b-c) SEM images of a Rectangular nanobar and an elongated nanoprism. (d-e) corresponding transmission spectra of varying lengths (average lengths for both shapes: l = 145, 156, 167 and 178 nm).

S5: Details of nonlinear experimental setup

A schematic of the SHG experimental setup is illustrated in Fig. 2. A motorized achromatic half-wave plate (HWP) and a polarizer were used to control the level of power P_ω from the OPO. Before entering the polarization-control part of the setup, the fundamental beam was cleaned and expanded with a set of lenses and an aperture (diameter D = 25 μm). To weakly focus the beam on the sample arrays, an achromatic lens with the focal length of

150 mm was used, ensuring a relatively small beam waist diameter of the excitation beam (around 100 μm) while the plane-wave approximation could still be used. To control the input polarization, we used a high-quality polarizer and an achromatic HWP, whereas to select the polarization of the emitted SHG light, we used a film polarizer after the sample. Then, to pass (block) the fundamental beam, we used a 900 nm long-pass (700 nm short-pass) filter. To efficiently collect the generated SH signal, a lens with the focal length of 16 mm was used after the sample. After being reflected by a dichroic mirror and passing through another short-pass filter (900 nm), the SHG signal was focused on the active area of a photomultiplier tube (PMT) module with another achromatic lens of 150 mm focal length. For sample alignment, the light transmitted through the dichroic mirror was used to image the sample plane with a CMOS camera and a camera lens (MVL50M23). The PMT has been calibrated using a sensitive power meter, and the result is that 1 count/s corresponds to 5.2 aW.

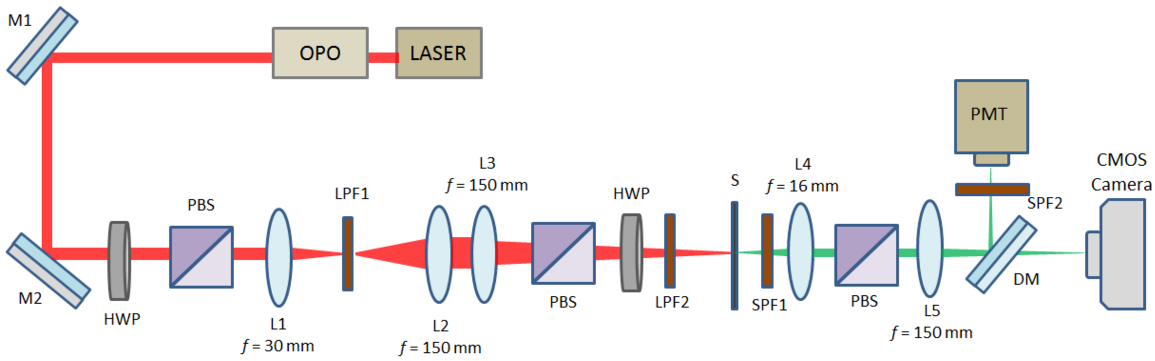

Fig. 5 — Nonlinear SHG Experimental Setup. Schematic representation of the experimental setup for measuring SHG. M – mirrors, HWP – motorized half-wave plates, P – polarizers, S - sample, L – lenses (L1 has f = 30 mm, L2 has f = 150 mm, L3 has f=150 mm, L4 has f=16 mm, L5 has f=150 mm, L1, L2, L3, and L5 – achromats). LPF — long-pass filter at 900 nm, SPF1 — short-pass filter at 700 nm, A – film polarizer (analyzer), DM – dichroic mirror, SPF2 – short-pass filter at 900 nm, PMT – photomultiplier tube (PicoQuant PMA-C 192-M).

Chapter 3

Plasmonic Metasurface with Ultra-High-Q Resonances

3.1 Summary

This chapter presents the first-time experimental observation of an ultra-high-Q surface lattice resonances in a metasurface platform enabled by periodically arranged plasmonic nanostructures made of gold. Integrating such metasurfaces with any electro-optical or semiconductor flat optical thin films would lay down the base of dynamic or active modulation of free-space light for beam steering, sensing, photodetection, and imaging. Nevertheless, the intrinsic losses in the plasmonic metals have so far been thought of as the primary barrier to the practical efficient realization of the pronounced potential applications. Notwithstanding, a careful design of plasmonic metasurfaces, for example, the wise selection of the incident light polarization alongside the individual plasmonic nanoparticles' shape, size, and lattice periodicity, can excite nonlocalized diffraction-order modes in the plane of the metasurface, which may exhibit very high-Q resonances. Despite the theoretical prediction, experimental manifestation of such high-Q resonant modes, also called plasmonic surface lattice resonances (SLRs), has not been previously observed due to the limitation existing in the sample fabrication and characterization processes. In the project presented in this chapter, by overcoming these limitations, we observed ultra-high-Q SLRs and their polarization dependence.

3.2 Contributions

The results provided in this chapter have been published in *Nature Communications* [72]. I was the only graduate student involved in this project. I primarily accomplished three tasks: 1. The design of the plasmonic metasurface with an SLR feature at the desired wavelength using Lumerical FDTD software, 2. Building a linear transmission measurement setup in the lab, and 3. Figuring out the limitations in the design and characterization techniques which obstructed the observation of ultra-high-Q SLRs in other groups' experiments. My findings ultimately led me to overcome the challenges in my design and experimental characterization processes.

Notwithstanding, throughout the duration of this project, I required help from my colleagues. Together with Dr. Orad Reshef and Dr. Mikko J. Huttunen from the University of Ottawa and Tampere University, I conceived the basic idea for this work. I obtained the training from Dr. Orad Reshef who helped me to perform FDTD simulations. Together with Dr. Mikko J. Huttunen and Dr. Orad Reshef, I performed the lattice-sum calculation. Dr. Orad Reshef and Dr. Graham Carlow fabricated the device. Dr. Zahirul Alam and Dr. Mikko J. Huttunen trained me in designing and building the experimental setup. Ms. Yaryna Mamchur, a former undergraduate Mitax Globalink intern student from Ukraine, assisted me in performing the measurements at the final stage of the experimental characterization. I analyzed the experimental results by comparing them with the simulated data, which helped me to understand how to improve the devices to obtain the desired results. Last but not least, Dr. Jeremy Upham, Dr. Brian T. Sullivan, Prof. Jean-Michel Ménard, Dr. Mikko J. Huttunen, Prof. Robert W. Boyd, and Prof. Ksenia Dolgaleva supervised the whole research project and the development of the manuscript. I wrote the first draft of the manuscript, which was checked and corrected by Dr. Orad Reshef. All co-authors subsequently took part in the revision process and approved the final copy of the manuscript.

3.3 Article

The published article follows verbatim.

nature COMMUNICATIONS

ARTICLE

https://doi.org/10.1038/s41467-021-21196-2 OPEN

Ultra-high-Q resonances in plasmonic metasurfaces

M. Saad Bin-Alam[1,7], Orad Reshef [2,7]✉, Yaryna Mamchur[1,3], M. Zahirul Alam [2], Graham Carlow[4], Jeremy Upham[2], Brian T. Sullivan[4], Jean-Michel Ménard [2], Mikko J. Huttunen[5], Robert W. Boyd[1,2,6] & Ksenia Dolgaleva[1,2]

Plasmonic nanostructures hold promise for the realization of ultra-thin sub-wavelength devices, reducing power operating thresholds and enabling nonlinear optical functionality in metasurfaces. However, this promise is substantially undercut by absorption introduced by resistive losses, causing the metasurface community to turn away from plasmonics in favour of alternative material platforms (e.g., dielectrics) that provide weaker field enhancement, but more tolerable losses. Here, we report a plasmonic metasurface with a quality-factor (Q-factor) of 2340 in the telecommunication C band by exploiting surface lattice resonances (SLRs), exceeding the record by an order of magnitude. Additionally, we show that SLRs retain many of the same benefits as localized plasmonic resonances, such as field enhancement and strong confinement of light along the metal surface. Our results demonstrate that SLRs provide an exciting and unexplored method to tailor incident light fields, and could pave the way to flexible wavelength-scale devices for any optical resonating application.

---

[1] School of Electrical Engineering and Computer Science, University of Ottawa, Ottawa, ON, Canada. [2] Department of Physics, University of Ottawa, Ottawa, ON, Canada. [3] National Technical University of Ukraine “Igor Sikorsky Kyiv Polytechnic Institute”, Kyiv, Ukraine. [4] Iridian Spectral Technologies Inc., Ottawa, ON, Canada. [5] Photonics Laboratory, Physics Unit, Tampere University, Tampere, Finland. [6] Institute of Optics and Department of Physics and Astronomy, University of Rochester, Rochester, NY, USA. [7] These authors contributed equally: M. Saad Bin-Alam, Orad Reshef. ✉email: orad@reshef.ca

Metallic nanostructures are essential to many applications in photonics, including biosensing[1], spectroscopy[2,3], nanolasing[4], all-optical switching[5], nonlinear optical processes[6], and metasurface technologies[7–9]. These plasmonic elements form flexible components with geometry-dependent responses and have many desirable properties, such as the possibility to confine light to sub-wavelength scales and large local-field enhancements[9,10]. Metals also possess intrinsic nonlinear optical constants that are many orders of magnitude larger than dielectric materials[11].

When structured at the sub-wavelength scale[8,9,12], individual nanostructures exhibit localized surface plasmon resonances (LSPRs), where electromagnetic fields couple to the free-electron plasma of a conductor at a metal–dielectric interface[6,10]. Depending on its shape, an individual nanoparticle may be polarized by an incident light beam, acting as a lossy dipole antenna[13] and trapping light for a short period of time. In contrast to other photonic resonant devices such as whispering gallery mode resonators, microring resonators, or photonic crystals[14–16], resonating dipoles in a metasurface can easily be accessed by a beam propagating in free space and require only a sub-wavelength propagation region for operation. Therefore, a plasmonic metasurface resonator enables a series of specialized optical responses, including phase-matching-free nonlinear optical effects[6,17], strongly localized field enhancements[9], multi-mode operation[18], and a spatially localized optical response[7]. Such a metasurface with a large quality factor (Q-factor) could be used as a cavity for applications that need increased light–matter interactions, small mode volumes, large field enhancements, and large optical nonlinearities, such as an ultra-flat nano-laser with a large transverse mode size[4,19] or frequency conversion applications (e.g., nonlinear harmonic generation[20] or THz-wave generation[21]). One frequently cited limitation of LSPR-based metasurfaces are their low Q-factors (e.g., $Q < 10$) due to the intrinsic Ohmic losses present in metals at optical frequencies[10,22–24]. As the Q-factor is related to the light–matter interaction time as well as to enhancements to the electric field, it is typically desirable to maximize this quantity[14]. Low Q-factors therefore make many potential applications of plasmonics-based metasurface devices impractical, and new methods for obtaining large Q-factor resonances in a metasurface have long been sought after.

The optical response of coupled plasmonic nanoresonators has been a topic of intense study[25]. Notably, plasmonic metasurfaces of large periodically arranged nanostructures support collective resonances called surface lattice resonances (SLRs)[26–32]. Here the individual responses from the surface plasmons of many individual nanostructures form a collective response that couples to in-plane diffraction orders of the periodic array[26,30]. As a consequence, a relatively high-Q resonance can emerge at an optical wavelength $\lambda_{\mathrm{SLR}} \approx nP$, close to the product of the refractive index of the background medium n and the lattice period P[26,32]. Recent theoretical studies of this platform have predicted Q-factors on the order of 10^3 by properly engineering the dimensions of the individual nanostructures and the period of the lattice[31–33], hinting at the possibility of combining the aforementioned benefits of metals with long interaction times provided by high Q-factors. However, to date, the highest experimentally observed Q-factor in an SLR-based metasurface is 430[34]. The disparity between theory and experiment has been attributed to a variety of reasons, including poor spatial coherence of light beams[28,35], small array sizes[30,31,36], fabrication imperfections[30,31], and the addition of an adhesion layer[37].

Inspired by this discrepancy, here we perform a detailed investigation to determine the dominant factors that most drastically affect the observed Q of an SLR-based metasurface: the nanostructure geometry, the array size, and the spatial coherence of the probing light source. Using the results of this study, we demonstrate a plasmonic metasurface capable of supporting ultra-high-Q SLRs.

Results

The metasurface in consideration consists of a rectangular array of rectangular gold nanostructures embedded in a homogeneous silica glass ($n \sim 1.45$) environment (Fig. 1a). The lattice constant $P_y = 1060$ nm was selected to place the SLR wavelength in the telecommunication window; $P_x = 500$ nm was reduced from a square lattice, increasing the nanoparticle density and consequently increasing the extinction ratio of the resonance. The overcladding is carefully matched to the substrate material to ensure a symmetric cladding index, as it has been shown that the Q of an SLR may be affected by the homogeneity of the environment[26,38,39]. As shown by the numerical predictions in Fig. 1b, for an x-polarized beam, this metasurface is expected to support an LSPR at $\lambda_{\mathrm{LSPR}} = 830$ nm and an SLR of the first type around $\lambda_{\mathrm{SLR}} = 1550$ nm (See Supplementary Sec. S2: SLR type). The SLR linewidth is substantially narrower than that of the LSPR, corresponding to a much higher Q-factor. Incidentally, the inset field profiles in Fig. 1b also reveal that the SLR provides a more significant field enhancement, with $|E_{\max}(\lambda_{\mathrm{SLR}})| \sim 3|E_{\max}(\lambda_{\mathrm{LSPR}})|$. Figure 1c shows an image of the fabricated device with dimensions matching those of the simulations. The measured transmission spectra are presented in Fig. 1d, closely matching the predicted spectrum. Notably, the full width at half-maximum of the linewidth is only $\Delta\lambda = 0.66$ nm, corresponding to a Q-factor of $Q = 2340$. This value exceeds the record for plasmonic metasurfaces by an order of magnitude[34,37,40] and is among the highest reported in a metasurface. It is roughly within a factor of two of semi-analytic calculations performed using the lattice sum approach (LSA), where $Q \sim 5000$ (see “Methods” for details). In order to observe this value for the Q-factor, both the metasurface and the measurement apparatus needed to be arranged with a few considerations in mind, which we describe in greater detail below.

The role of nanoparticle polarizability. First, the individual structures need to be engineered to exhibit the appropriate response at λ_{SLR}. The optical response of a nanostructure can be approximated using the polarizability of a Lorentzian dipole,

$$\alpha(\omega) = \frac{A_0}{\omega - \omega_0 + i\gamma}, \tag{1}$$

where A_0 is the oscillator strength, $\omega_0 = 2\pi c/\lambda_{\mathrm{LSPR}}$ corresponds to the nanoparticle resonance frequency, and γ is the damping term. These quantities all depend on the particle geometry[12] (here the length L_y and width L_x of a rectangular bar). The contribution of the particle lattice to the polarizability can be introduced using the LSA[39,41]:

$$\alpha^*(\omega) = \frac{\alpha(\omega)}{1 - \epsilon_0 \alpha(\omega) S(\omega)}, \tag{2}$$

where $\alpha^*(\omega)$ is known as the effective polarizability of the entire metasurface and $S(\omega)$ corresponds to the lattice sum. This latter term depends only on the arrangement of the lattice. An SLR appears approximately where $S(\omega)$ exhibits a pole, at $\omega_{\mathrm{SLR}} = (2\pi c/\lambda_{\mathrm{SLR}})$. At this spectral location, the individual responses of all of the nanostructures contribute cooperatively[41].

Equation (2) may be used to predict the optical response of the entire metasurface, including the behavior of its many resonances, as a function of the geometry of its nanostructures (see “Methods”): by changing the geometry of a nanostructure[12,42], its individual resonance wavelength λ_{LSPR}, oscillator strength A_0,

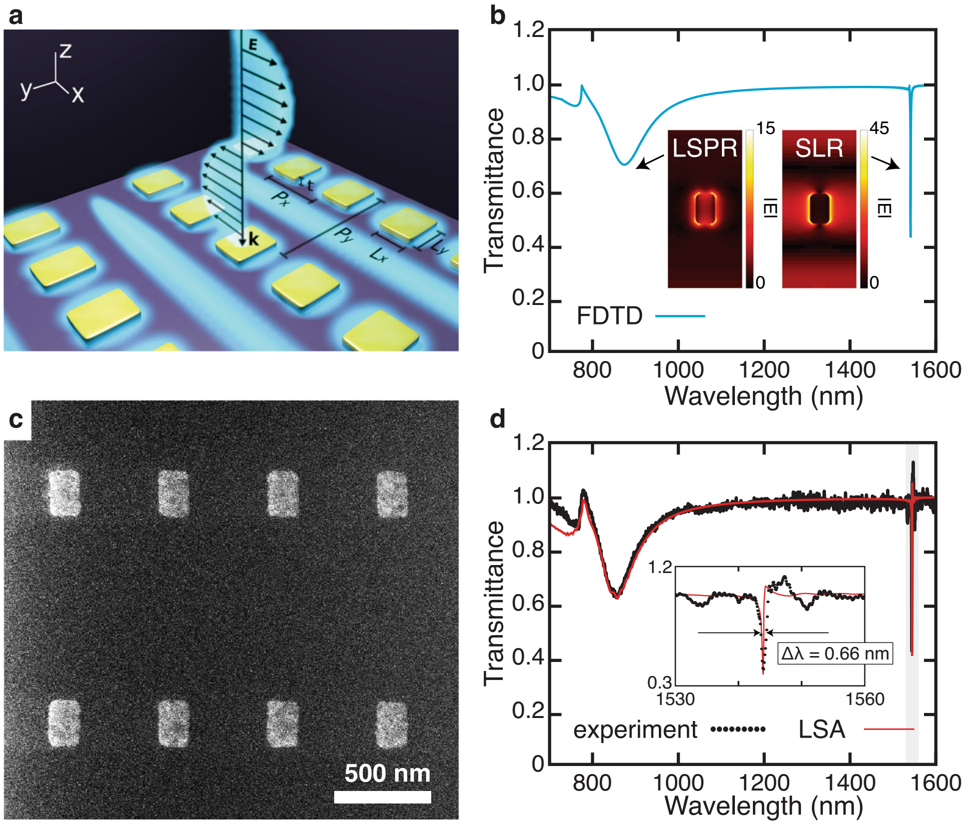

Fig. 1 High-Q metasurface nanocavities using arrays of plasmonic nanostructures. **a** Schematic of the metasurface consisting of a rectangular array of rectangular gold nanostructures. Here $L_x = 130$ nm, $L_y = 200$ nm, $t = 20$ nm, $P_x = 500$ nm, and $P_y = 1060$ nm. The blue shaded regions illustrate the electric field, reproducing the mode structure in the inset of **b**. **b** Numerical (FDTD) calculations of the transmission spectrum of this metasurface for x-polarized light. Both the LSPR and the SLR are observed in these results. Inset: The simulated magnitude of the electric field $|E|$ for the entire unit cell of both LSPR and SLR modes in the x–y plane that bisects the nanoparticles. The color bar indicates the relative magnitude when normalized to the incident plane wave. **c** Helium ion microscopic image of the fabricated metasurface prior to cladding deposition. **d** Measured transmission spectrum (black dots) and fits to semi-analytic calculations (LSA, red line). Inset: Zoomed plot of the highlighted region in **d**. Fitting the measurement to a Lorentzian function yields a linewidth of $\Delta\lambda = 0.66$ nm, corresponding to $Q = 2340$ (see Supplementary Sec. S1: Q-factor extraction).

and damping constant γ are all modified. In turn, adjusting these values changes the polarizability of the nanostructures throughout the spectrum, including at the SLR wavelength $\alpha(\omega_{\text{SLR}})$, and therefore also the response of the entire metasurface at this wavelength $\alpha^*(\omega_{\text{SLR}})$. Here we adjust the above parameters by changing the dimensions of the nanostructures (see "Methods"), while the parameters could be alternatively modified by considering altogether different nanostructure shapes, such as nanorings, nanorods, or core–shell nanoparticles[42]. By contrast, the spectral location of the SLR wavelength is dictated mainly by the lattice period and the background index $\lambda_{\text{SLR}} \approx nP$[32,43,44]. In other words, the lattice configuration governs the presence of the SLR, and the nanostructure geometry dictates its coupling efficiency to free space. Indeed, recent theoretical studies in this platform have shown Q-factors on the order of 10^3 by properly selecting the dimensions of the individual nanostructures[31,33].

We reproduce this dependence in this platform explicitly by plotting the calculated transmission of a metasurface (see "Methods") as a function of nanostructure resonance wavelength λ_{LSPR} (Fig. 2). (The dependence of the SLR behavior on particle dimensions, which is connected to the resonance wavelength, is also demonstrated using full-wave simulations in Supplementary Sec. S3: Dependence of SLR behavior on particle dimensions.) Here we hold the oscillator strength A_0 and damping term γ constant and slowly increase the nanoparticle resonance wavelength λ_{LSPR}. Note that the resonance position differs slightly from the position of the dip due to the incorporation of a long-wavelength correction[45]. In Fig. 2b, c, the SLR wavelength does not change substantially from its location around $\lambda_{\text{SLR}} = 1542$ nm; however, the extinction ratio ΔT and the linewidth $\Delta\lambda$ of the resonance change dramatically. In Fig. 2d, we plot the extracted Q-factors for these SLRs and for other values of A_0, as well (see Supplementary Sec. S1: Q-factor extraction for the fits). Based on well-established relationships between nanoparticle geometry and polarizability[10,46], this A_0 range corresponds to a change in nanoparticle volume of roughly 20%. We find that, for every given value of A_0, there is a corresponding λ_{LSPR} for which light couples optimally to the lattice resonance at λ_{SLR} and produces the highest Q-factor. The optimal conditions are therefore found in the balance between increasing α relative to P_y (i.e., increasing coupling strength) and maintaining a large spectral gap between λ_{LSPR} and λ_{SLR} (i.e., limiting Ohmic losses associated with metallic nanoparticles). The trade-off between coupling and loss is a traditional one for optical resonators and is reproduced in the SLR-based metasurface platform[47].

Effect of array size. Next, we study the dependence of the Q-factor on the array size. For certain metasurfaces, it has already been predicted that larger array sizes lead to better device performance[36,48]. This dependence makes some intuitive sense—since high-Q operation requires low absorption losses, we are

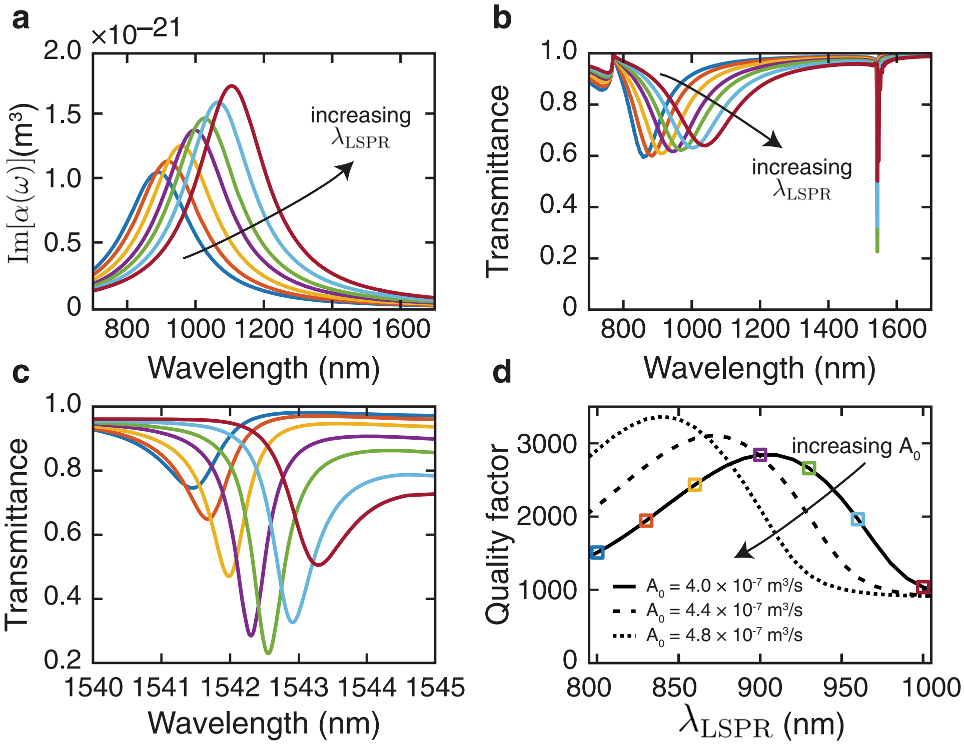

Fig. 2 Coupling to a surface lattice resonance. The colors in **a**–**d** are consistent, corresponding to the same type of nanoparticle. **a** The imaginary part of the individual particle polarizability for various nanostructures with increasing resonance wavelength λ_{LSPR}, holding both the oscillator strength A_0 and the damping term γ fixed. Here λ_{LSPR} is tuned from 800 to 1000 nm. **b** Simulated broadband transmission spectra for gold nanostructure arrays as a function of tuning λ_{LSPR}. By tuning the LSPR wavelength, the extinction factor of the SLR is observed to change near $\lambda = 1542$ nm. While λ_{LSPR} changes dramatically, the SLR wavelength λ_{SLR} does not change much. **c** Zoomed-in plot of the SLR in **b**. **d** The Q-factor of the surface lattice resonance as a function of λ_{LSPR} for various oscillator strengths A_0. The optimal LSPR wavelength for a high-Q SLR changes as a function of A_0. The oscillator strength A_0 increases from 3.98×10^{-7} to 4.77×10^{-7} m³/s, roughly corresponding to a 20% increase in the particle volume. The squares indicate the Q values extracted from the curves in **c**.

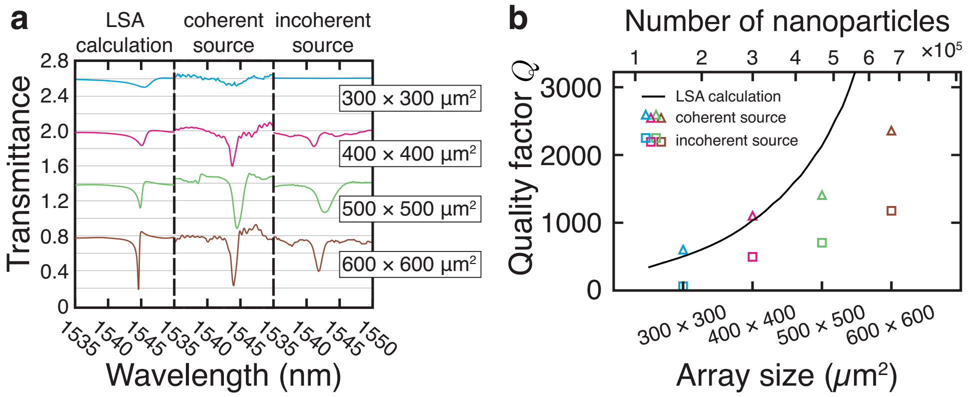

Fig. 3 Effects of array size and spatial coherence of light source. a Calculated and measured (using coherent and incoherent sources) transmission spectra for identical metasurface arrays of varying size (from top to bottom: 300 × 300, 400 × 400, 500 × 500, and 600 × 600 µm², respectively). The spectra are offset for clarity, and each vertical division corresponds to an increment of $\Delta T = 0.2$ in transmittance. **b** The Q-factors extracted from Lorentzian fits to the calculations and to the measurements shown in **a**. An increase in the number of nanostructures in the array results in an increase in the estimated Q-factors. Additionally, the observed Q-factor is globally larger for each array when measured using the coherent source.

required to operate the device far from the LSPR. However, at a sufficiently far operating wavelength, the scattering cross-section is also small, resulting in each antenna scattering very weakly. Consequently, far from the LSPR, one requires a sufficiently large number of scatterers to build up the resonance. Equivalently, the standing wave mode in an SLR consists of counter-propagating surface waves; therefore, a larger array provides an expanded propagation length in the cavity to support these modes.

To examine the dependence of Q on the number of nanostructures explicitly, we fabricated and characterized a series of devices of increasing array size. Figure 3 shows the resulting transmission spectra, as well as their corresponding semi-analytic predictions. The observed Q-factors increase monotonically as a function of array size (Fig. 3b—see Supplementary Sec. S1: Q-factor extraction for the fits). In the smallest array (300 × 300 µm²), the SLR is almost imperceptible. This trend might help explain the relatively low Q values observed in previous studies[9,30,31,36] where array sizes were typically no larger than 250 × 250 μm^2, likely due to the relatively slow write-speed of the electron-beam lithography process necessary for fabrication[26,37]. By contrast, our devices have array sizes reaching up to 600 × 600 μm^2 (see Supplementary Sec. S4: Image of the device).

The role of spatial coherence. Finally, it is of critical importance to consider all aspects of the characterization system in order to get an accurate measurement of the Q-factor. In particular, we have found that the spatial coherence of the probe beam was critical to obtaining a clean measurement of the dip in transmission indicating a resonance. A spatially coherent beam, such as a laser, excites every region of the metasurface in phase, producing a resonance feature that is both deeper and narrower compared to using a spatially incoherent source. Additionally, the higher-order modes of the lattice are more sensitive to angular variance in the measurements, leading to broader peaks when using incoherent sources[35]. Furthermore, in our particular experiment, the transmitted signal from our coherent supercontinuum source was both brighter and could also be better collimated than our incoherent thermal source. Therefore, the light collected from the metasurface array could be isolated with a smaller pinhole in the image plane, selecting the signal coming from nanostructures at the center of the array with a more uniform collective response.

In Fig. 3, we compare the performance of the metasurface when illuminated using different light sources: a broadband supercontinuum laser (i.e., a well-collimated coherent source), and a tungsten-halogen lamp. The comparison between these measurements indicates that the Q increases with the coherence of the light source—using the thermal light source reduces the Q-factor by a factor of 2–5 when compared to the laser. Additionally, it decreases the resonance coupling strength, as is evident from the reduced extinction ratio of the SLRs. Figure 3b summarizes the Q-factors extracted from these measurements and compares them to numerical predictions. LSA calculations predict that Q-factors increase as a function of array size; this trend continues for both smaller and larger devices than those probed experimentally. Note that, even when using an incoherent source, the largest array still produces a very large Q-factor ($Q \sim 1000$). The observation of such a high Q using an incoherent source reinforces the validity of our aforementioned metasurface design criteria—that is, the importance of the choice of nanostructure geometry and of the array size.

In some of the measurements, the value for the normalized transmittance can be seen to exceed unity (i.e., $T > 1$). We speculate that this is because the nanostructures aid in coupling to the substrate, reducing the reflections from the first interface.

Discussion

Despite promising results, Fig. 3b also highlights some discrepancies between the simulation and the experiment for the largest arrays, notably reducing the measured Q-factors. This disparity could be due to multiple reasons, which we enumerate below. First, the prediction produced by the LSA might be overestimating the Q by assuming that each nanoparticle is excited with a constant-valued local field. This assumption cannot be entirely correct for a Gaussian beam and a finite array, where particles closer to the boundaries of the array feel a weaker local field than the particles near the center. Second, the fabrication procedure produces stitching errors, which become more important for larger arrays. This added disorder might contribute to the reduction in Q. Lastly, the Q-factors might be limited due to additional measurement considerations, such as the finite coherence length of the light source or imperfections with the collimation.

In this work, we only looked into rectangular nanoparticles in rectangular lattices. Based on LSA calculations and the discrete-dipole approximation (DDA) used in previous work[26,39,44,49,50], it is evident that any particle geometry (e.g., cylindrical, rectangular, or triangular) that can be approximated by dipoles with the same Lorentzian parameters A_0, λ_{LSPR}, and γ will yield an identical SLR Q-factor. For nanoparticles that cannot be modeled by dipoles—regardless of the particle geometry—the SLR Q-factor will be the same provided that the polarizability at λ_{SLR} remains the same. Regarding different lattice configurations, the spectral responses of other lattice geometries such as hexagonal, orthorhombic, and kagome are likely to be different than the rectangular lattice design we have adopted. However, lattice sums can be computed for these regular lattices, and therefore they can also be treated using our method. Therefore, strategies presented in this work are largely blind to the specific lattice arrangements, and its conclusions will be helpful in obtaining resonances with large-Q factors in other geometries.

The Q-factors for the type of device presented here could be further increased, however, by considering larger arrays or by further optimizing the nanostructure dimensions—instead of rectangles, a more intricate nanostructure shape could tailor the Lorentzian dipole coefficients A_0, λ_{LSPR}, and γ more independently to allow for optimal coupling and higher extinction ratios. These shapes include L-shaped antennas[51], split-ring resonators[52], and others that also exhibit higher-order moments[53,54]. Alternatively, a nanoparticle with a large aspect ratio could increase coupling to more neighboring particles using out-of-plane oscillations[44]. Finally, the metasurface shown here can be combined with other established methods to enable multiple simultaneous resonances[39,50,55].

Table 1 contains a short survey of the literature on metasurface nanocavities. Other than the reported Q-factors, we have included, when available, information that is relevant to compare their work against ours, such as the operating wavelength, the material platform, the array size, and the type of light source used. Our work demonstrates the highest Q by an order of magnitude among metasurfaces with plasmonic components and is exceeded only by metasurfaces that incorporate a bound state in the continuum (BIC).

To summarize, we have fabricated and experimentally demonstrated a plasmonic metasurface nanoresonator with a high Q-factor, which is in excellent agreement with numerical predictions. Our work presents the experimental demonstration of a high-Q plasmonic metasurface nanoresonator with an order-of-magnitude improvement over prior art (see Table 1). We have found that the observed Q-factor obtained from an SLR may be limited by a poor choice of nanostructure dimensions, a small array size, or poor spatial coherence of the source illumination; we hypothesize that one or many of these factors may have been the cause for the low Q-factors reported in previous experiments featuring SLRs. Additionally, our device follows simple design principles that can be easily expanded upon to enable multiple resonances to fully tailor the transmission spectrum of a wavelength-scale surface. Our result highlights the potential of SLR-based metasurfaces and expands the capabilities of plasmonic nanoparticles for many optical applications.

Methods

Simulations

Finite-difference time domain (FDTD). Full-wave simulations were performed using a commercial three-dimensional FDTD solver. A single unit cell was simulated using periodic boundary conditions in the in-plane dimensions and perfectly matched layers in the out-of-plane dimension. The structures were modeled using

Table 1 Summary of experimentally obtained *Q*-factors in metasurfaces.

Mechanism	Q	λ (nm)	Material	Light source	Array size (μm²)	Reference
SLR	**2340**	**1550**	**Au NPs**	**Supercontinuum**	**600 × 600**	**This work**
LSPR	<10	700	Au NPs	Tungs.-halogen lamp	3000 × 3000	61
SLR	25	930	Au NPs	Collimated source	135 × 135	27
SLR	30	850	Au NPs	Tungs.-halogen lamp	3000 × 3000	61
SLR	40–60	600	Au NPs	Ellipsometer	200 × 200	28
SLR	60	800	Au NPs	Tungs.-halogen lamp	35 × 35	26
SLR	150	764	Au NPs	Tungs.-halogen lamp	N/A	62
SLR	230	900	Au NPs	Tungs.-halogen lamp	~10,000 × 10,000	63
SLR	300	1500	Au nanostripes	Tungs.-halogen lamp	300 × 100	40
SLR	330	648	Ag NPs	Tungs.-halogen lamp	2500 × 2500	37
SLR	430	860	Au NPs	Tungs.-halogen lamp	1000 × 1000	34
Mirror image	200	5000	ITO nanorods	Collimated source	N/A	35
EIT	483	1380	Si	Tungs.-halogen lamp	225 × 240	64
Fano resonance	65	THz	Al particles	THz laser	10,000 × 10,000	65
Fano resonance	100	THz	Au Assym. NPs	FTIR	150 × 150	66
Fano resonance	350	1000	Si	N/A	N/A	67
Fano resonance	600	1000	GaAs	N/A	N/A	67
BIC	2750	825	GaAs	Laser	60 × 108	68
Quasi-BIC	18,511	1588.4	Si	Laser	15 × 15	69

The results presented in this work are in bold.
Q quality factor, *λ* resonance wavelength, *NP* nanoparticle, *SLR* surface lattice resonance, *LSPR* localized surface plasmon resonance, *EIT* electromagnetically induced transparency, *BIC* bound state in the continuum.

fully dispersive optical material properties for silica[56] and for gold[57]. Minimal artificial absorption ($\mathrm{Im}(n) \sim 10^{-4}$) was added to the background medium to reduce numerical divergences.

Lattice sum approach. The LSA is a variant of the DDA method[58]. It is a semi-analytic calculation method that has been found to produce accurate results for plasmonic arrays[39,41,44]. The main assumption in LSA when compared to DDA is that the dipole moments of all interacting nanoparticles are assumed to be identical[44]. The main benefit of using LSA for our application compared to alternatives such as FDTD is its capability to model finite-sized arrays with an arbitrary number of nanostructures, by assuming that the overall response of the array closely follows the responses of the nanoparticles at the center of the array. By comparing simulations performed using the LSA against the DDA, this assumption has also been found to be quite accurate[44]. Its rapid simulation time makes it a useful tool for iterating many simulations to study trends and behaviors of entire metasurfaces, especially for finite array effects, such as the effect of array size on the Q-factor.

Using the LSA approach, the dipole moment **p** of any particle in the array is written as

$$\mathbf{p} = \frac{\epsilon_0 \alpha(\omega) \mathbf{E}_{\mathrm{inc}}}{1 - \epsilon_0 \alpha(\omega) S(\omega)} \equiv \epsilon_0 \alpha^{*}(\omega) \mathbf{E}_{\mathrm{inc}}, \tag{3}$$

where the effect of inter-particle coupling is incorporated in the lattice sum S and α^{*} is the effective polarizability. This equation produces Eq. (2) in the main text. The calculations presented in this work also incorporate a modified long-wavelength correction[45]:

$$\alpha(\omega) \rightarrow \frac{\alpha_{\mathrm{static}}(\omega)}{1 - \frac{2}{3} i k^3 \alpha_{\mathrm{static}}(\omega) - \frac{k^2}{l} \alpha_{\mathrm{static}}(\omega)}, \tag{4}$$

where k is the wavenumber in the background medium $k = (2\pi n/\lambda)$ and l is the effective particle radius. Also here, minimal artificial absorption ($\mathrm{Im}(n) = 6 \times 10^{-4}$) was added to the refractive index $n = 1.452$ of the background medium to reduce numerical divergences associated with the approach when considering large arrays[41]. We set $l = 180$ nm for all calculations. The static polarizability of the nanoparticle is given by

$$\alpha_{\mathrm{static}}(\omega) = \frac{A_0}{\omega - \omega_0 - i\gamma}, \tag{5}$$

where A_0 is the oscillator strength, $\omega_0 = 2\pi c/\lambda_{\mathrm{LSPR}}$ corresponds to the nanoparticle resonance frequency, and γ is the damping term.

For a planar array of N dipoles, the lattice sum term S is

$$S(\omega) = \sum_{j=1}^{N} \frac{\exp(\mathrm{i}kr_j)}{\epsilon_0 r_j} \left[k^2 + \frac{(1 - \mathrm{i}kr_j)(3\cos^2\theta_j - 1)}{r_j^2} \right], \tag{6}$$

where r_j is the distance to the jth dipole and θ_j is the angle between $\mathbf{r}_j$ and the dipole moment **p**.

The optical transmission spectra can be obtained by using the optical theorem, $\mathrm{Ext} \propto k\mathrm{Im}(\alpha^{*})$[59]:

$$T(\omega) = 1 - \frac{4\pi k}{P_x P_y} \mathrm{Im}[\alpha^{*}(\omega)], \tag{7}$$

where P_x and P_y are the lattice constants along the x and y dimensions, respectively.

To produce the plots in Fig. 1d, we performed an LSA calculation using the following parameters for the single dipole: $\lambda_{\mathrm{LSPR}} = 780$ nm; $A_0 = 3.46 \times 10^{-7}$ m^3/s, $\gamma = 8.5 \times 10^{13}$ s^{-1}. LSA parameters were determined by matching to FDTD data. The lattice constants were $P_x = 500$ nm and $P_y = 1067.5$ nm. The total array size was 600 × 600 μm^2, corresponding to $N_x = 1200 \times N_y = 562$ nanostructures, respectively. The LSA calculations in Fig. 3 used these same parameters but varied the total number of nanostructures.

To calculate the figures in Fig. 2a, c, we performed a series of LSA calculation using the following parameters for the particle: $A_0 = 3.98 \times 10^{-7}$ m^3/s, $\gamma = 1/[2\pi\,(2.1\ \mathrm{fs})] \approx 7.6 \times 10^{13}$ s^{-1}. The dipole resonance wavelengths λ_{LSPR} were 800, 833, 866, 900, 933, 966, and 1000 nm, respectively. Based on the performed FDTD simulations, these resonance wavelengths could correspond to rectangular gold nanostructures with widths of $L_x = 110$, 120, 130, 140, 150, 160, and 170 nm, respectively, if $L_y = 190$ nm, and $t = 20$ nm. (Note that, in the main text, $L_y =$ 200 nm). See Supplementary Sec. S3: Dependence of SLR behavior on particle dimensions for the corresponding simulations. The lattice constants were $P_x =$ 500 nm and $P_y = 1060$ nm, respectively. The total array size was 600 × 600 μm^2, corresponding to $N_x = 1200 \times N_y = 567$ nanostructures, respectively. To obtain Fig. 2d, a series of LSA calculations were performed for many values of λ_{LSPR} ranging from 800 to 1000 nm, and the Q-factors were extracted from the results using a fit to a Lorentzian. The curves in Fig. 2d come from repeating this procedure with oscillator strengths of $A_0 = 3.98 \times 10^{-7}$, 4.38×10^{-7}, and 4.77×10^{-7} m^3/s.

Device details. We fabricated different metasurface devices with array sizes of 300 × 300, 400 × 400, 500 × 500, and 600 × 600 μm^2, with a corresponding number of participating nanostructures of 600 × 284, 800 × 378, 1000 × 472, and 1200 × 567, respectively. The lattice constants of the rectangular arrays are $P_x = 500$ nm × $P_y = 1060$ nm. The dimensions of the rectangular gold nanostructures are $L_x =$ 130 nm × $L_y = 200$ nm, with a thickness of $t = 20$ nm. The lattice is embedded within a homogeneous background $n \approx 1.46$.

Fabrication. The metasurfaces are fabricated using a standard metal lift-off process. We start with a fused silica substrate. We deposit a silica undercladding layer using sputtering. We then define the pattern using electron-beam lithography in a positive tone resist bi-layer with the help of a commercial conductive polymer. The mask was designed using shape-correction proximity error correction[60] to correct for corner rounding. Following development, a thin adhesion layer of chromium (0.2-nm thick) is deposited using e-beam evaporation, followed by a layer of gold deposited using thermal evaporation. Lift-off is performed, and a final protective silica cladding layer is deposited using sputtering. The initial and final silica layers are sputtered using the same tool under the same conditions to ensure that the environment surrounding the metasurface is completely homogeneous. Before characterization, the surface of the device is then covered in index-matching oil. The backside of the silica substrate is coated with an anti-reflective coating to minimize substrate-related etalon fringes.

Characterization. See Supplementary Sec. S5: Experimental set-up for a schematic of the experimental set-up.

Coherent light measurements. To measure the transmission spectra, we flood-illuminated all of the arrays in the sample using a collimated light beam from a broadband supercontinuum laser source. The wavelength spectrum of the source ranges from $\lambda = 470$ to 2400 nm. The beam comes from normal incidence along the z-direction with light polarized in the x-direction. The incident polarization is controlled using a broadband linear polarizing filter. Light transmitted by the metasurface is then imaged by a $f = 35$ mm lens, and a 100-μm pinhole is placed in the image plane to select the desired array. The transmitted light is collected in a large core (400 μm) multimode fiber and analyzed using an optical spectrum analyzer and is normalized to a background trace of the substrate without gold nanostructures. The resolution of the spectrometer is set to 0.01 nm.

Incoherent light measurements. Here the experiment goes as above, but the samples are excited using a collimated tungsten-halogen light source (ranging from $\lambda = 300$ to 2600 nm) and a 400-μm pinhole.

Data availability

The data that support the plots within this paper and other findings of this study are available from the corresponding author upon reasonable request.

Code availability

The code used to analyze the data and the related simulation files are available from the corresponding author upon reasonable request.

Received: 29 June 2020; Accepted: 14 January 2021;
Published online: 12 February 2021

References

1. Anker, J. et al. Biosensing with plasmonic nanosensors. *Nat. Mater.* **7**, 442–453 (2008).
2. Nie, S. & Emory, S. R. Probing single molecules and single nanoparticles by surface-enhanced Raman scattering. *Science* **275**, 1102–1106 (1997).
3. Willets, K. A. & Van Duyne, R. P. Localized surface plasmon resonance spectroscopy and sensing. *Annu. Rev. Phys. Chem.* **58**, 267–297 (2007).
4. Azzam, S. I. et al. Ten years of spasers and plasmonic nanolasers. *Light Sci. Appl.* **9**, 90 (2020).
5. Ren, M. et al. Nanostructured plasmonic medium for terahertz bandwidth all-optical switching. *Adv. Mater.* **23**, 5540–5544 (2011).
6. Kauranen, M. & Zayats, A. V. Nonlinear plasmonics. *Nat. Photonics* **6**, 737 (2012).
7. Yu, N. et al. Light propagation with phase discontinuities: generalized laws of reflection and refraction. *Science* **334**, 333–337 (2011).
8. Won, R. The rise of plasmonic metasurfaces. *Nat. Photonics* **11**, 462–464 (2017).
9. Meinzer, N., Barnes, W. L. & Hooper, I. R. Plasmonic meta-atoms and metasurfaces. *Nat. Photonics* **8**, 889–898 (2014).
10. Maier, S. A. *Plasmonics: Fundamentals and Applications* (Springer, 2007).
11. Boyd, R. W. *Nonlinear Optics* 4th edn (Academic, 2020).
12. Oldenburg, S. J., D., A. R., Westcott, S. L. & Halas, N. J. Nanoengineering of optical resonances. *Chem. Phys. Lett.* **288**, 243–247 (1998).
13. Novotny, L. & Van Hulst, N. Antennas for light. *Nat. Photonics* **5**, 83–90 (2011).
14. Zhang, X., Choi, H. S. & Armani, A. M. Ultimate quality factor of silica microtoroid resonant cavities. *Appl. Phys. Lett.* **96**, 153304 (2010).
15. Ji, X. et al. Ultra-low-loss on-chip resonators with sub-milliwatt parametric oscillation threshold. *Optica* **4**, 619–624 (2017).
16. Asano, T., Ochi, Y., Takahashi, Y., Kishimoto, K. & Noda, S. Photonic crystal nanocavity with a Q factor exceeding eleven million. *Opt. Express* **25**, 1769 (2017).
17. Krasnok, A., Tymchenko, M. & Alù, A. Nonlinear metasurfaces: a paradigm shift in nonlinear optics. *Mater. Today* **21**, 8–21 (2018).
18. Celebrano, M. et al. Mode matching in multiresonant plasmonic nanoantennas for enhanced second harmonic generation. *Nat. Nanotechnol.* **10**, 412–417 (2015).
19. Zhou, W. et al. Lasing action in strongly coupled plasmonic nanocavity arrays. *Nat. Nanotechnol.* **8**, 506–511 (2013).
20. Michaeli, L., Keren-Zur, S., Avayu, O., Suchowski, H. & Ellenbogen, T. Nonlinear surface lattice resonance in plasmonic nanoparticle arrays. *Phys. Rev. Lett.* **118**, 243904 (2017).
21. Luo, L. et al. Broadband terahertz generation from metamaterials. *Nat. Commun.* **5**, 3055 (2014).
22. Choi, D.-Y. et al. Imaging-based molecular barcoding with pixelated dielectric metasurfaces. *Science* **360**, 1105–1109 (2018).
23. Sain, B., Meier, C. & Zentgraf, T. Nonlinear optics in all-dielectric nanoantennas and metasurfaces: a review. *Adv. Photonics* **1**, 1 (2019).
24. Koshelev, K. et al. Subwavelength dielectric resonators for nonlinear nanophotonics. *Science* **367**, 288–292 (2020).
25. Nordlander, P., Oubre, C., Prodan, E., Li, K. & Stockman, M. I. Plasmon hybridization in nanoparticle dimers. *Nano Lett.* **4**, 899–903 (2004).
26. Auguié, B. & Barnes, W. L. Collective resonances in gold nanoparticle arrays. *Phys. Rev. Lett.* **101**, 143902 (2008).
27. Chu, Y., Schonbrun, E., Yang, T. & Crozier, K. B. Experimental observation of narrow surface plasmon resonances in gold nanoparticle arrays. *Appl. Phys. Lett.* **93**, 181108 (2008).
28. Kravets, V., Schedin, F. & Grigorenko, A. Extremely narrow plasmon resonances based on diffraction coupling of localized plasmons in arrays of metallic nanoparticles. *Phys. Rev. Lett.* **101**, 087403 (2008).
29. Vecchi, G., Giannini, V. & Rivas, J. G. Surface modes in plasmonic crystals induced by diffractive coupling of nanoantennas. *Phys. Rev. B* **80**, 201401 (2009).
30. Kravets, V. G., Kabashin, A. V., Barnes, W. L. & Grigorenko, A. N. Plasmonic surface lattice resonances: a review of properties and applications. *Chem. Rev.* **118**, 5912–5951 (2018).
31. Khlopin, D. et al. Lattice modes and plasmonic linewidth engineering in gold and aluminum nanoparticle arrays. *J. Opt. Soc. Am. B* **34**, 691 (2017).
32. Zou, S., Janel, N. & Schatz, G. C. Silver nanoparticle array structures that produce remarkable narrow plasmon line shapes. *J. Chem. Phys.* **120**, 10871–10875 (2004).
33. Zakomirnyi, V. I. et al. Refractory titanium nitride two-dimensional structures with extremely narrow surface lattice resonances at telecommunication wavelengths. *Appl. Phys. Lett.* **111**, 123107 (2017).
34. Deng, S. et al. Ultranarrow plasmon resonances from annealed nanoparticle lattices. *Proc. Natl. Acad. Sci. USA* **117**, 23380 (2020).
35. Li, S. Q. et al. Ultra-sharp plasmonic resonances from monopole optical nanoantenna phased arrays. *Appl. Phys. Lett.* **104**, 231101 (2014).
36. Rodriguez, S. R. K., Schaafsma, M. C., Berrier, A. & Gomez Rivas, J. Collective resonances in plasmonic crystals: size matters. *Phys. B Condens. Matter* **407**, 4081–4085 (2012).
37. Le-Van, Q. et al. Enhanced quality factors of surface lattice resonances in plasmonic arrays of nanoparticles. *Adv. Opt. Mater.* **7**, 1801451 (2019).
38. Auguié, B., Bendana, X. M., Barnes, W. L. & de Abajo, F. J. G. Diffractive arrays of gold nanoparticles near an interface: critical role of the substrate. *Phys. Rev. B* **82**, 155447 (2010).
39. Reshef, O. et al. Multiresonant high-Q plasmonic metasurfaces. *Nano Lett.* **19**, 6429–6434 (2019).
40. Thackray, B. D. et al. Super-narrow, extremely high quality collective plasmon resonances at telecom wavelengths and their application in a hybrid graphene-plasmonic modulator. *Nano Lett.* **15**, 3519–3523 (2015).
41. Markel, V. A. Divergence of dipole sums and the nature of non-Lorentzian exponentially narrow resonances in one-dimensional periodic arrays of nanospheres. *J. Phys. B* **38**, L115–L121 (2005).
42. Teperik, T. & Degiron, A. Design strategies to tailor the narrow plasmon-photonic resonances in arrays of metallic nanoparticles. *Phys. Rev. B* **86**, 245425 (2012).
43. Offermans, P. et al. Universal scaling of the figure of merit of plasmonic sensors. *ACS Nano* **5**, 5151–5157 (2011).
44. Huttunen, M. J., Dolgaleva, K., Törmä, P. & Boyd, R. W. Ultra-strong polarization dependence of surface lattice resonances with out-of-plane plasmon oscillations. *Opt. Express* **24**, 28279–28289 (2016).
45. Jensen, T., Kelly, L., Lazarides, A. & Schatz, G. C. Electrodynamics of noble metal nanoparticles and nanoparticle clusters. *J. Cluster Sci.* **10**, 295–317 (1999).
46. Huang, C.-p, Yin, X.-g, Huang, H. & Zhu, Y.-y Study of plasmon resonance in a gold nanorod with an LC circuit model. *Opt. Express* **17**, 6407–6413 (2009).
47. McKinnon, W. R. et al. Extracting coupling and loss coefficients from a ring resonator. *Opt. Express* **17**, 17010 (2009).
48. Zundel, L. & Manjavacas, A. Finite-size effects on periodic arrays of nanostructures. *J. Phys. Photonics* **1**, 015004 (2019).
49. Huttunen, M. J., Rasekh, P., Boyd, R. W. & Dolgaleva, K. Using surface lattice resonances to engineer nonlinear optical processes in metal nanoparticle arrays. *Phys. Rev. A* **97**, 053817 (2018).
50. Huttunen, M. J., Reshef, O., Stolt, T., Dolgaleva, K. & Boyd, R. W. Efficient nonlinear metasurfaces by using multiresonant high-Q plasmonic arrays. *J. Opt. Soc. Am. B* **36**, 118 (2019).

51. Husu, H., Mäkitalo, J., Laukkanen, J., Kuittinen, M. & Kauranen, M. Particle plasmon resonances in l-shaped gold nanoparticles. *Opt. Express* **18**, 16601–16606 (2010).
52. Corrigan, T. D. et al. Optical plasmonic resonances in split-ring resonator structures: an improved LC model. *Opt. Express* **16**, 19850–19864 (2008).
53. Barnes, W. L. Particle plasmons: why shape matters. *Am. J. Phys.* **84**, 593–601 (2016).
54. Alaee, R., Rockstuhl, C. & Fernandez-Corbaton, I. An electromagnetic multipole expansion beyond the long-wavelength approximation. *Opt. Commun.* **407**, 17–21 (2018).
55. Baur, S., Sanders, S. & Manjavacas, A. Hybridization of lattice resonances. *ACS Nano* **12**, 1618–1629 (2018).
56. Palik, E. D. *Handbook of Optical Constants of Solid* (Academic, 1985).
57. Johnson, P. & Christy, R. Optical constants of the noble metals. *Phys. Rev. B* **6**, 4370–4379 (1972).
58. Oldenburg, S. J., D., A. R., Westcott, S. L. & Halas, N. J. Discrete-dipole approximation for scattering calculations. *J. Opt. Soc. Am. A* **11**, 1491–1499 (1994).
59. Jackson, J. D. *Classical Electrodynamics* 3rd edn (Wiley, 1999).
60. Schulz, S. A. et al. Quantifying the impact of proximity error correction on plasmonic metasurfaces [Invited]. *Opt. Mater. Express* **5**, 2798–2803 (2015).
61. Rodriguez, S. R. et al. Coupling bright and dark plasmonic lattice resonances. *Phys. Rev. X* **1**, 021019 (2011).
62. Kravets, V. G., Schedin, F., Kabashin, A. V. & Grigorenko, A. N. Sensitivity of collective plasmon modes of gold nanoresonators to local environment. *Opt. Lett.* **35**, 956–958 (2010).
63. Yang, A. et al. Real-time tunable lasing from plasmonic nanocavity arrays. *Nat. Commun.* **6**, 6939 (2015).
64. Yang, Y., Kravchenko, I. I., Briggs, D. P. & Valentine, J. All-dielectric metasurface analogue of electromagnetically induced transparency. *Nat. Commun.* **5**, 5753 (2014).
65. Singh, R. et al. Ultrasensitive terahertz sensing with high-Q Fano resonances in metasurfaces. *Appl. Phys. Lett.* **105**, 171101 (2011).
66. Wu, C. et al. Fano-resonant asymmetric metamaterials for ultrasensitive spectroscopy and identification of molecular monolayers. *Nat. Mater.* **11**, 69–75 (2011).
67. Campione, S. et al. Broken symmetry dielectric resonators for high quality factor fano metasurfaces. *Nano Lett.* **3**, 2362–2367 (2016).
68. Ha, S. T. et al. Directional lasing in resonant semiconductor nanoantenna arrays. *Nat. Nanotechnol.* **13**, 1042–1047 (2018).
69. Liu, Z. et al. High-Q quasibound states in the continuum for nonlinear metasurfaces. *Phys. Rev. Lett.* **123**, 253901 (2019).

Acknowledgements

Fabrication in this work was performed in part at the Centre for Research in Photonics at the University of Ottawa (CRPuO). The authors acknowledge support from the Canada Excellence Research Chairs (CERC) Program, the Canada Research Chairs (CRC) Program, and the Natural Sciences and Engineering Research Council of Canada (NSERC) Discovery funding program. M.S.B.-A. acknowledges the support of the Ontario Graduate Scholarship (OGS), the University of Ottawa Excellence Scholarship, and the University of Ottawa International Experience Scholarship. O.R. acknowledges the support of the Banting Postdoctoral Fellowship of the NSERC. Y.M. was supported by the Mitacs Globalink Research Award. M.J.H. acknowledges the support of the Academy of Finland (Grant No. 308596) and the Flagship of Photonics Research and Innovation (PREIN) funded by the Academy of Finland (Grant No. 320165).

Author contributions

M.S.B.-A., O.R., and M.J.H. conceived the basic idea for this work. O.R. and M.S.B.-A. performed the FDTD simulations. M.J.H., M.S.B.-A., and O.R. performed the lattice sum calculations. O.R. and G.C. fabricated the device. M.Z.A. and M.J.H. designed the preliminary experimental set-up. M.S.B.-A. and Y.M. carried out the measurements. O.R., M.S.B.-A., and Y.M. analyzed the experimental results. J.U., B.T.S., J.-M.M., M.J.H., R.W. B., and K.D. supervised the research and the development of the manuscript. M.S.B.-A. and O.R. wrote the first draft of the manuscript. All co-authors subsequently took part in the revision process and approved the final copy of the manuscript. Portions of this work were presented at the 2020 SPIE Photonics West Conference in San Francisco, CA.

Competing interests

The authors declare no competing interests.

Additional information

Supplementary information The online version contains supplementary material available at https://doi.org/10.1038/s41467-021-21196-2.

Correspondence and requests for materials should be addressed to O.R.

Peer review information *Nature Communications* thanks the anonymous reviewers for their contribution to the peer review of this work.

Reprints and permission information is available at http://www.nature.com/reprints

Supplementary Information

Below is the supplementary information for *Ultra-high-Q resonances in plasmonic metasurfaces* by M. Saad Bin-Alam, Orad Reshef, Yaryna Mamchur, M. Zahirul Alam, Graham Carlow, Jeremy Upham, Brian T. Sullivan, Jean-Michel Ménard, Mikko J. Huttunen, Robert W. Boyd, and Ksenia Dolgaleva. In Sec. S1, we present supporting material for Fig. 2d and Fig. 3b. In Sec. S2 we determine the type of SLR by looking directly at the polarizability and the lattice sum. Section S3 shows the dependence of the LSPR and SLR behaviours on the particle geometry, produced using FDTD simulations. It also contains additional measurement results for a different metasurface with the same lattice geometry. In Sec. S4, we present a representative image of a fabricated device. In Sec. S5, we describe our experimental setup.

S1 Q-factor extraction

Figure S1 shows Lorentzian fits to a series of LSA calculations with varying λ_{LSPR} (see Methods for values). The Q-factors extracted from these fits are used to produce the black curves in Fig. 2d. In Fig. S2, we reproduce the fits to the measurements that produced the values for Fig. 3b.

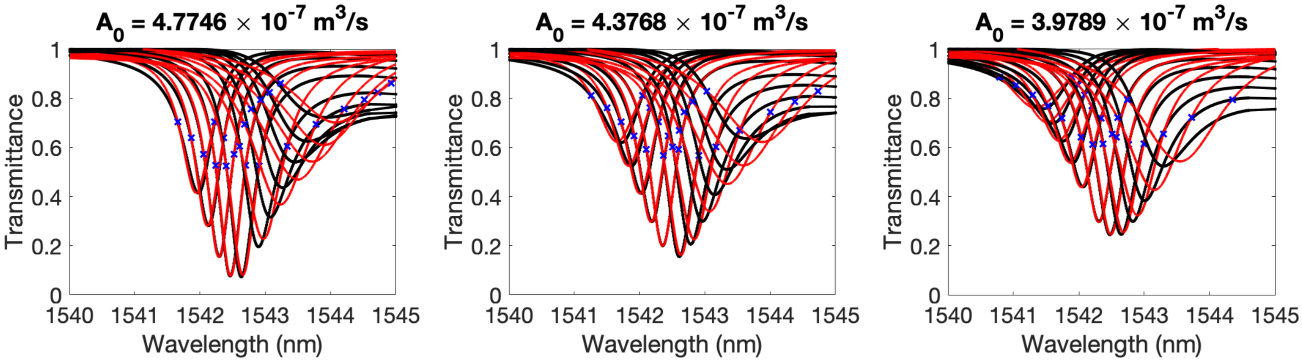

Fig. S1 | Parameter sweeps of LSA calculations. The black curves are calculated using the LSA using the values described in the Methods. The red curves correspond to Lorentzian fits.

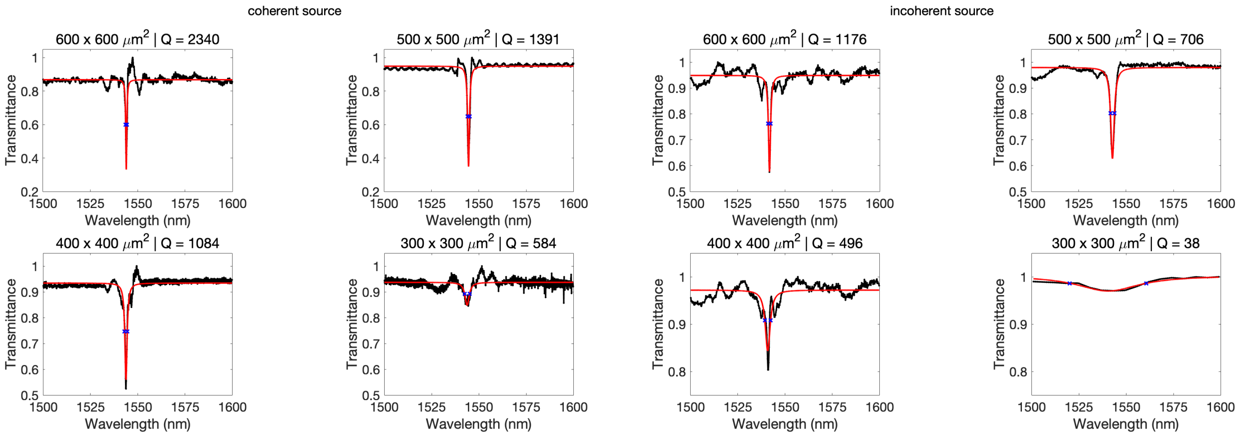

(a)

(b)

Fig. S2 | Measurements of devices. Measurements (black curves) of the devices described in the main text taken using **a,** a coherent and **b,** an incoherent source. The red lines correspond to Lorentzian fits. The array sizes and extracted Q-factors are indicated on the individual figures.

S2 SLR Type

Figure S3 shows the real part of the inverse of the particle polarizability $\mathrm{Re}[1/\alpha]$ as well as the real part of the lattice sum $\mathrm{Re}[\mathbb{S}]$ for the metasurface in Fig. 1. As these two values cross twice near λ_{SLR}, this SLR is considered to be an SLR of the first type according to the nomenclature of Ref.[1].

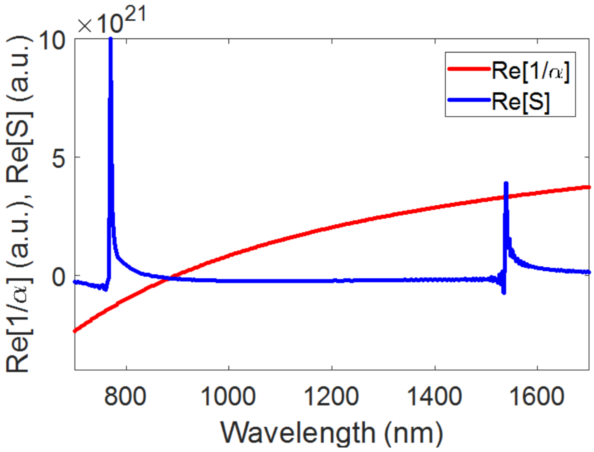

Fig. S3 | SLR type. The real part of the inverse of the particle polarizability $\mathrm{Re}[1/\alpha]$ as well as the real part of the lattice sum $\mathrm{Re}[\mathbb{S}]$ for the metasurface in Fig. 1.

S3 Dependence of SLR behaviour on particle dimensions

To explicitly demonstrate how changing the dimensions of the nanoparticle may affect the properties of the SLR, we perform full-wave simulations in FDTD using a series of particle geometries. Figure S5 depicts the simulation results. Not only the Q-factor, but also λ_{SLR} and the extinction ratio are all affected by changes in the particle dimensions.

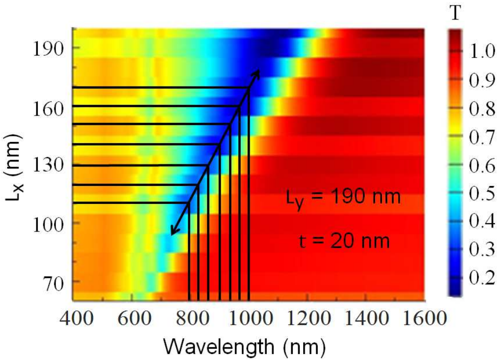

Fig. S4 | Particle dimension vs. LSPR wavelength. λ_{LSPR} (shown in x-axis) linearly increases alongside the particle length L_x towards the light polarization (shown in y-axis). This relation is extracted from full-wave simulations performed with FDTD.

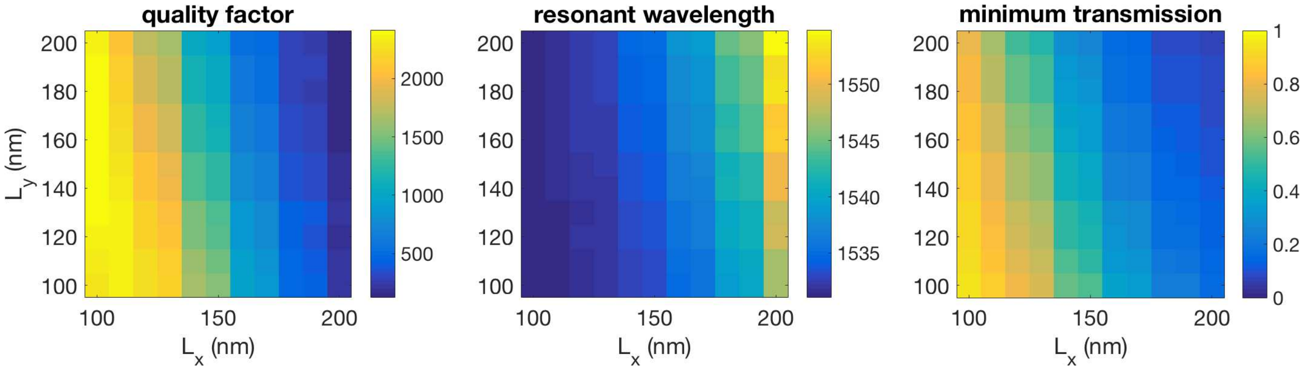

Fig. S5 | Particle dimension sweep. Quality factor Q (left), resonant wavelength λ_{SLR} (center), and minimum transmission as a function of particle dimensions L_x and L_y, extracted from full-wave simulations performed with FDTD.

In Fig. S6a, we present a different 400×400 µm^2 array with a nanoparticle geometry of $L_x = 200$ nm, $L_y = 130$ nm. Note that the nanoparticle dimensions are identical to those presented in the arrays above, but due to being rotated by 90 degrees, their resulting particle polarizabilities are completely different. The lattice constants are identical to the arrays presented in the main text, that is, $P_x = 500$ nm and $P_y = 1060$ nm.

The measurements in Fig. S6b were performed using an incoherent source. Here, due to the different polarizability, λ_{LSPR} is red-shifted (1100 nm vs 840 nm), and consequently, the SLR is dramatically affected: in comparison to the matching array in the main text which has an SLR of $Q = 500$, the SLR here only has a $Q = 80$, despite having the same lattice constants and nanoparticle geometries. This further demonstrates the importance of the polarizability to the Q of the SLR.

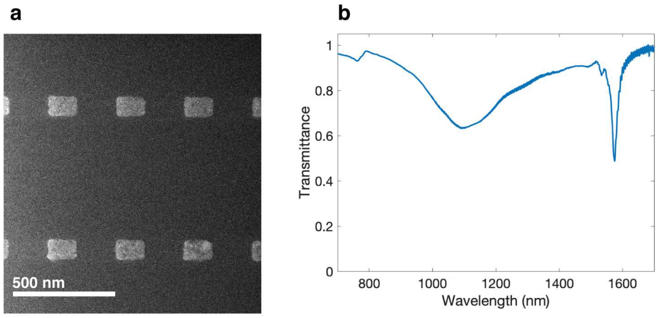

Fig. S6 | Metasurface with same lattice constants but rotated nanoparticles. This device consists of a 400×400 µm^2 array with $L_x = 200$ nm, $L_y = 130$ nm, $P_x = 500$ nm and $P_y = 1060$ nm. The SLR is also located at $\lambda_{\mathrm{SLR}} = 1550$ nm, but here $Q = 80$.

S4 Image of the device

Figure S7 shows a typical optical image for one of the devices taken with a bright field microscope. Surrounding the device are large aluminum alignment marks to help locate the device in the experimental setup.

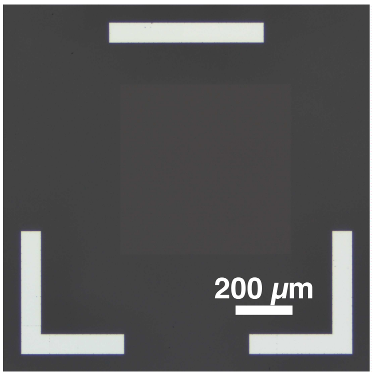

Fig. S7 | Large-area high-Q SLR device. Optical image of a 600 × 600 μm^2 array.

S5 Experimental setup

A broadband source is collimated and is polarized using a broadband linear polarizing filter. A first iris is optionally placed to help align the sample in the center of the beam. The beam is then passed through the sample. The surface of the device is imaged using an $f_2 = 35$ mm lens, and a pinhole is placed in the image plane to select the desired array. The transmitted light is collected in a large core (400 µm diameter) multimode fiber and is analyzed using an optical spectrum analyzer.

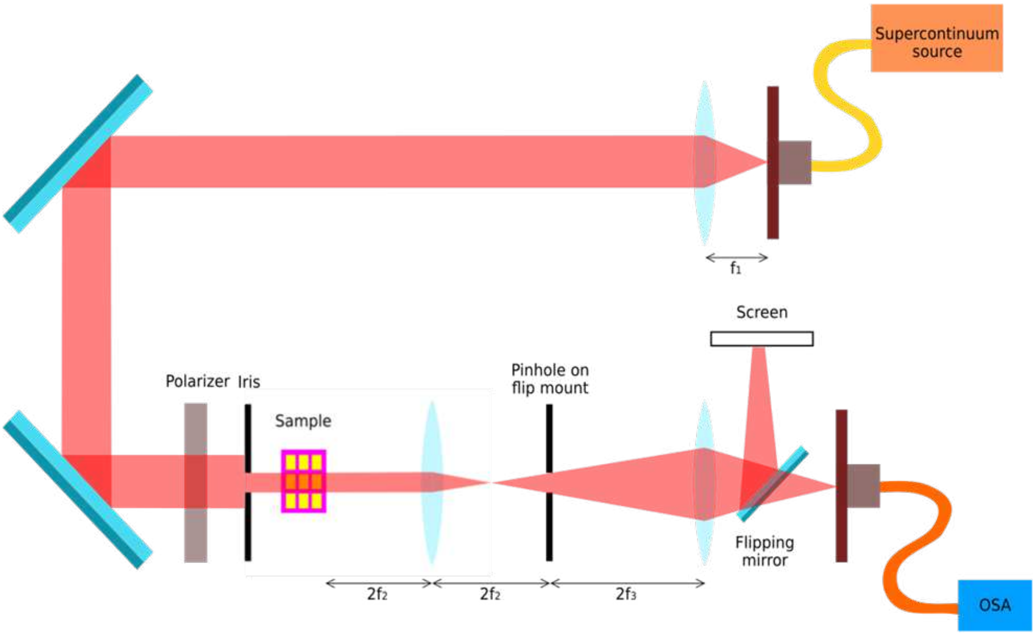

Fig. S8 | Experimental setup. The metasurface is excited by a broadband collimated and polarized beam. Light is collected from the image plane of the metasurface and detected using a camera or a spectrum analyser.

References for Supplementary Information

1. Kravets, V. G., Kabashin, A. V., Barnes, W. L. & Grigorenko, A. N. Plasmonic surface lattice resonances: A review of properties and applications. *Chemical Reviews* **118**, 5912–5951 (2018).

Chapter 4

Plasmonic Metasurface with Cross-Polarized Resonances

4.1 Summary

In this chapter, we experimentally demonstrate a metasurface comprising an array of 'V'-shaped plasmonic nanoparticles, which is capable of exciting two polarization-controlled surface-lattice resonances (SLRs) at two distinct wavelengths spectrally separated by an octave-band distance (one in the infrared and the other one in the visible spectral regimes). Here, one of the SLRs, that is excited in the infrared wavelength, possesses an ultra-high-Q feature with the Q-factor on the order of 10^3. The obtained results verified our group's prior theoretical modelling conducted by Dr. Mikko J. Huttunen and Dr. Orad Reshef. In addition, this work also inspired other research group to conduct nonlinear SHG experiments using similar metasurfaces by implementing the corresponding dual-SLRs at both the fundamental and SH wavelengths [73]–[75].

4.2 Contributions

The results presented in this chapter have been published in *Optics Letters* [76]. Together with Dr. Orad Reshef and Dr. Mikko J. Huttunen, I conceived the basic idea for this work. The idea was to prepare an SLR metasurface for highly efficient nonlinear second-harmonic generation in free-space flat optical regime. As a part of the collaboration, Dr. Mikko J. Huttunen and I jointly performed the FDTD simulations. Dr. Orad Reshef fabricated the device based on our design. Dr. Raja Naeem Ahmed, a PhD intern from Germany, initally assisted with carrying out the measurements using the experimental linear transmission measurement setup that I built for the previous project. Dr. Orad Reshef and I analyzed the experimental results. Lastly, Dr. Jeremy Upham, Dr. Mikko J. Huttunen, Prof. Robert W. Boyd, and Prof. Ksenia Dolgaleva supervised the research and the development of the manuscript. I wrote the first draft of the manuscript. All co-authors subsequently took part in the revision process and approved the final copy of the manuscript.

4.3 Article

The published article follows verbatim.

Letter Vol. 47, No. 8 / 15 April 2022 / Optics Letters 2105

Optics Letters

Cross-polarized surface lattice resonances in a rectangular lattice plasmonic metasurface

M. SAAD BIN-ALAM,[1,*] ORAD RESHEF,[2] RAJA NAEEM AHMAD,[2,3] JEREMY UPHAM,[2] MIKKO J. HUTTUNEN,[4] KSENIA DOLGALEVA,[1,2] AND ROBERT W. BOYD[1,2,5]

[1] School of Electrical Engineering and Computer Science, University of Ottawa, Ottawa ON K1N 6N5, Canada
[2] Department of Physics, University of Ottawa, Ottawa ON K1N 6N5, Canada
[3] Max Plank Institute of Quantum Optics, Hans Kopfermann Str 1, 85748, Garching bei Munich, Germany
[4] Laboratory of Photonics, Tampere University, Tampere FI-33014, Finland
[5] The Institute of Optics and Department of Physics and Astronomy, University of Rochester, Rochester, New York 14627, USA
*Corresponding author: msaad009@uottawa.ca

Received 17 November 2021; revised 28 March 2022; accepted 30 March 2022; posted 31 March 2022; published 14 April 2022

Multiresonant metasurfaces could enable many applications in filtering, sensing, and nonlinear optics. However, developing a metasurface with more than one high-quality-factor or high-Q resonance at designated resonant wavelengths is challenging. Here, we experimentally demonstrate a plasmonic metasurface exhibiting different, narrow surface lattice resonances by exploiting the polarization degree of freedom where different lattice modes propagate along different dimensions of the lattice. The surface consists of aluminum nanostructures in a rectangular periodic lattice. The resulting surface lattice resonances were measured around 640 nm and 1160 nm with Q factors of ~50 and ~800, respectively. The latter is a record-high plasmonic Q factor within the near-infrared type-II window. Such metasurfaces could benefit such applications as frequency conversion and all-optical switching.

https://doi.org/10.1364/OL.448813

Resonant metasurfaces promise to enable free-space photonic applications in nanoscale thin flat optical devices [1]. Thanks to their strong resonance enhancement characteristics, plasmonic lattice metasurfaces formed by metal nanostructures are considered to be strong candidates for such applications as sensing, spectroscopy, and lasing [2–4]. Among those applications, some specific processes may involve two or more frequencies, particularly nonlinear optical processes, such as harmonic generation, frequency up- and downconversion, cross-phase modulation or ultrafast all-optical switching [5]. Strongly resonant responses, like plasmonic resonances, could boost the efficiency of nonlinear optical processes without requiring any phase-matching between the input and output waves [6,7]. Thus, an implementation of multiresonant plasmonic metasurfaces could dramatically enhance the efficiency of applications involving nonlinear optical phenomena [8].

Under optical illumination, metal nanostructures naturally exhibit strongly localized surface plasmon resonances (LSPRs) [9]. However, a longstanding issue with metal nanostructures is that of their high absorptive and radiative losses, which result in the swift decay of excitations associated with the LSPRs. Whereas absorptive losses are inherent to metals, it is possible to suppress the radiative or scattering losses by engineering periodic arrays of metal nanostructures to support plasmonic surface lattice resonances (SLRs) with longer lifetimes [4,10]. Such SLRs originate from the collective coupling of every particle in a lattice and suppress the scattered losses associated with the individual particles. Thus, the resulting resonances can have significantly high quality factors (Q>2000 [11]), appearing at the wavelength near the diffraction edge of the lattice periodicity. Under normal illumination, the spectral position of the SLRs can be defined by the product of the periodicity, P, of the particles toward its radiating direction and the refractive index n of the particles' surrounding background medium ($\lambda_{\mathrm{SLR}} \approx nP$) [11,12].

As such, SLR modes are generated in the form of in-plane waves, oscillating orthogonally to the polarization direction of incident light. Hence, in a 2D plasmonic metasurface array with a rectangular lattice formation, it is possible to generate two different SLR modes along two separate orthogonal directions [13]. Such lattice modes, owing to orthogonally polarized incident waves, may be useful for linear applications, such as polarization-selective notch filters, or nonlinear optical processes, such as cross-phase modulation or two-beam coupling, which depend on more than one input field.

In this Letter, we report the observation of multiple LSPRs and SLRs at different wavelengths in the same metasurface. The resonant wavelengths of the SLRs can be selected through the careful choice of lattice geometry. The different resonances can be isolated by selecting a given linear polarization of the probing light or they can be excited simultaneously by employing diagonally polarized light.

To properly design a metasurface with multiple resonances in both the visible and infrared regime, here we consider the behavior of the constituent materials in the spectral range from 400 nm to 1300 nm. In noble plasmonic metals, like gold and silver, the interband transition occurs in the visible wavelength regime [14]. This transition causes such metals to absorb most of the visible light, and to lose their capability to support plasmon oscillations in the shorter ultraviolet wavelength regime. However, unlike noble metals, the interband transition in aluminum appears in the near-infrared (NIR) regime (around $\lambda = 850\,\mathrm{nm}$). Furthermore, because of the electronic band structure of the aluminum, the interband transition is quite narrow [15]. Hence, aluminum retains its metallicity at shorter wavelengths, compared with gold or silver. Subsequently, aluminum nanostructures can exhibit LSPRs and can thus efficiently scatter light in the visible or ultraviolet spectral ranges [16]. Inspired by this fact, aluminum nanostructures have been recently adopted to demonstrate SLRs in periodic metasurfaces with applications in SHG and nanolasing [3,12,13]. It was also revealed that aluminum possesses a comparatively larger nonlinear optical coefficient than gold or silver [17,18]. We therefore elect to have our metasurface composed of aluminum nanoparticles cladded in a transparent, fused silica substrate.

Typically, the collective SLRs are excited at the longer wavelength tails of the LSPRs corresponding to the individual nanostructures [4]. As we aim to excite polarization-dependent SLRs, here we fabricate periodic right-angled V-shaped aluminum nanostructures, since this particular shape is used to exhibit two polarization-dependent LSPRs at different wavelengths [6,19,20]. The fabricated dimensions are: length $L \approx 110$–$130\,\mathrm{nm}$; width $W \approx 70$–$80\,\mathrm{nm}$; and thickness $t \approx 30\,\mathrm{nm}$. The overall array size is $400 \times 400\,\mu\mathrm{m}^2$. This design was selected to serve as a proof of principle for this approach to a flexible multiresonant metasurface, exhibiting SLRs in the visible and NIR spectra with high Q factors. For conceptual clarity, we investigated a rectangular lattice, supporting two orthogonal SLRs, excited using either x- or y-polarized incident light at normal incidence to the surface. This design makes it straightforward to independently control the properties of the SLRs by adjusting the incident polarization and the tilting angles of the metasurface. For example, the center wavelengths of the SLR could be controlled by appropriately tilting the metasurface. However, we note that different particle geometries or oblique lattices might be beneficial for applications, such as nonlinear frequency conversion, where mode overlaps between several SLRs should be optimized.

Figures 1(a)–1(c) illustrate the designed metasurface in 2D. Here, we depict the LSPR by the glowing yellow ring encircling each V-shape nanostructure, the SLR mode for x-polarization in red vertically, and the SLR mode for y-polarization in green horizontally in Fig. 1(a) and 1(b), respectively. In Fig. 1(c), we show that both SLRs can be excited simultaneously using diagonally polarized illumination. A focused-ion beam micrograph of the fabricated array is depicted in Fig. 1(d). The periodic structured particles form a rectangular lattice in the xy plane (periodicity $P_x \approx 445\,\mathrm{nm}$ and $P_y \approx 790\,\mathrm{nm}$) inside a fused silica substrate (refractive index $n = 1.46$).

The sample fabrication and the experimental technique are similar to those of Ref. [11]. We fabricate metasurfaces using a standard metal lift-off process. On top of a fused silica substrate, we deposit a silica undercladding layer using sputtering. Next, we define the pattern of the nanostructure arrays using electron-beam lithography in a positive tone resist bilayer with the help of a commercial conductive polymer. To correct for the nanostructure corner rounding, we design the mask using shape-correction proximity error correction. After the development, we deposit an aluminum layer using thermal evaporation followed by the lift-off process. We deposit a 200 nm thick final protective silica cladding layer using sputtering to protect the aluminum nanoparticles from oxidization. To make sure that the environment surrounding the metasurface is completely homogeneous, we sputter the initial and final silica layers using the same tool under the same conditions. Before the characterization, we cover the surface of the device in index-matching oil and also coat the backside of the silica substrate with an antireflective coating to minimize substrate-related etalon fringes [21].

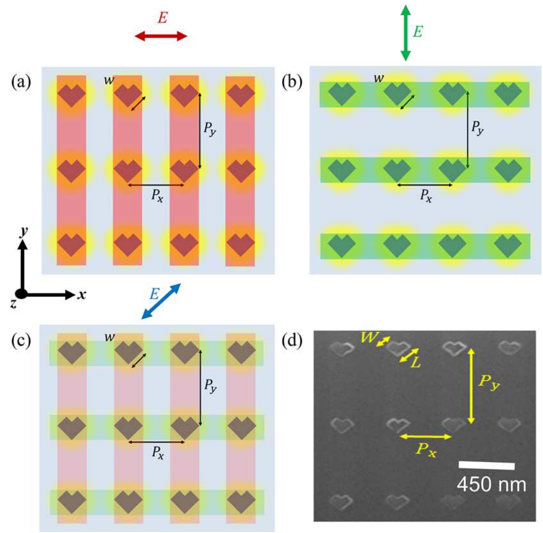

Fig. 1. Plasmonic metasurface in 2D. Normally incident light polarized (a) along the x-axis excites an SLR along the periodicity P_y (vertical, red), (b) along the y-axis excites an SLR along the periodicity P_x (horizontal, green), and (c) diagonally simultaneously excites SLRs along both directions. The yellow ring encircling each V-shaped nanostructure represents the LSPRs. (d) Focused-ion beam micrograph of fabricated metasurface.

In the experiment, we use a normally incident collimated light beam from a broadband supercontinuum laser source (spectral range $\lambda = 470$–$2400\,\mathrm{nm}$) to flood-illuminate all of the metasurface arrays in the sample. We control the incident polarization using a broadband linear polarizing filter. We observe the image of the light transmitted by the metasurface using a lens with a focal length $f = 35\,\mathrm{mm}$ and by placing a $100\,\mu\mathrm{m}$ pinhole in the image plane to collect the image of the desired array. We use a large-core ($400\,\mu\mathrm{m}$) multimode fiber to collect the transmitted light from the sample metasurface array and pass it to an optical spectrum analyzer (OSA). The resolution of the OSA is set to 0.01 nm. The OSA is used to measure the transmittance spectra by taking the ratio of light transmitted through the aluminum nanostructured metasurface array to light transmitted through the substrate without the metasurface array.

Figure 2(a) shows the simulated transmission spectra of our designed metasurface for different polarization states. The finite-difference time domain (FDTD) simulation was performed using Lumerical FDTD software. We also measured the normalized transmission spectra of our fabricated metasurface, illuminating it with a normally incident collimated beam generated from a broadband supercontinuum source. Figure 2(b) shows the measured normalized transmission spectra for different polarization states; these are in good agreement with the simulated results, shown in Fig. 2(a). For convenience, the resonances in the visible and infrared are presented separately in Figs. 2(c)–2(h) for different polarization states. It is evident in the enlarged spectra that, in the visible regime, the x-polarized

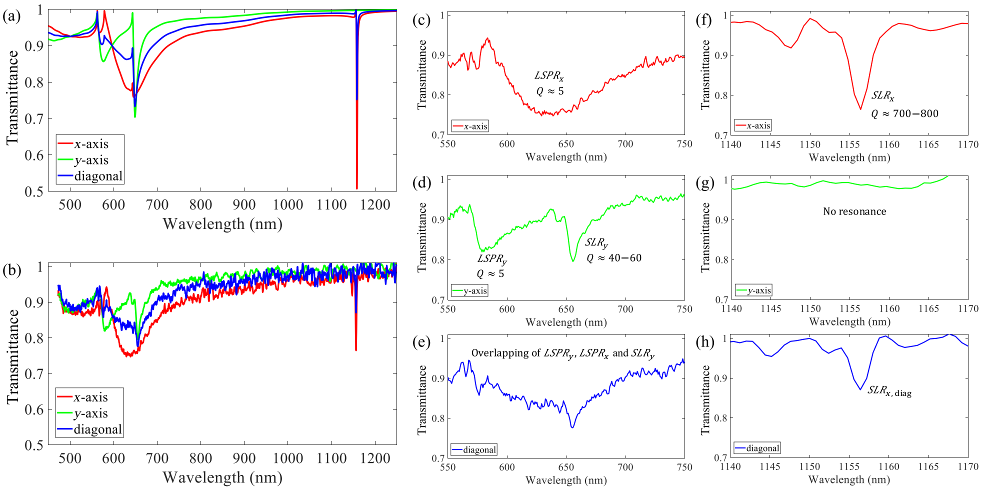

Fig. 2. (a) Simulated and (b) experimentally measured normalized transmission spectra of the polarization-dependent (*x*-axis, *y*-axis, and diagonal) multiresonant LSPRs and SLRs in the plasmonic metasurface. Diagonally polarized light excites the LSPRs and SLRs of both dimensions, enabling simultaneous SLRs around 649 nm and 1150 nm. (c)–(h) Close-ups of the measured spectra for the (c)–(e) visible and (f)–(h) NIR resonances for different polarizations.

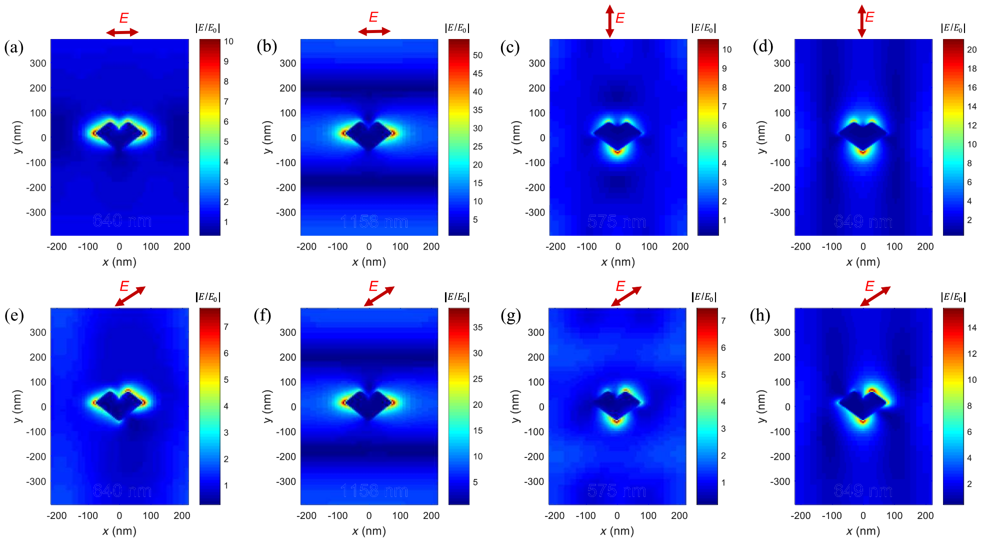

Fig. 3. Normalized electric field distributions of the SLR modes for the *x*-polarization at (a) 640 nm and (b) 1158 nm, *y*-polarization at (c) 575 nm and (d) 649 nm, and diagonal polarization at (e) 640 nm, (f) 1158 nm, (g) 575 nm, and (h) 649 nm.

LSPR [Fig. 2(c)] overlaps with the *y*-polarized LSPR and SLR [Fig. 2(d)] under diagonally polarized excitation [Fig. 2(e)]. We note that the resonance strength is halved from its original value, as conceptually predicted in Fig. 1(c) and simulated in Fig. 2(a). Such overlapping causes the resonances in the visible regime to superimpose with each other and thus form a modified spectral line shape, as depicted in Fig. 2(e). The Q factors of the LSPRs for both the x- and y-polarization are around 5, whereas the SLR Q factor for the y-polarization is around 50.

As expected, the SLR for the x-polarization in the infrared regime [shown in Fig. 2(f)] emerged at the far spectral distance, redshifted from all other resonance features in the visible regime. From different samples of our designed metasurface, we find the Q value for this infrared SLR to vary between 700 and 820. Although the high-Q SLR feature completely vanishes under y-polarized excitation [see Fig. 2(g)], it can emerge without any spectral modification for any other polarization states with reduced strength. Thus, as expected, we observe the re-appearance of the high-Q SLR in Fig. 2(h) for the diagonal polarization.

Next, we investigated the impact of the polarization state rotation on the in-plane electric field distribution inside the metasurface for all the resonances we discussed previously (Fig. 3). The simulated normalized electric field distribution corresponding to the LSPR around $\lambda = 629$ nm is presented in Fig. 3(a) and the SLR around 1158 nm is presented in Fig. 3(b) for the x-polarization. These figures show that the horizontally excited LSPR mode is only localized near the individual nanostructures; however, the delocalized SLR mode forms a delocalized diffraction grating-like standing wave, extended along the y-axis orthogonal to the polarization direction, which is in keeping with previous investigations of such lattice modes [12]. The electric field strength of the SLR is significantly higher than that of its

LSPR counterpart, as indicated by the color bars in Figs. 3(a) and 3(b), respectively. Such a large field enhancement in the SLR is the outcome of the scattering loss reduction by trapping the energy of scattered light near the diffraction order. The field distributions for these modes under y-polarized illumination are presented in Figs. 3(c) and 3(d). These modes are similar to their x-polarized counterparts, except that they are pointed along the y-direction, and feature smaller field enhancements, owing to a lower value of the associated Q factor.

We now turn to the electric field distribution under diagonal polarization. The fields in Fig. 3(e) depict the LSPR field under diagonally polarized light at 640 nm. Here, an SLR-like grating mode can be observed forming along the edges of the unit cell. This SLR-like feature around the LSPR center wavelength stems from the y-polarized SLR mode at 649 nm [Fig. 3(d)]. This indicates that, under diagonally polarized light, the x-polarized LSPR and the y-polarized SLR are superimposed. Comparing the scales between Fig. 3(a) and Fig. 3(e),we see that the overall field strength of the original LSPR for the x-polarization is slightly reduced in this superimposed mode by the off-axis diagonal polarization state.

In contrast, Fig. 3(f) shows no deviation of the stand-alone high-Q SLR field distribution around 1158 nm for the diagonal polarization from its x-polarization counterpart in Fig. 3(b), except the reduction of the field strength values indicated by the color bars. This feature confirms the behavior previously observed in Fig. 2(h), which depicts no spectral modification of the sharp infrared SLR in Fig. 2(f), owing to the lack of any other resonance nearby in Fig. 2(g). Next, we see that the LSPR field distribution for the y-polarization around 575 nm in Fig. 3(c) is also modified by the diagonally polarized light in Fig. 3(g). Such a modification occurs because of the superimposing of this LSPR for the y-polarization around 575 nm with the LSPR for the x-polarization around 640 nm. Contrary to the LSPR around 640 nm, this short wavelength modified LSPR around 575 nm is positioned relatively far from the SLR around 649 nm. Thus, the corresponding field distribution in Fig. 3(g) does not show a pronounced SLR-like grating.

Lastly, the field distribution in Fig. 3(h) depicts an SLR-like field distribution, just as in Fig. 3(d). These observations suggest that the field distribution of the localized, plasmon-like modes are dictated by polarization, whereas the SLR mode is dictated by the excitation wavelength.

In summary, we have experimentally demonstrated a technique to simultaneously excite cross-polarized dual LSPR and SLR modes in a nanostructured periodic metasurface via diagonally polarized normally incident light. The two different orthogonal SLRs, at wavelengths $\lambda = 649$ nm and $\lambda = 1158$ nm, could be tuned independently by modifying P_x and P_y, respectively. These two SLRs can be excited simultaneously using diagonally polarized light. We observed an unprecedentedly large Q factor for the SLR in the infrared type-II regime ($Q \approx 800$ around $\lambda = 1158$ nm) and analyzed the resonance characteristics and relevant electric field distribution of the generated modes. The Q factor of the SLRs in the visible region could probably be further enhanced by tuning dimensions and periodicity and enlarging the metasurface area [11,13]. In addition, because this approach to a multiresonant metasurface is independent of multiresonances demonstrated elsewhere [21], they could probably be combined to design particular mode coupling or even hybridized modes. This multiresonant high-Q metasurface is a proof of principle for efficient, polarization-selective filtering. Nonlinear optical processes in flat photonic devices, such as SHG to photon-pair generation via spontaneous parametric downconversion, may also be possible.

Acknowledgments. The authors thank Iridian Spectral Technologies Ltd, Ottawa, ON, Canada, for help in cladding the silica superstrate on top of the metasurface substrate for this work.

Disclosures. The authors declare no conflicts of interest.

Data availability. Data underlying the results presented in this paper are not publicly available at this time but may be obtained from the authors upon reasonable request.

REFERENCES

1. A. V. Kildishev, A. Boltasseva, and V. M. Shalaev, Science **339**, 1232009 (2013).
2. B. Špačková, P. Wrobel, M. Bocková, and J. Homola, Proc. IEEE **104**, 2380 (2016).
3. D. Wang, J. Guan, J. Hu, M. R. Bourgeois, and T. W. Odom, Acc. Chem. Res. **52**, 2997 (2019).
4. V. G. Kravets, A. V. Kabashin, W. L. Barnes, and A. N. Grigorenko, Chem. Rev. **118**, 5912 (2018).
5. R. W. Boyd, *Nonlinear Optics* (Academic, 2020).
6. M. Kauranen and A. V. Zayats, Nat. Photonics **6**, 737 (2012).
7. M. S. Bin-Alam, J. Baxter, K. M. Awan, A. Kiviniemi, Y. Mamchur, A. C. Lesina, K. L. Tsakmakidis, M. J. Huttunen, L. Ramunno, and K. Dolgaleva, Nano Lett. **21**, 51 (2021).
8. J. Butet, P.-F. Brevet, and O. J. F. Martin, ACS Nano **9**, 10545 (2015).
9. N. Meinzer, W. L. Barnes, and I. R. Hooper, Nat. Photonics **8**, 889 (2014).
10. C. Cherqui, M. R. Bourgeois, D. Wang, and G. C. Schatz, Acc. Chem. Res. **52**, 2548 (2019).
11. M. S. Bin-Alam, O. Reshef, Y. Mamchur, M. Z. Alam, G. Carlow, J. Upham, B. T. Sullivan, J.-M. Ménard, M. J. Huttunen, R. W. Boyd, and K. Dolgaleva, Nat. Commun. **12**, 974 (2021).
12. D. Khlopin, F. Laux, W. P. Wardley, J. Martin, G. A. Wurtz, J. Plain, N. Bonod, A. V. Zayats, W. Dickson, and D. Gérard, J. Opt. Soc. Am. B **34**, 691 (2017).
13. M. J. Huttunen, O. Reshef, T. Stolt, K. Dolgaleva, and R. W. Boyd, J. Opt. Soc. Am. B **36**, E30 (2019).
14. S. A. Maier, *Plasmonics: Fundamentals and applications* (Springer, 2007).
15. D. Gérard and S. K. Gray, J. Phys. D: Appl. Phys. **48**, 184001 (2015).
16. M. W. Knight, N. S. King, L. Liu, H. O. Everitt, P. Nordlander, and N. J. Halas, ACS Nano **8**, 834 (2014).
17. B. Metzger, L. Gui, J. Fuchs, D. Floess, M. Hentschel, and H. Giessen, Nano Lett. **15**, 3917 (2015).
18. M. Castro-Lopez, D. Brinks, R. Sapienza, and N. F. van Hulst, Nano Lett. **11**, 4674 (2011).
19. M. Celebrano, X. Wu, M. Baselli, S. Großmann, P. Biagioni, A. Locatelli, C De Angelis, G. Cerullo, R. Osellame, B. Hecht, L. Duò, F. Ciccacci, and M. Finazzi, Nat. Nanotechnol. **10**, 412 (2015).
20. R. Czaplicki, A. Kiviniemi, M. J. Huttunen, X. Zang, T. Stolt, I. Vartiainen, J. Butet, M. Kuittinen, O. J. F. Martin, and M. Kauranen, Nano Lett. **18**, 7709 (2018).
21. O. Reshef, M. Saad-Bin-Alam, M. J. Huttunen, G. Carlow, B. T. Sullivan, J.-M. Ménard, K. Dolgaleva, and R. W. Boyd, Nano Lett. **19**, 6429 (2019).

Chapter 5

Multiresonant Plasmonic Metasurfaces

5.1 Summary

In this chapter, we demonstrated a multiresonant metasurface that operates by trapping the out-of-plane scattering radiaion of a metallic nanoparticle array. Here we deposited a thin-film cladding layer with the refractive index matching the metasurface substrate, that had a thickness on the order of wavelength of light. That thin-film cladding layer acted as a waveguide thanks to its air-dielectric interface on one side, and the surfaces of the periodically arranged metallic particles on the other side. Thus, the cladding layer trapped the metasurface lattice-controlled out-of-plane collective scattering from the particles via total internal reflection, which ultimately resulted in the generation of multiple narrow-linewidth resonances with relatively high-Q factors compared to those of the broad localized surface plasmon resonances (LSPRs) associated with the individual metallic nanoparticles.

5.2 Contributions

The results demonstrated in this chapter have been published in *Nano Letters* [77]. The idea of this project was conceived by Dr. Orad Reshef and myself right after I understood the origin of the unexpected resonance features in the experiment. Based on my amended concept and design, Dr. Orad Reshef carried out the FDTD simulations, whereas Dr. Mikko J. Huttunen performed the lattice sum calculations. Dr. Orad Reshef and Dr. Graham Carlow then fabricated the devices. For the characterization, I used the same setup that I built for the previous projects and carried out the measurements. Dr. Orad Reshef analyzed the experimental results. At the end, Dr. Brian T. Sullivan, Prof. Jean-Michel Ménard, Prof. Ksenia Dolgaleva, and Prof. Robert W. Boyd supervised the research and the development of the manuscript. Dr. Orad Reshef wrote the first draft of the manuscript essentially based on my observations, and all authors subsequently took part in the revision process and approved the final copy of the manuscript.

5.3 Article

The published article follows verbatim.

NANO LETTERS
Letter
Cite This: *Nano Lett.* 2019, 19, 6429−6434
pubs.acs.org/NanoLett

Multiresonant High-*Q* Plasmonic Metasurfaces

Orad Reshef,[*,†] Md Saad-Bin-Alam,[‡] Mikko J. Huttunen,[§] Graham Carlow,[∥] Brian T. Sullivan,[∥] Jean-Michel Ménard,[†] Ksenia Dolgaleva,[†,‡] and Robert W. Boyd[†,‡,⊥]

[†]Department of Physics and [‡]School of Electrical Engineering and Computer Science, University of Ottawa, 25 Templeton Street, Ottawa, ON K1N 6N5, Canada

[§]Photonics Laboratory, Physics Unit, Tampere University, P.O. Box 692, FI-33014 Tampere, Finland

[∥]Iridian Spectral Technologies Inc., 2700 Swansea Crescent, Ottawa, ON K1G 6R8, Canada

[⊥]Institute of Optics and Department of Physics and Astronomy, University of Rochester, Rochester, New York 14627, United States

Supporting Information

ABSTRACT: Resonant metasurfaces are devices composed of nanostructured subwavelength scatterers that generate narrow optical resonances, enabling applications in filtering, nonlinear optics, and molecular fingerprinting. It is highly desirable for these applications to incorporate such devices with multiple high-quality-factor resonances; however, it can be challenging to obtain more than a pair of narrow resonances in a single plasmonic surface. Here, we demonstrate a multiresonant metasurface that operates by extending the functionality of surface lattice resonances, which are the collective responses of arrays of metallic nanoparticles. This device features a series of resonances with high-quality factors ($Q \sim 40$), an order of magnitude larger than what is typically achievable with plasmonic nanoparticles, as well as a narrow free spectral range. This design methodology can be used to better tailor the transmission spectrum of resonant metasurfaces and represents an important step toward the miniaturization of optical devices.

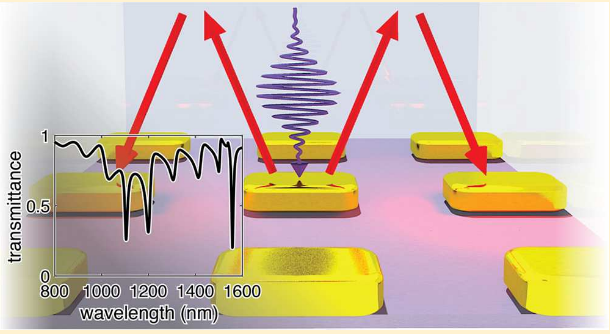

KEYWORDS: *Plasmonics, surface lattice resonance, resonant metasurface, gold nanoparticles, nanophotonics*

Plasmonic nanoparticles intrinsically support localized surface plasmon resonances (LSPRs) that may be spectrally located from the visible to the mid-infrared regime.[1,2] These resonances can easily be tailored by modifying the nanoparticle geometry, and this design flexibility has opened up the field of nanoplasmonics for applications in filtering,[3,4] color generation,[5−8] and, due to the large intrinsic nonlinearities of metals, nonlinear optics.[9−11] More recently, gold nanoparticles have been used as meta-atom building blocks in metamaterials and metasurfaces that exploit the tunability of LSPRs.[12−16]

Despite this versatility, applications that feature plasmonic particles are limited by the inherent absorption loss of metals, which results in low-quality factors ($Q \lesssim 10$) in the optical regime.[17,18] Recently, surface lattice resonances (SLRs) have emerged as an alternative method to obtain narrow-band resonances in plasmonic systems.[18−21] These resonances appear in surfaces consisting of periodic arrays of metal nanoparticles, and they feature Q factors that are typically much higher than their LSPR counterparts, experimentally achieving quality factors on the order of $Q > 100$,[22,23] with numerical predictions exceeding 2000.[24] These large quality factors are advantageous to many practical applications of plasmonic devices, particularly in nonlinear optics. Indeed, SLR metasurfaces have already been shown to enhance nonlinearities,[25−28] and they have been implemented in lasers[23,29,30] and nonlinear spectroscopy applications.[31]

Many applications have been shown to benefit strongly from the existence of multiple simultaneous resonances,[32] such as molecular fingerprinting,[33] fluorescence imaging,[34] heads-up display technologies,[5,35,36] or nonlinear applications, such as in frequency mixing[37−39] or frequency comb generation.[40,41] Multiple simultaneous resonances are usually enabled by the hybridization of LSPRs such as in nanoparticle dimers and trimers,[37,42] by using asymmetric particles,[34,36] or through the use of multiple different materials.[35] More recent developments include the hybridization of multiple surface lattice resonances by incorporating multiple particles within a single unit cell,[43] among many other approaches in coupling both localized and delocalized responses.[32] However, to date, high-Q SLR metasurface designs have only supported one or two simultaneous SLRs,[43,44] typically owing to the number of degrees of freedom in a two-dimensional plane.[44] Here, we

Received: June 28, 2019
Revised: August 10, 2019
Published: August 27, 2019

DOI: 10.1021/acs.nanolett.9b02638
Nano Lett. 2019, 19, 6429−6434

show that a metasurface consisting of a metallic nanoparticle array cladded by a thin transparent layer may exhibit multiple hybrid high-Q SLR cavity modes.

In a periodically arranged array of plasmonic meta-atoms (Figure 1a), individual LSPRs strongly couple to form a hybridized collective lattice mode. This mode corresponds to the first-order diffraction mode of the array, which consists of a pair of counter-propagating surface modes in the plane of the array (Figure 1b). The lattice response is often modeled using the coupled-dipole method or the lattice sum approach (LSA), which calculate the effective polarizability induced in a single particle of the array by taking into account the change in the local field felt by the particle due to the light rescattered from all other dipoles in the lattice.[19,20] The explicit form of this lattice sum therefore depends strongly on the specific arrangement of the dipoles and their respective coupling channels (see Methods). For light at normal incidence to the surface and polarized along the x axis, an orthogonal lattice periodicity, P_y, and a homogeneous background refractive index of n, the LSA predicts that the resonance frequency of this mode is to be found at about $\lambda \approx nP_y$. The Q factor and extinction ratio of this resonance depend on the polarizability (and, therefore, the dimensions) of the individual nanoparticles.[24] The SLR wavelength has also been shown to depend on the nanoparticle dimension.[20]

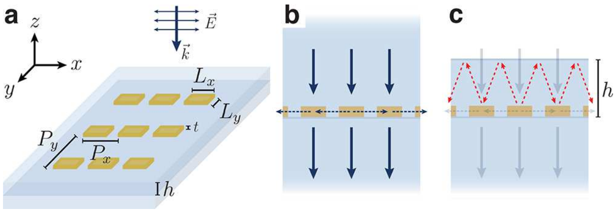

Figure 1. (a) Schematic of the metasurface under investigation, consisting of rectangular gold nanoparticles in a rectangular array and cladded by a thin silica cladding layer. (b) In a homogeneous medium, an incident plane wave (solid arrows) excites a surface lattice resonance. Here, every dipole is excited, scatters, and excites its neighbors (dashed blue arrows). (c) Thin cladding layer (h on the order of a few wavelengths) confines additional resonance modes, providing another coupling channel between the dipoles (dashed red arrows). For clarity, the illustrated dashed arrows in panels (b,c) indicate the light scattered from only the middle incident arrow.

An interesting situation arises when a wavelength-scale transparent film is deposited on top of the periodic lattice. Figure 2a compares the transmission spectra calculated using full-wave simulations for a metasurface composed of a rectangular array of gold nanoparticles in a homogeneous medium and a metasurface with a finite 2.5 μm thick silica (SiO_2) cladding. The particle dimensions are L_x = 200 nm by L_y = 130 nm, and the thickness of the gold layer is only t = 20 nm. The rectangular lattice parameters are P_y = (1550 nm)/n ≈ 1060 nm and P_x = 500 nm. In the usual situation with an infinitely thick cladding layer, we expect only the broad ($Q \approx$ 4) LSPR with a resonance wavelength at 1100 nm and the

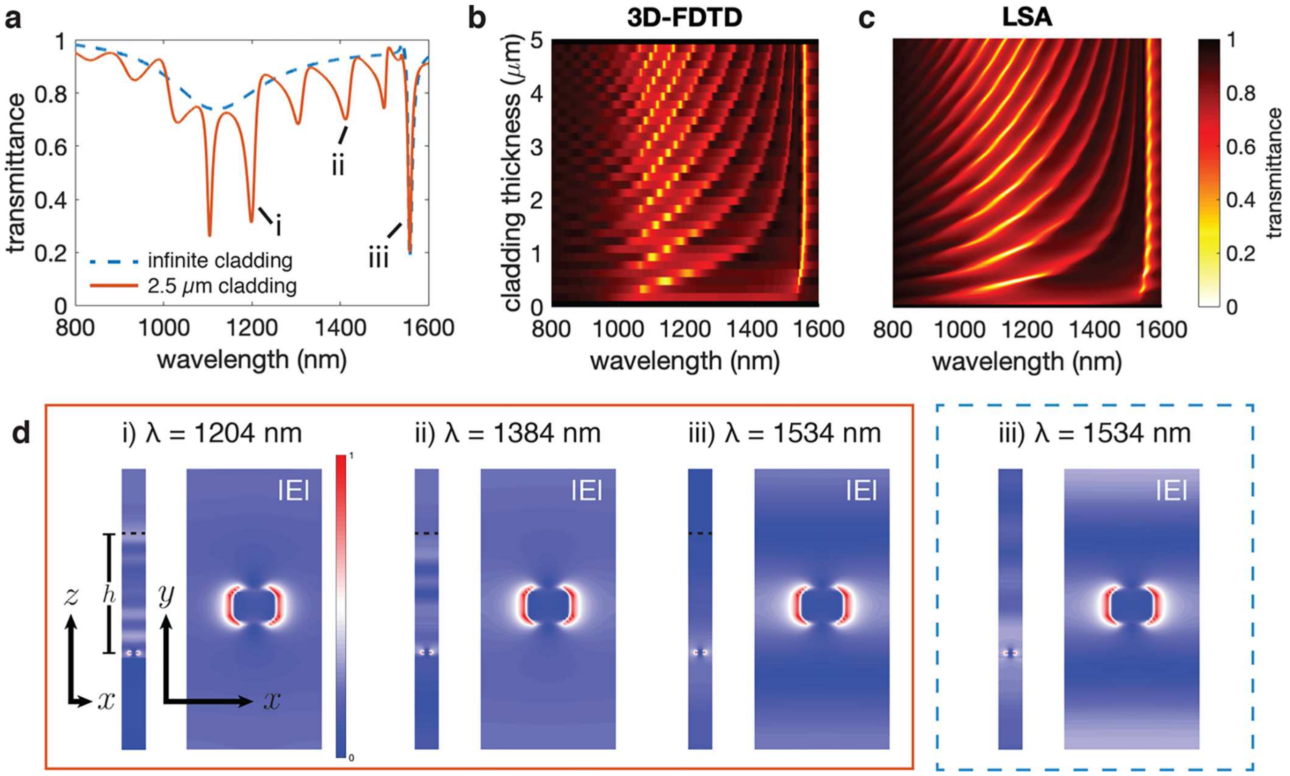

Figure 2. (a) Full-wave simulations of transmission spectra of a periodic lattice of gold nanoparticles in a homogeneous environment (dashed line) and with a cladding layer of finite thickness (solid line). (b) Transmission spectra as a function of cladding thickness calculated using 3D-FDTD. Additional resonances with higher-quality factors appear as the thickness of the cladding increases. (c) Corresponding transmission spectra calculated using the lattice sum approach. (d) Near-field profiles of resonances indicated in (a) for a 2.5 μm thick cladding layer (solid red box) and for an infinitely thick cladding layer (dashed blue box).

narrow ($Q \approx 150$) SLR at $\lambda = 1550$ nm to appear. However, when there is a finite cladding thickness, a plurality of hybrid resonance modes emerge. In particular, the SLR remains unchanged, and the hybrid resonances nearest to the nanoparticle's LSPR wavelength have both the highest Q factors and extinction ratios. The Q factor (as estimated from the full width at half-maximum) of the SLR remains at about 150, and the Q factor for the narrowest hybrid resonance is about 100.

To further investigate the origin of these new resonances, we perform additional numerical calculations (Figure 2b,c). First, we perform finite-difference time-domain (FDTD) simulations for various top-cladding thicknesses, h. Without any cladding (i.e., $h = 0$), the SLR mode is not supported, as expected.[18,20] As we gradually increase h, we also observe an increasing number of resonances in the transmission spectrum. Additionally, the most pronounced resonances continue to appear near the nanoparticle resonance, around $\lambda = 1100$ nm. Next, we perform the same calculations using the LSA. Here, the effect of a finite cladding layer can be taken into account by adding a coupling term between the dipoles due to reflection occurring at the superstrate−air interface (see Figure 1c). The LSA model presented in Figure 2c is in excellent agreement with the full-wave simulations, confirming that the origin of these additional modes may be attributed solely due to this coupling channel. Therefore, in addition to surface waves that travel parallel to the plane of the metasurface, the finite cladding layer supports modes that reflect diagonally between the metasurface and the upper cladding interface.

Figure 2d illustrates cross-sectional profiles of the magnitude of the electric field $|E|$ for a select few resonances. In all cases, the field is most intense on the surface of the nanoparticle. When looking out of the plane, we observe a notable amount of field also bound by the cladding layer away from the particle. Figure 2d also shows the field profile for the original SLR in a homogeneous background. It is found to be nearly identical to its corresponding resonance with a finite cladding layer. This behavior is expected because, in both cases, this resonant mode is propagating parallel to the plane of the surface, and it helps explain why its resonance wavelength does not change substantially as a function of cladding thickness.

To experimentally confirm these new hybrid resonances, we fabricate a series of arrays of this proposed device (i.e., P_x = 500 nm by P_y = 1060 nm) with a 2.5 μm thick silica top cladding and with lattice areas of 400 × 400, 500 × 500, and 600 × 600 μm^2. Figure 3 shows images of the metasurface before the final cladding deposition step. To isolate the effect of the lattice configuration from that of the nanoparticle dimensions, we also fabricated a matching set of devices with identical nanoparticles in the same orientation but in a rotated lattice configuration (i.e., P_x = 1060 nm by P_y = 500 nm). Finally, we also fabricated another different series of devices that support SLR at $\lambda = 1550$ nm (i.e., P_x = 400 nm by P_y = 1060 nm). In these devices, the particle number was held constant, resulting in total array sizes of 320 × 400, 400 × 500, and 480 × 600 μm^2.

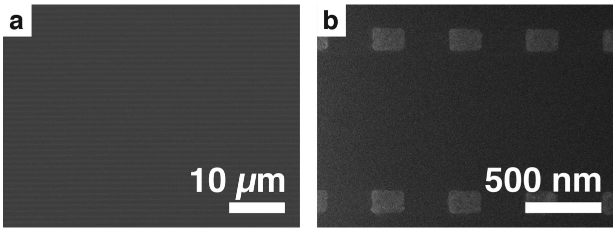

Figure 3. (a) Bright-field optical microscope image of the metasurface. (b) Helium ion microscope image of the metasurface prior to cladding deposition.

Figure 4 displays the transmittance through these devices as a function of wavelength. The resonances are present in all devices, in good agreement with the simulations. In devices where P_y = 1060 nm, the SLR appears around the design wavelength of $\lambda = 1550$ nm. The resonances with the highest extinction ratio appear near the LSPR, as predicted by the simulations. Notably, the sharpest hybrid resonance has a Q factor of 40, an order of magnitude larger than that of the individual nanoparticles. In every device, both the extinction ratios and the Q factors of the resonances increase as a function of array size. Finally, in the array with the rotated lattice configuration, the SLR does not appear at $\lambda = 1550$ nm, as expected (Figure 4b).

The plasmonic metasurface described above supports multiple resonances with Q factors that are an order of magnitude larger than those associated with the LSPRs of the individual nanoparticles. The resulting hybrid modes propagate along trajectories described by the LSA method and may be interpreted as higher-order diffraction modes that are confined by the upper boundary.[45] Full-wave simulations show that, despite their differing trajectories, the different resonances possess similar field profiles on the surface of the nanoparticle, with good spatial overlap. These types of multiresonant surfaces could be exploited for applications in optical frequency mixing, which would benefit from the combination of the strong nonlinearities of metals, strong field overlap, and the modification of the local density of states of high-quality resonances. The location and number of resonances is determined by the lattice spacing and the thickness of the top-cladding layer and can be rapidly predicted using the modified LSA. As the array size increases, the devices perform better, manifesting higher Q factors and deeper extinction ratios. We note that the simulation, which treats an "infinitely periodic" array, exhibits the narrowest and deepest resonances, suggesting that larger arrays could display even better performance, as has been explored in ref 46.

The effect of combining a Fabry-Pérot (FP) microcavity with plasmonic nanoparticles has already been thoroughly investigated in the literature.[47−50] Typically, lattice parameters are deeply subwavelength such that the metasurface may be treated as an effective reflective boundary in an asymmetric FP cavity. This modeling approach does not work in our case due to the emergence of diffraction orders. In a more recent implementation,[50] an SLR is hybridized with the propagating eigenmodes of a higher-index slab waveguide. In our approach, the cladding layer possesses the same refractive index as the substrate and would not support any propagating slab modes in the absence of the metasurface. Therefore, our method, which capitalizes on the periodic structure of the lattice to exploit the highest Q resonances, is based on a fundamentally novel resonance mechanism. Its functionality can also be further expanded by combining with other multiresonance mechanisms, such as by employing unit cells that contain more than a single nanoparticle.[43]

One interesting consequence of this resonance mechanism is that the free spectral range (FSR) of this device may turn out

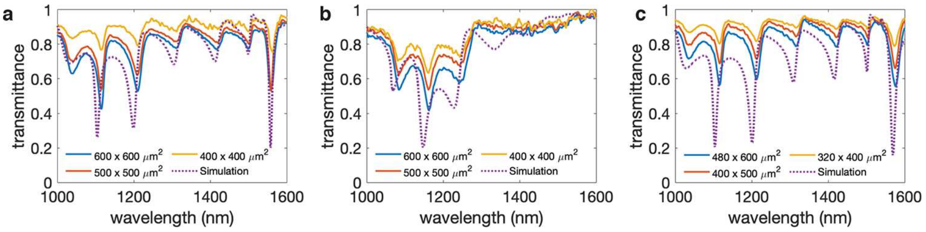

Figure 4. Transmission spectra for (a) $P_x = 500$ nm by $P_y = 1.06$ μm, (b) $P_x = 1.06$ μm by $P_y = 500$ nm, and (c) $P_x = 400$ nm by $P_y = 1.06$ μm. The dashed line corresponds to full-wave simulations with periodic boundary conditions. Multiple resonances emerge with quality factors that are significantly larger than those of the individual nanoparticles. No SLR is supported at $\lambda = 1550$ nm when $P_y \neq 1.06$ μm, as expected. The measurements are taken for arrays of different sizes—the extinction is observed to increase monotonically for larger arrays.

to be much narrower than that of an equivalent FP resonator. An FP etalon formed of 2.5 μm of silica glass is predicted to have an FSR of $\Delta\nu_{\mathrm{FSR}} = \frac{c}{2n_g L} = 42$ THz (corresponding to $\Delta\lambda_{\mathrm{FSR}} = 185$ nm near $\lambda = 1150$ nm). However, our devices all demonstrate a much narrower FSR of $\Delta\nu_{\mathrm{FSR}} = 22.8$ THz (i.e., $\Delta\lambda_{\mathrm{FSR}} = 94$ nm). This platform therefore provides a method with which one may relax the restrictions on device size for a given desired free spectral range.

If what is actually desired is to suppress this multiresonance mechanism, our work tells us that the cladding layer needs to be much thicker than what is typically used, for example, to enable high-quality photonic integrated circuits (e.g., ref 51). Indeed, the simulations in Figure 2 show that a wavelength-scale cladding layer is insufficiently thick to suppress the additional modes and that the presence of this layer needs to be taken into account for SLR metasurfaces with a finite cladding.

The approach presented above can be used to design the highest Q factor multiresonant metasurfaces that incorporate plasmonic materials, which is desirable for nonlinear applications. These devices feature a simple fabrication procedure, can be composed using common, non-exotic materials, and may be trivially scaled to other operating wavelengths of interest, particularly at longer wavelengths where dielectric stacks become prohibitively thick for standard deposition methods.

Methods. *Simulations.* Full-wave simulations were performed using a commercial 3D-FDTD solver. A single unit cell was simulated using periodic boundary conditions in the in-plane dimensions and perfectly matched layers in the out-of-plane dimension. The structures were created using fully dispersive optical material properties for silica[52] and for gold.[53] Minimal artificial absorption ($\mathrm{Im}(n) \sim 10^{-4}$) was added to the background medium to reduce numerical divergences.

The lattice sum approach is a simplified variant of the discrete-dipole approximation (DDA) method.[54] The version of the LSA code that was used to compute the figures in this paper can be found in ref 55. The LSA differs from the DDA in that it assumes an infinite array of identical dipoles ($\vec{p}_i = \vec{p}_k = \vec{p}$).[56] Under these assumptions, the dipole moment $\vec{p}$ of any particle in the array can be written as

$$\vec{p} = \frac{\epsilon_0 \alpha \vec{E}_{\mathrm{inc}}}{1 - \alpha \mathcal{S}} \equiv \epsilon_0 \alpha^* \vec{E}_{\mathrm{inc}} \qquad (1)$$

where the effect of interparticle coupling is incorporated in the lattice sum $\mathcal{S}$ and α^* is the effective polarizability. For arrays with in-plane coupling, the lattice sum term $\mathcal{S}_{\mathrm{in}}$ is simply

$$\mathcal{S}_{\mathrm{in}} = \sum_{j=1}^{N} \frac{\exp(ikr_j)}{r_j} \left[k^2 \sin^2\theta_j + \frac{(1 - ikr_j)(3\cos^2\theta_j - 1)}{r_j^2} \right] \qquad (2)$$

where the sum extends over the N nearest neighboring dipoles, r_j is the distance to the jth dipole, and θ_j is the angle between $\mathbf{r}_j$ and the dipole moment $\vec{p}$. The simulation in Figure 2 considers all $N = 680\,000$ particles found in the largest (i.e., 600×600 $\mu\mathrm{m}^2$) array.

For the situation where particles may also optically couple back into the array via scattered fields reflected at the superstrate−air interface, the total lattice sum term is modified by an additional contribution:

$$\mathcal{S} = \mathcal{S}_{\mathrm{in}} + \mathcal{S}_{\mathrm{FP}} \qquad (3)$$

The lattice sum term $\mathcal{S}_{\mathrm{FP}}$ for arrays with out-of-plane (Fabry-Pérot type) coupling takes the form

$$\mathcal{S}_{\mathrm{FP}} = \sum_{j=1}^{N} \frac{R_j \exp(ikd_j)}{d_j} \left[k^2 \sin^2\theta_j + \frac{(1 - ikd_j)(3\cos^2\theta_j - 1)}{d_j^2} \right] \qquad (4)$$

where h is the thickness of the upper cladding, $d_j = 2\sqrt{r_j^2/4 + h^2}$, and R_j are the appropriate Fresnel amplitude reflection coefficients. A similar approach to this structure can be found in refs 57 and 58. Once the particle polarizabilities are known, the optical extinction spectra can be obtained by solving for eqs 2−4 and using the optical theorem $\mathrm{Ext} \propto k\mathrm{Im}(\alpha^*)$.[59]

Fabrication. The metasurfaces are fabricated using a standard metal lift-off process and a positive tone resist bilayer. We start with a fused silica substrate and define the pattern using electron-beam lithography with the help of a commercial conductive polymer. The mask was designed using shape correction proximity error correction[60] to correct for corner rounding. Following development, gold is deposited using thermal evaporation. The final silica cladding layer is deposited using sputtering. The backside of the silica substrate is coated with an antireflective coating to minimize substrate-related etalon fringes.

Characterization. The samples are excited using a collimated tungsten−halogen light source. The incident polarization is controlled using a broad-band linear polarizing filter. The entire sample is illuminated, and the transmission from a single device is selected using a variable aperture. The transmission spectrum is measured using a diffraction-grating-based optical spectrum analyzer and is normalized to a background trace of the substrate without gold nanostructures.

■ ASSOCIATED CONTENT

Ⓢ Supporting Information

The Supporting Information is available free of charge on the ACS Publications website at DOI: 10.1021/acs.nanolett.9b02638.

Up-to-date LSA FP code (PDF)

■ AUTHOR INFORMATION

Corresponding Author

*E-mail: orad@reshef.ca.

ORCID

Orad Reshef: 0000-0001-9818-8491

Robert W. Boyd: 0000-0002-1234-2265

Author Contributions

O.R. and M.S.B.A. conceived the basic idea for this work. O.R. performed the FDTD simulations; M.J.H. performed the lattice sum calculations. O.R. and G.C. fabricated the devices. M.S.B.A. built the experimental setup and carried out the measurements. O.R. analyzed the experimental results. B.S., J.M.M., K.D., and R.W.B. supervised the research and the development of the manuscript. O.R. wrote the first draft of the manuscript, and all authors subsequently took part in the revision process and approved the final copy of the manuscript. Portions of this work were presented at the Conference on Lasers and Electro-Optics in 2019.[61]

Notes

The authors declare no competing financial interest.

■ ACKNOWLEDGMENTS

Fabrication in this work was performed in part at the Centre for Research in Photonics at the University of Ottawa (CRPuO). The authors thank Anthony Olivieri for help with nanofabrication, M. Zahirul Alam for help with measurements, Choloong Hahn for help with imaging, and Mikhail A. Kats and Martti Kauranen for helpful discussions. The authors acknowledge support from the Canada Excellence Research Chairs Program, the Canada Research Chairs Program, and the Natural Sciences and Engineering Research Council of Canada (NSERC) Discovery funding program. O.R. acknowledges the support of the Banting Postdoctoral Fellowship of the NSERC. M.S.B.A. acknowledges the support of the Ontario Graduate Scholarship and the University of Ottawa Excellence Scholarship. M.J.H. acknowledges the support of the Academy of Finland (Grant No. 308596) and the Flagship of Photonics Research and Innovation (PREIN) funded by the Academy of Finland (Grant No. 320165).

■ REFERENCES

(1) Oldenburg, S.; Averitt, R.; Westcott, S.; Halas, N. *Chem. Phys. Lett.* **1998**, *288*, 243−247.

(2) Maier, S. A. *Plasmonics: Fundamentals and Applications*; Springer: New York, 2007.

(3) Yokogawa, S.; Burgos, S. P.; Atwater, H. A. *Nano Lett.* **2012**, *12*, 4349−4354.

(4) Zeng, B.; Gao, Y.; Bartoli, F. *Sci. Rep.* **2013**, *3*, 2840.

(5) Hsu, C. W.; Zhen, B.; Qiu, W.; Shapira, O.; DeLacy, B. G.; Joannopoulos, J. D.; Soljačić, M. *Nat. Commun.* **2014**, *5*, 3152.

(6) Kumar, K.; Duan, H.; Hegde, R. S.; Koh, S. C.; Wei, J. N.; Yang, J. K. *Nat. Nanotechnol.* **2012**, *7*, 557−561.

(7) Kristensen, A.; Yang, J. K.; Bozhevolnyi, S. I.; Link, S.; Nordlander, P.; Halas, N. J.; Mortensen, N. A. *Nature Reviews Materials* **2017**, *2*, 16088.

(8) Guay, J. M.; Calà Lesina, A.; Côté, G.; Charron, M.; Poitras, D.; Ramunno, L.; Berini, P.; Weck, A. *Nat. Commun.* **2017**, *8*, 16095.

(9) Palomba, S.; Danckwerts, M.; Novotny, L. *J. Opt. A: Pure Appl. Opt.* **2009**, *11*, 114030.

(10) Li, G.; Zhang, S.; Zentgraf, T. *Nature Reviews Materials* **2017**, *2*, 17010.

(11) Alam, M. Z.; Schulz, S. A.; Upham, J.; De Leon, I.; Boyd, R. W. *Nat. Photonics* **2018**, *12*, 79−83.

(12) Schurig, D.; Mock, J. J.; Justice, B. J.; Cummer, S. A.; Pendry, J. B.; Starr, A. F.; Smith, D. R. *Science* **2006**, *314*, 977−980.

(13) Yu, N.; Genevet, P.; Kats, M. A.; Aieta, F.; Tetienne, J.-P.; Capasso, F.; Gaburro, Z. *Science* **2011**, *334*, 333−337.

(14) Sun, S.; Yang, K. Y.; Wang, C. M.; Juan, T. K.; Chen, W. T.; Liao, C. Y.; He, Q.; Xiao, S.; Kung, W. T.; Guo, G. Y.; Zhou, L.; Tsai, D. P. *Nano Lett.* **2012**, *12*, 6223−6229.

(15) Meinzer, N.; Barnes, W. L.; Hooper, I. R. *Nat. Photonics* **2014**, *8*, 889−898.

(16) Karimi, E.; Schulz, S. A.; De Leon, I.; Qassim, H.; Upham, J.; Boyd, R. W. *Light: Sci. Appl.* **2014**, *3*, No. e167.

(17) Doiron, B.; Mota, M.; Wells, M. P.; Bower, R.; Mihai, A.; Li, Y.; Cohen, L. F.; Alford, N. M.; Petrov, P. K.; Oulton, R. F.; Maier, S. A. *ACS Photonics* **2019**, *6*, 240−259.

(18) Kravets, V. G.; Kabashin, A. V.; Barnes, W. L.; Grigorenko, A. N. *Chem. Rev.* **2018**, *118*, 5912−5951.

(19) Zou, S.; Janel, N.; Schatz, G. C. *J. Chem. Phys.* **2004**, *120*, 10871−10875.

(20) Auguié, B.; Barnes, W. L. *Phys. Rev. Lett.* **2008**, *101*, 143902.

(21) Chu, Y.; Schonbrun, E.; Yang, T.; Crozier, K. B. *Appl. Phys. Lett.* **2008**, *93*, 181108.

(22) Li, S. Q.; Zhou, W.; Bruce Buchholz, D.; Ketterson, J. B.; Ocola, L. E.; Sakoda, K.; Chang, R. P. H. *Appl. Phys. Lett.* **2014**, *104*, 231101.

(23) Yang, A.; Hoang, T. B.; Dridi, M.; Deeb, C.; Mikkelsen, M. H.; Schatz, G. C.; Odom, T. W. *Nat. Commun.* **2015**, *6*, 6939.

(24) Zakomirnyi, V. I.; Rasskazov, I. L.; Gerasimov, V. S.; Ershov, A. E.; Polyutov, S. P.; Karpov, S. V. *Appl. Phys. Lett.* **2017**, *111*, 123107.

(25) Czaplicki, R.; Kiviniemi, A.; Laukkanen, J.; Lehtolahti, J.; Kuittinen, M.; Kauranen, M. *Opt. Lett.* **2016**, *41*, 2684−2687.

(26) Michaeli, L.; Keren-Zur, S.; Avayu, O.; Suchowski, H.; Ellenbogen, T. *Phys. Rev. Lett.* **2017**, *118*, 243904.

(27) Huttunen, M. J.; Rasekh, P.; Boyd, R. W.; Dolgaleva, K. *Phys. Rev. A: At., Mol., Opt. Phys.* **2018**, *97*, 053817.

(28) Huttunen, M. J.; Reshef, O.; Stolt, T.; Dolgaleva, K.; Boyd, R. W.; Kauranen, M. *J. Opt. Soc. Am. B* **2019**, *36*, E30−E35.

(29) Zhou, W.; Dridi, M.; Suh, J. Y.; Kim, C. H.; Co, D. T.; Wasielewski, M. R.; Schatz, G. C.; Odom, T. W. *Nat. Nanotechnol.* **2013**, *8*, 506−511.

(30) Hakala, T. K.; Rekola, H. T.; Väkeväinen, A. I.; Martikainen, J. P.; Nečada, M.; Moilanen, A. J.; Törmä, P. *Nat. Commun.* **2017**, *8*, 13687.

(31) Hooper, D. C.; Kuppe, C.; Wang, D.; Wang, W.; Guan, J.; Odom, T. W.; Valev, V. K. *Nano Lett.* **2019**, *19*, 165−172.

(32) Safiabadi Tali, S. A.; Zhou, W. *Nanophotonics* **2019**, *8*, 1199−1225.

(33) Choi, D.-Y.; Kivshar, Y. S.; Neshev, D. N.; Liu, M.; Altug, H.; Tittl, A.; Yesilkoy, F.; Leitis, A. *Science* **2018**, *360*, 1105−1109.

(34) Liu, X.; Yuan Lei, D. *Sci. Rep.* **2015**, *5*, 15235.

(35) http://www.mit.edu/~soljacic/transparent_display.html.

(36) Monti, A.; Toscano, A.; Bilotti, F. *J. Appl. Phys.* **2017**, *121*, 243106.

(37) Thyagarajan, K.; Rivier, S.; Lovera, A.; Martin, O. J. *Opt. Express* **2012**, *20*, 12860−12865.

(38) Aouani, H.; Navarro-Cia, M.; Rahmani, M.; Sidiropoulos, T. P.; Hong, M.; Oulton, R. F.; Maier, S. A. *Nano Lett.* **2012**, *12*, 4997−5002.

(39) Liu, S. D.; Leong, E. S. P.; Li, G. C.; Hou, Y.; Deng, J.; Teng, J. H.; Ong, H. C.; Lei, D. Y. *ACS Nano* **2016**, *10*, 1442−1453.

(40) Okawachi, Y.; Saha, K.; Levy, J. S.; Wen, Y. H.; Lipson, M.; Gaeta, A. L. *Opt. Lett.* **2011**, *36*, 3398−3400.

(41) Kippenberg, T. J.; Holzwarth, R.; Diddams, S. A. *Science* **2011**, *332*, 555−559.

(42) Nordlander, P.; Oubre, C.; Prodan, E.; Li, K.; Stockman, M. I. *Nano Lett.* **2004**, *4*, 899−903.

(43) Baur, S.; Sanders, S.; Manjavacas, A. *ACS Nano* **2018**, *12*, 1618−1629.

(44) Guo, R.; Hakala, T. K.; Törmä, P. *Phys. Rev. B: Condens. Matter Mater. Phys.* **2017**, *95*, 155423.

(45) Wang, S. S.; Magnusson, R. *Appl. Opt.* **1993**, *32*, 2606−2613.

(46) Zundel, L.; Manjavacas, A. *Journal of Physics: Photonics* **2019**, *1*, 015004.

(47) Schmidt, M. A.; Lei, D. Y.; Wondraczek, L.; Nazabal, V.; Maier, S. A. *Nat. Commun.* **2012**, *3*, 1108.

(48) Yao, Y.; Shankar, R.; Kats, M. A.; Song, Y.; Kong, J.; Loncar, M.; Capasso, F. *Nano Lett.* **2014**, *14*, 6526−6532.

(49) Li, P. C.; Yu, E. T. *J. Appl. Phys.* **2013**, *114*, 133104.

(50) Ramezani, M.; Lozano, G.; Verschuuren, M. A.; Gómez-Rivas, J. *Phys. Rev. B: Condens. Matter Mater. Phys.* **2016**, *94*, 125406.

(51) Ji, X.; Barbosa, F. A. S.; Roberts, S. P.; Dutt, A.; Cardenas, J.; Okawachi, Y.; Bryant, A.; Gaeta, A. L.; Lipson, M. *Optica* **2017**, *4*, 619−624.

(52) Palik, E. D. *Handbook of Optical Constants of Solids*; Academic Press: Orlando, FL, 1985.

(53) Johnson, P. B.; Christy, R. W. *Phys. Rev. B* **1972**, *6*, 4370−4379.

(54) Draine, B. T.; Flatau, P. J. *J. Opt. Soc. Am. A* **1994**, *11*, 1491−1499.

(55) https://zenodo.org/record/3259084#.XWbAvihKiUk10.5281/zenodo.3259084.

(56) Huttunen, M. J.; Dolgaleva, K.; Torma, P.; Boyd, R. W. *Opt. Express* **2016**, *24*, 28279−28289.

(57) Schokker, A. H.; Van Riggelen, F.; Hadad, Y.; Alù, A.; Koenderink, A. F. *Phys. Rev. B: Condens. Matter Mater. Phys.* **2017**, *95*, 085409.

(58) Chen, Y.; Zhang, Y.; Femius Koenderink, A. *Opt. Express* **2017**, *25*, 21358−21378.

(59) Jackson, J. D. *Classical Electrodynamics*, 3rd ed.; John Wiley & Sons, Inc.: Hoboken, NJ, 1999.

(60) Schulz, S. A.; Upham, J.; Bouchard, F.; De Leon, I.; Karimi, E.; Boyd, R. W. *Opt. Mater. Express* **2015**, *5*, 2798−2803.

(61) Saad-Bin-Alam, M.; Reshef, O.; Huttunen, M. J.; Carlow, G.; Sullivan, B.; Ménard, J.-M.; Dolgaleva, K.; Boyd, R. W. *High-Q Resonance Train in a Plasmonic Metasurface*; Conference on Lasers and Electro-Optics, Washington, DC, 2019; FM3C.4.

Chapter 6

Plasmonic Metasurfaces as 2D Lattice Diffraction Gratings

In the previous chapters, we focused on the in-plane surface lattice resonances (SLRs). Such lattice-coupled resonances could be useful for enhancing the efficiency of some selected optical processes which might be required to understand the fundamental optical phenomena in the laboratory environment. The notable examples of those selected optical phenomena are the flat nanolasing [78], nonlinear frequency conversion, and mixing [73], [79], *etc*. Notwithstanding, to extract the full benefit of the metasurface lattice-mode resonances, we need to explore alternative techniques to excite metasurface lattice-controlled high-Q resonances in different materials alongside new applications.

In this chapter, we describe two recently initiated projects associated with two distinct applications. In the first project, we are working on exciting non-localized high-Q resonances in a dielectric optical medium by implementing a 2D plasmonic nanoparticle array as a lattice diffraction grating. In this system, unlike the in-plane SLRs, we do not need to embed the nanoparticle array in a homogeneous medium, we can keep the nanoparticles uncovered from the top. The initial results were presented in the 2022 Conference on Lasers and Electro-Optics (CLEO) [80].

In the second project, we are implementing a 2D plasmonic lattice diffraction grating to enhance the light absorption in a semiconductor absorbing medium in a spectral region where that medium typically cannot absorb light naturally.

6.1 High-Q Guided-Mode Multi-Resonances

As mentioned in the previous chapters, the SLR-based metasurfaces need to be fully surrounded by a homogeneous dielectric medium in order for the SLR to be excited. Unfortunately, such homogeneous metasurfaces cannot be used in applications like biosensing, which require physical contact with the nanoparticle arrays.

Recently, apart from our SLRs-based work [72], [77], various types of high-Q metasurfaces have been demonstrated by exploiting Fano resonance-like quasi-bound-states in the continuum (quasi-BIC) [38] and guided-mode resonances (GMRs) [41], which often exhibit the Q-factors on the order of 10^3 to 10^4 [81], [82]. It is now believed that BIC- and GMR-based metasurfaces represent the superior suitability for practical applications. However, such metasurfaces have their own drawbacks that make them not ideal for applications. For example, BIC metasurfaces require breaking the symmetry of the nanoparticle's geometry or the array periodicity to excite non-radiative dark-mode resonances, which introduces additional complexity to the fabrication process. On the other hand, regarding the applications, a common downside of both SLRs- and BICs-based metasurfaces are the hurdles in simultaneously exciting multiple sharp resonances over a broad spectral range. Such high-Q multi-resonant features could benefit the applications involving nonlinear optical frequency conversion and mixing, and non-degenerate photon-pair generation.

To address these issues, we design a metasurface with multi-high-Q guided-mode resonances (GMRs) comprising a two-dimensional (2D) nanoparticle array integrated on a $LiNbO_3$ thin film. The $LiNbO_3$ thin film, which should act here like a slab waveguide, is sandwiched between the relatively low-index media, *e.g.*, air ($n_{\text{air}} \approx 1.0003$) and fused silica ($SiO_2$) glass, as illustrated in Fig. 6.1(a). Here, the thickness of the $LiNbO_3$ thin film is d. As depicted in Fig. 6.1(a), we choose a square lattice array by setting a common periodicity, $P_{\text{y}} = P_{\text{x}} = P$ in both y- and x-directions, respectively. Since the light scatters in all directions, we should also take into consideration the periodicity in the diagonal direction, which we can define as $P_{\text{xy}} = \sqrt{{P_{\text{y}}}^2 + {P_{\text{x}}}^2}$ (not shown in the figure). Considering that the polarization of incident light is aligned along the x-axis, we decided to use rectangular bar-shaped gold nanoparticles to construct the 2D diffraction grating array. By selecting such a shape with the shorter rectangle dimension aligned along the light polarization, we want to push the absorption loss-related localized surface plasmon resonances (LSPRs) corresponding to the individual gold nanoparticles towards the visible range, which should be spectrally far from any nonlocalized sharp resonances lying in the infrared and near-infrared ranges. Nevertheless, since such blue-shifting of the LSPRs also reduces the scattering cross-section, we want to keep the vertical length of the bars relatively large to compensate for this reduction.

The simulations are performed using Lumerical FDTD software. In Lumerical FDTD, at first we select a lossy fused silica glass medium as a substrate (refractive index, $n_{\text{glass}} \approx 1.46$). We introduce loss by artificially adding imaginary index representing the absorption inside the glass. Next, we add a thin layer of $LiNbO_3$ with thickness, d on top of the glass substrate. In practice, $LiNbO_3$ is an uniaxial birefringent material. In case of a x-cut $LiNbO_3$ thin film, the refractive index parallel to the any direction of the thin-film plane is uniform, which is called ordinary refractive index,

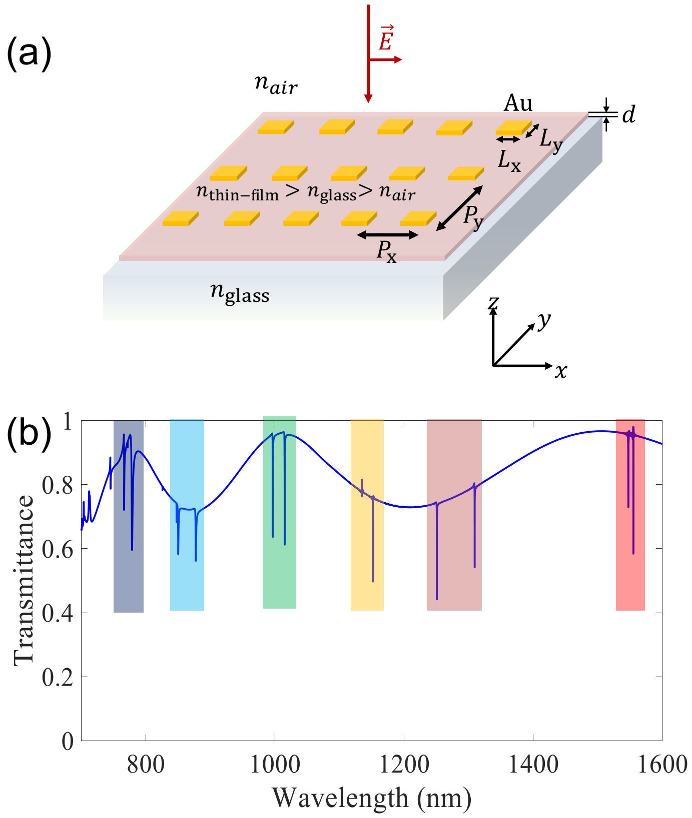

FIGURE 6.1: (a) Illustration of a metasurface comprising a nanoparticle array-integrated lithium niobate thin film. Here, collimated light is incident from the normal direction on the 2D nanoparticle array. (b) The simulated transmittance spectra of the metasurface showing an octave-spanned high-Q multi-resonances.

$n_\mathrm{o} \approx 2.21$ around the 1550 nm spectral wavelength. On the other hand, the refractive index towards the direction perpendicular to the thin-film plane is called extraordinary refractive index, $n_\mathrm{e} \approx 2.14$ around the 1550 nm spectral wavelength. Since in our case, we want both the x- and y-polarized scattered light from the nanoparticles to excite both transverse electric (TE) and transverse magnetic (TM) GMRs inside the thin-film, here we choose a x-cut $\mathrm{LiNbO_3}$ layer on top of the glass to ensure that, the refractive index of the thin film n_thinfilm is equal to $n_\mathrm{o} \approx 2.21$. Finally, on top of the $\mathrm{LiNbO_3}$ thin film, we put a 2D metasurface array consisting of gold nanoparticles which serve as a 2D diffraction grating array by scattering light inside the thin film.

To excite fundamental TE and TM mode resonances around 1550 nm, through the trial-and-error simulations, we find that the periodicity $P_\mathrm{y} = P$ and $P = P_\mathrm{x} = P$ should be aproximately equal to 780 nm. Here we set the rectangular-shaped nanoparticle bars' lengths to $l_x = 70$ nm and $l_y = 300$ nm, respectively. We also find that shortening the horizontal length l_x helps to increase the sharpness, *i.e.*, the resonance Q-factors. On the other hand, increasing the vertical length l_y helps to increase the resonance dip in transmittance spectra, *i.e.*, the resonance strength. Apart from the lengths, we also fix the height of the bar at $l_z = 20$ nm in our simulation, which falls within the range of a typical metal nanoparticle height (20 nm to 50 nm) suitable for the sample fabrication.

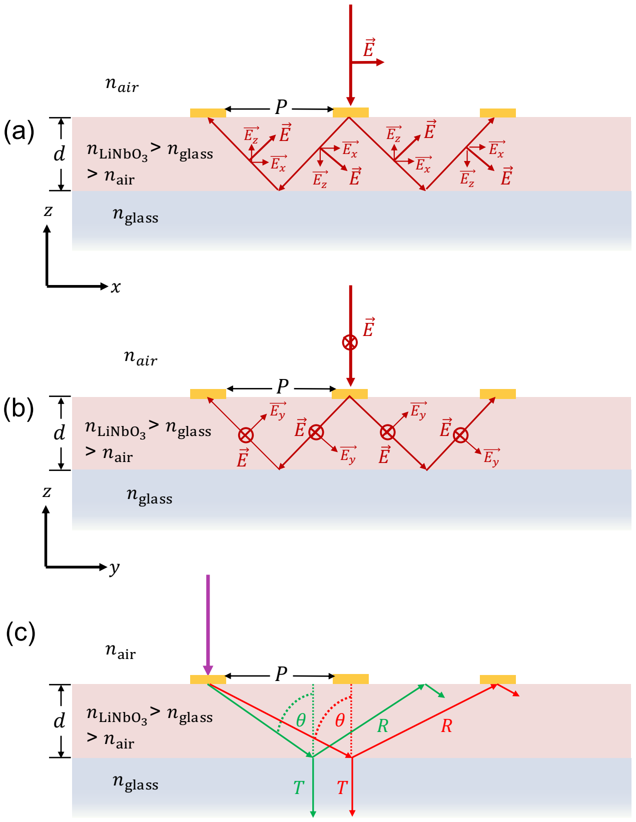

FIGURE 6.2: Cross-sectional views of the (a) xz and (b) yz planes of the metasurface showing the p- and s-polarized light diffracted/scattered by the 2D nanoparticle grating array with the periodicity P. The light forms the guided TE and TM modes inside the $\mathrm{LiNbO_3}$ thin film with thickness d. (c) Side-view of the metasurface representing either xz cross-section, yz cross-section or the diagonal cross-section across the xy plane illustrates that a normally incident collimated light can be scattered by the periodically arranged individual nanoparticles at different scattering angles. The scattered light experience total internal reflection inside the thin film, and thus creates multiple guided-mode resonances (GMRs).

Fig. 6.1(b) demonstrates the simulated octave-spanning transmittance spectra (800 nm to 1600 nm) corresponding to the $\mathrm{LiNbO_3}$ thin film integrated with the square lattice arrays. Here, two extremely sharp resonances appear near our desired fundamental wavelength around 1550 nm with the linewidth less than 0.5 nm; henceforth, the corresponding Q-factors are on the orders of 10^3. The origin of the two resonances around 1550 nm correspond to the TE and TM polarized GMRs inside the thin film, as illustrated in Fig. 6.2(a) and Fig. 6.2(b), respectively. Apart from the fundamental resonances, there are more pairs of the sharp resonances appearing at different shorter wavelengths throughout the 800 nm to 1600 nm octave-spanning broadband spectral range, which are indicated in different colors. Those resonances are also the GMR modes, which correspond to the TE- and TM-polarized scattered light inside the thin film, scattered by the nanoparticle array in-phase at different scattering angles in x, y and xy directions, as illustrated in Fig. 6.2(c).

6.2 Extended Short-Wavelength Light Absorption in InGaAs/InP Semiconductors

Short-wavelength infrared (SWIR) light enables the detection and imaging of objects of interest that would not be possible in the visible spectral regime. In the SWIR regime, photons are transmitted through certain visibly obscure media formed by the particles limited by Mie scattering or the molecular vibrations, such as water vapor, fog, cloud, and smog, alongside the media absorbing the visible light, such as silicon. Thus, the SWIR light can be used for detecting and imaging the objects emitting, reflecting, or absorbing the SWIR photons hidden behind visibly obscure media with high-resolution imaging contrast [62]. Such a technique finds its implementation in a variety of applications, for example, imaging of ambient stars and the background radiance (nightglow) through the cloud, security surveillance, imaging of the biological tissues through which longer wavelengths penetrate deeper than shorter wavelengths, product inspection and process quality control, and many more [61].

A handful of semiconductor materials, *e.g.*, germanium (Ge), indium arsenide (InAs), indium gallium arsenide (InGaAs), indium antimonide (InSb), and mercury cadmium telluride (MCT or HgCdTe) can be implemented in SWIR photodetection [1], [83]. Nevertheless, only lattice-matched InGaAs/InP III-V semiconductor-based photodetectors operating in the 900 nm to 1700 nm wavelength range are capable of performing practical photodetection via efficient conversion of the absorbed photons into photoelectrons due to their high quantum efficiency (Q.E.) and low dark current at room temperature [61]. High Q.E. (henceforth the device responsivity) requires a micron-scale-thickness (*e.g.*, 3–5 μm) InGaAs absorber. However, such a large thickness also increases the rise time (*i.e.*, the time taken by the generated electrons and holes to reach the ohmic contacts of the photodetector circuit), resulting in limiting the device speed, *i.e.*, the bandwidth of the photodetector [59], [84]. An InGaAs absorber with a thickness less than 1 μm can be operated at a relatively high speed but at the expense of relatively low sensitivity. Nevertheless, inserting such a nanometer-thick absorbing layer into a Fabry-Pérot microcavity (in which one mirror is formed by using the Bragg-reflector semiconductor bi-layer stack) can constitute a high-speed and high-sensitivity photodetector [59], [85]. As the alternatives to the relatively thick Fabry-Pérot microcavity, other types of flat resonators, such as metasurfaces, can also boost the efficiency of high-speed photodetectors [86], [87].

Such SWIR photodetectors operating at the telecom wavelengths play essential roles in the long-range light detection and ranging (LiDAR) systems, a recently developed technology mass-adopted in a variety of applications [51]. Unfortunately, the use of intense lasers for longer wavelengths and higher-resolution detection typically imposes eye safety issues, particularly in highly populated urban areas. Thus, nowadays, the operational spectral range of interest of the LiDAR system is shifting towards the extended SWIR band beyond the wavelength of 1700 nm, up to 2200 nm [83]. However, since the corresponding extended SWIR photon energy cannot exceed the bandgap energy of the InGaAs lattice matched to InP, one may increase In concentration of InGaAs to shorten its bandgap energy to absorb the extended SWIR photons. Notwithstanding, it causes the lattice mismatch between Indium-enriched InGaAs and InP on which InGaAs is grown. It creates severe threading dislocation inside the molecular structure of InGaAs/InP layers resulting in high dark-current noise in the photodetector circuit, henceforth triggering a significant drop in the signal-to-noise ratio. Introducing quantum-dots (QDs) inside the lattice-matched InGaAs absorber could extend the absorption wavelength to 1800–2200 nm extended short-wavelength infrared (SWIR) regime to provide an alternative solution that can help one to eliminate the problem of high dark current associated with the lattice-mismatched InGaAs/InP photodetector structure. The absorption in the QDs depends primarily on the number of QD layers; however, the QD thickness is limited to maintaining high crystal quality in the bulk-absorber structure. Such a trade-off greatly restricts the absorption efficiency of the QDs.

To counter such material property-limited restrictions in the extended SWIR regime, we seek solutions from the flat resonators-based technique of improving the efficiency of high-speed photodetectors operating in the traditional telecom SWIR regime. Here, using the concept of the metasurface lattice-enabled guided modes, we show that photodetectors consisting of 2D Bragg-diffraction-grating metasurfaces can significantly enhance the absorption inside the nanoscale-thin InGaAs QD absorber layer from 0.4% to approximately 23% of the incident light around the 1900-nm extended SWIR band. Such a large enhancement of light absorption could enable the realization of highly efficient InGaAs photodetectors for imaging spectroscopy, hyper-spectral imaging, and scientific imaging in the extended SWIR regime.

Recently, our collaborators from the National Research Council, Canada have experimentally observed a small amount of light absorption around 1900 nm after inserting multiple layers of 2-nm-thick InGaAs QDs inside the regular lattice-matched InGaAs layer. In Fig. 6.3(a), we illustrate such a structure comprising the QD layer without any distributed Bragg reflector (DBR) and metasurface. Here we consider

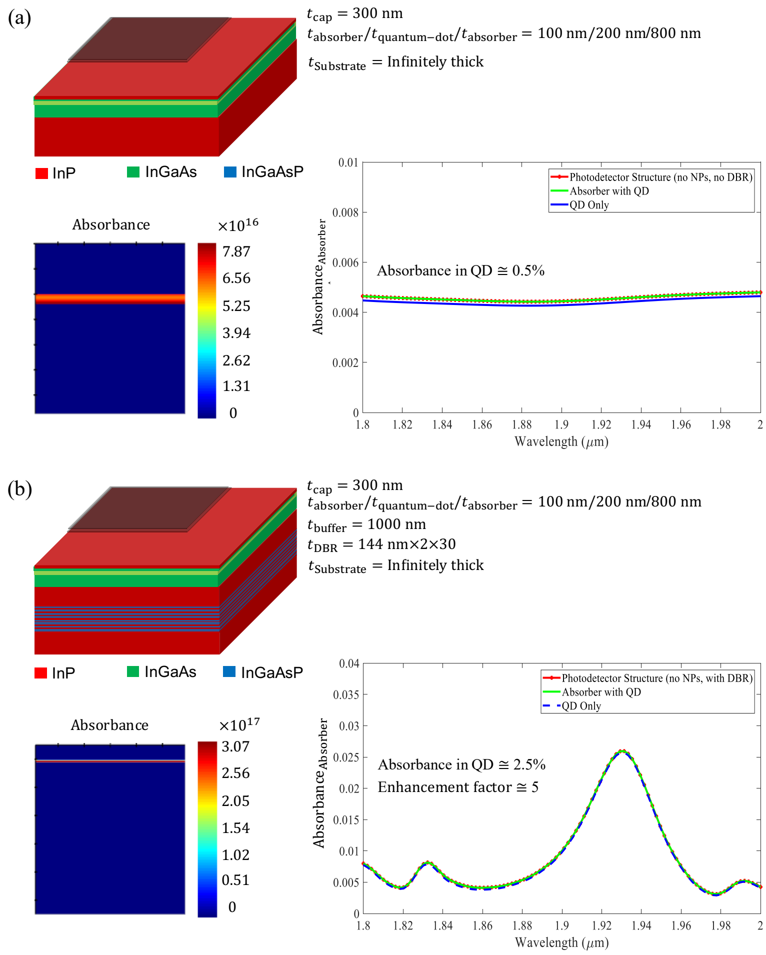

FIGURE 6.3: (a) A basic structure of a quantum-dot (QD) InGaAs/InP photodetector system comprising the InP cap layer cladded by an anti-reflection coating (ARC), InGaAs absorber layer loaded with the QD and the InP substrate. (b) A multi-stack distributed Bragg reflector (DBR) is added to the structure depicted in (a). The QD absorbance intensity map and the spectra in the extended SWIR regime are shown side-by-side with the corresponding structures.

only one thin QD layer with the thickness $t_{\text{quantum-dot}} = 200$ nm in our simulation instead of 100 ultra-thin layers of the actual QDs with a 2-nm thickness of each just for the sake of simplicity of the simulation procedure. In our simulation performed with Lumerical FDTD software, we ascribe the absorption to the layer of QD by adding the imaginary refractive index (*i.e.*, the absorption values k) over the extended SWIR band from 1800 to 2000 nm. In Fig. 6.3(a), the absorption intensity profile map shows the light absorbed inside the 200-nm-thick InGaAs QD layer, where the QDs actually absorb only 0.5% of the incident SWIR light as shown by the absorbance spectral lineshape. However, after adding a DBR in the system with the reflectance peak around 1900 nm, the absorption around that wavelength

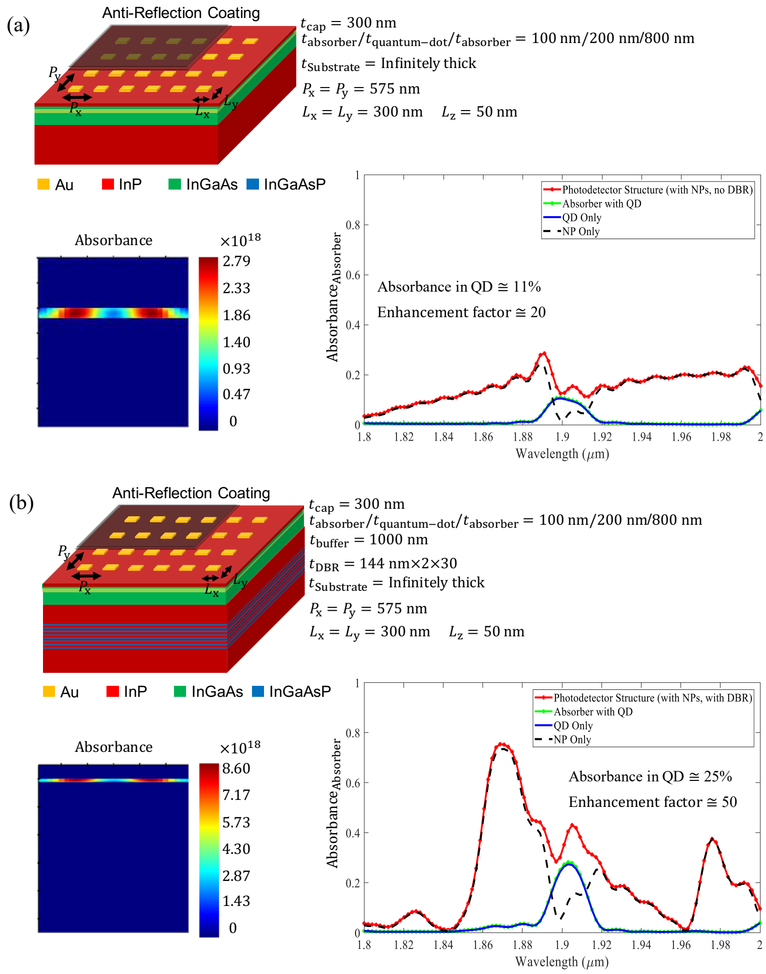

FIGURE 6.4: (a) A 2D plasmonic metasurface grating is added on top of the InP cap layer in the photodetector structure (without DBR) shown in Fig. 6.3(a). (b) A 2D plasmonic metasurface grating is added on top of the InP cap layer in the photodetector structure (with DBR) shown in Fig. 6.3(b). The QD absorbance intensity map and the spectra in the extended SWIR regime are shown side-by-side with the corresponding structures.

is enhanced up to 2.5% (by a factor of 5 or one order of magnitude intensity enhancement), as depicted in Fig. 6.3(b). Next, we add a metasurface array with the lattice mode around 1900 nm to the absorber layers without and with DBRs, which are shown in Fig. 6.4(a) and Fig. 6.4(b) with the corresponding absorbance intensity maps and spectra, respectively. The lattice periodicity $P = P_x = P_y = 575$ nm is set according to the following Bragg diffraction condition:

$$\lambda = nP, \tag{6.1}$$

where $n = n_{\text{eff}} = 3.3$ around 1900 nm. Fig. 6.4(a) shows that, in the presence of the metasurface grating, the absorbed intensity is enhanced by two orders of magnitude compared to the original absorbed intensity depicted in Fig. 6.3(a). Fig. 6.4(a) shows that the absorbance (with the metasurface but without a DBR) is increased to 11% (∼20 times larger than that in Fig. 6.3(a)). Nevertheless, Fig. 6.4(b) shows that the absorbance (with both the metasurface and DBR) is increased to 25% (∼50 times larger than that in Fig. 6.3(a)).

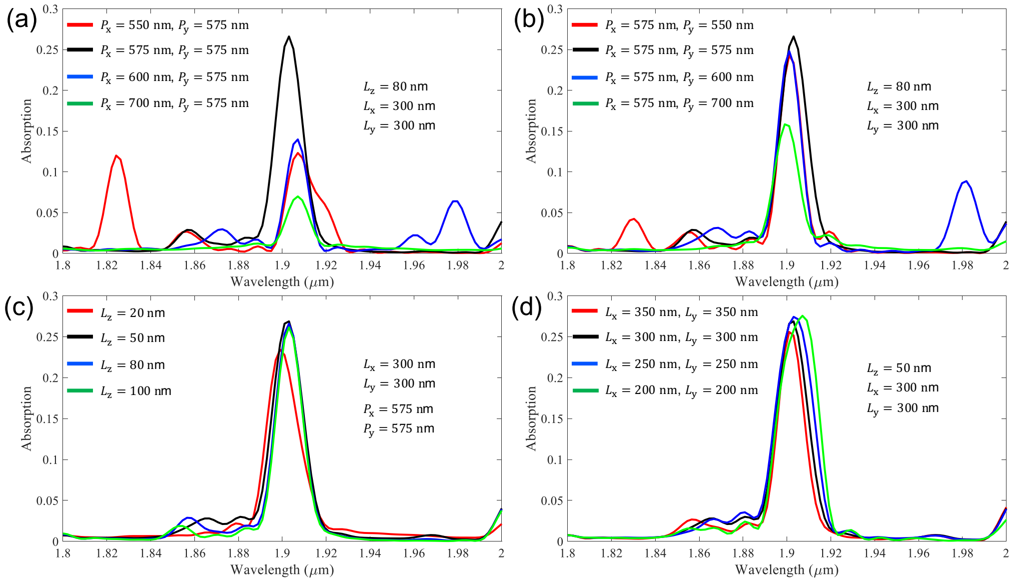

FIGURE 6.5: Maximizing the QD absorbance by tuning (a) the metasurface periodicity alongside the incident-light polarization, (b) the metasurface periodicity in the direction orthogonal to the incident-light polarization, (c) the thickness of the individual nanoparticles and (d) the area of the individual square nanoparticles, respectively.

Lastly, Fig. 6.5(a-d) show how we maximize the absorbance peak around 1900 nm of the extended SWIR band inside the QD by tuning the grating array periodicity by individually varying the periodicity P_x (Fig. 6.5(a)) and P_y (Fig. 6.5(b)), the particle thickness L_z (Fig. 6.5(c)) and the particle dimensions L_x and L_y (Fig. 6.5(d)), respectively.

6.3 Conclusions

In summary, we are presently analyzing the 2D plasmonic nanoparticle arrays developed in the two different projects described in this chapter to explore their potential as lattice diffraction gratings to excite out-of-plane non-localized resonances in different optical platforms.

In one of our ongoing projects, we designed an ultra-high-Q multiresonant and multi-modal flat meta-optics system by combining a periodic lattice metasurface with a high-refractive-index thin-film material to trap the collectively scattered out-of-plane lattice modes of the metasurface in the form of a series of GMRs at multiple wavelengths spread over a broadband optical spectrum. Our novel design is based on a unique mechanism that allows for an interplay between the lattice modes of the metasurface and the guided modes inside the thin film. Our designed flat meta-optics is expected to ease the limitation and restrictions that the current metasurface techniques encounter in practical applications.

In another ongoing project, we designed a plasmonic metasurface-integrated InGaAs/InP lattice-matched QD photodetector operating at the extended SWIR regime. While the InGaAs QD initiates a small amount of the photon absorption at the extended SWIR band around 1900 nm wavelength, the plasmonic metasurface consisting of the 2D nanoparticles array dramatically enhances the rate of absorption inside such lattice-matched QDs. Thus, such an improvement could increase the Q.E., henceforth, the responsivity of the lattice-matched InGaAs/InP photodiode structure, which is essential for the room-temperature operation of the extended-SWIR photodetector with a high signal-to-noise ratio (SNR).

Chapter 7

Conclusions and Future Work

7.1 Summary of the Primary Achievements

Over the last decade, metasurfaces with high-Q resonances have been proposed and demonstrated with a diverse range of functionalities in flat-optic systems. High-Q resonant metasurfaces can manipulate free-space light's amplitude, frequency, phase, and polarization [8], [9], [11], [82], [88]–[90]. Such metasurfaces could be used for efficient biosensing [69], [91], nanolasing [74], [92]–[94], entangled-photon-pair generation [95], all-optical and electro-optical modulation-based wavefront shaping, beam focusing and beam steering [56], [57], [82], *etc.*

In this dissertation, we designed and demonstrated such resonant metasurfaces with high-Q resonances comprising plasmonic meta-atoms, which are made of extremely lossy metallic nanoparticles. Even with low-Q localized surface plasmon resonances (LSPRs), such plasmonic nanoparticles often contribute in light-matter interaction via strong local-field enhancements. One such example is the nonlinear plasmonic effect. Inspired by the fact, in Chapter 2, we see how the plasmonic nanoparticles' geometry can play a crucial role in forming microscopic second-order nonlinear optical responses, typically characterized by the hyperpolarizability of the meta-atoms. Nevertheless, in the end, we also observed how the nonlocalized high-Q resonances could improve the efficiency of the second-harmonic generation (SHG) process, which is the most common example of second-order nonlinear optical responses.

Inspired by such enhanced nonlinear SHG process enabled by non-localized plasmonic surface-lattice resonances (SLRs) reported in Chapter 2, next, we successfully demonstrated a plasmonic metasurface with non-localized ultra-high-Q SLRs in Chapter 3. We demonstrated the high-Q SLR at the infrared wavelength by arranging gold nanoparticles periodically in 2D lattice arrangements. The Q-factor of the observed SLR was on the order of 10^3. Such a large Q-factor was at least one order of magnitude higher than any previously experimentally observed plasmonic

SLR Q-factors and two orders of magnitude higher than the traditional localized resonances associated with individual plasmonic or dielectric particles. Apart from that, in Chapter 4, we also demonstrated a metasurface with polarization-controlled periodicity-dependent dual SLRs. Throughout these projects, we successfully debunked a long-standing myth, according to which it was believed that plasmonic elements hinder obtaining high-Q resonances in any optical platform.

Notwithstanding, the high-Q-resonance systems analyzed in Chapter 3 and Chapter 4 have two practical design limitations, which may restrict them from being practically implemented. First, the in-plane SLR excitation under a normal incidence requires the nanoparticles' array to be cladded by a medium with the same refractive index as that of the substrate. In the case of any near-field application, for example, biosensing, that cladding layer becomes an obstacle between the nanoparticles and the substance of interest that is supposed to be detected. In addition, under a particular linearly polarized normally incident light, only a single in-plane SLR can be excited; in contrast, for many nonlinear optical processes such as frequency conversion and mixing, multiple high-Q resonances could be more desired.

To address these issues, in Chapter 5, we developed the methods of exciting multiple high-Q resonances in a metasurface. Here, we demonstrated the technique of trapping the out-of-plane lattice modes excited by the periodic nanoparticles array inside a thin homogeneous cladding layer. However, since those out-of-plane lattice resonances overlapped with the broad localized surface-plasmon resonances (LSPRs) associated with the individual nanoparticles, the Q-factors of such out-of-plane lattice resonances were not sufficiently high. One possibility could be to blue-shift the LSPRs to avoid such deteriorating overlap. Such blue-shifting would require reducing the nanoparticles' length alongside the light polarization. However, larger nanoparticles, which act as a 2D array of small mirrors, are also required to trap the out-of-plane lattice modes inside the cladding layer. Due to this trade-off, we cannot eliminate the overlap between the LSPRs and the out-of-plane lattice resonances. Despite all of these facts, we considered this novel work a milestone for future research advancements.

7.2 Current Research on Tackling the Limitations

Many optical dielectric and semiconductor thin-film materials play crucial roles in light modulation and detection. For example, lithium niobate ($LiNbO_3$) thin films are frequently used in electro-optical modulation [96], wavefront shaping [56], [57], optical frequency conversion and mixing [58], and photon-pair generation [95] due to their strong second-order nonlinear properties [54], [55]. However, the efficiency of such processes is very low in such thin-film structures. In such cases, SLRs could be useful to enhance the efficiency of such processes. Nevertheless, one cannot deposit a thin film of $LiNbO_3$ as a cladding layer; thus, medium homogeneity cannot be achieved in situations where $LiNbO_3$ is used. A similar situation could arise if one aims to implement the SLR to enhance the light absorption in a semiconductor photodiode made of indium gallium arsenide (InGaAs) and indium phosphide (InP). Note that, here $LiNbO_3$), InGaAs, and InP are just examples; the same problem could be faced in many other optical dielectric and semiconductor materials which are not listed here. To counter these challenges, we have recently developed the concept of 2D nanoparticle lattice diffraction grating-controlled guided mode resonances (GMRs) to enhance light-matter interaction in the inhomogeneous or heterogeneous metasurface structures formed by the thin-film materials which fall in the category described above.

Considering the successfully accomplished projects described in Chapter 2 to Chapter 5 as the groundwork, in our current research, we are applying our metasurface diffraction lattice-controlled GMR concept in different types of thin-film materials. We split our current research into two different projects, which are described in Chapter 6 of the thesis. In those projects, we aim to excite nonlocalized resonances in different thin-film material platforms using 2D plasmonic nanoparticle arrays for two different application purposes.

In one of those projects, we have recently designed a plasmonic lattice-coupled $LiNbO_3$ thin film. In our simulation, we have discovered an octave-spanned multi-high-Q GMRs appear from the metasurface.

In another ongoing project, we also have preliminarily observed the excitation of a plasmonic lattice-coupled mode in the quantum-dot (QD)-like thin-film layer of indium gallium arsenide (InGaAs) via a secondary layer of indium phosphide (InP), which results in the light absorption enhancement inside the InGaAs layer at the extended short-wavelength infrared (extended SWIR) regime.

7.3 Future Plans for Practical Implementations

As discussed above, Chapter 6 of the thesis describes the two ongoing projects. Nevertheless, the projects are currently in their preliminary design stage. Both projects ultimately require to be validated by the experimental characterization with successful implementation in their promised applications.

For that purpose, In the case of the first project on $LiNbO_3$ thin-film-based metasurface, very soon we are going to fabricate a test sample and characterize its linear transmission spectra to verify the appearance of the multi-high-Q resonances in our simulation. In parallel, we also want to rigorously analyze the origin of such multi-high-Q resonances by observing their corresponding electric-field maps. Once we experimentally verify the existence and analyze the origin of the multi-high-Q, in the next steps, we aim to investigate the impacts of the multi-high-Q resonances in practical applications. $LiNbO_3$ is famous for the processes like electro-optical light modulation [21], nonlinear optical frequency conversion and mixing, and entangled photon-pair generation [55]. Nevertheless, in thin-film configuration, $LiNbO_3$ exhibits a relatively low efficiency of the aforementioned processes. In addition, the uncovered plasmonic nanoparticles in this system could be utilized for sensing purposes [91]. We believe the experimental realization of such multi-high-Q metasurfaces would bring about numerous benefits for flat-optics technologies, for example, beam-steering in light detection and ranging (LiDAR) applications [51]., frequency switching and quantum-signal manipulation in free-space optical communications [66]., and biosensing in medical applications [69]..

On the other hand, we are also planning to fabricate metasurface diffraction lattice-coupled InGaAs QD photodiode devices. Once the fabrication of the sample is completed, we will characterize the sample to verify the absorption enhancement in the InGaAs QD layers by extracting its quantum efficiency, *i.e.*, the ability to convert the incident photons into the electric current by creating electron-hole pairs in the photodiode p-n junction. Verification of our simulation would lead us to demonstrate the first-ever lattice-matched InGaAs photodetector operating at room temperature to detect extended-SWIR light.

If we succeed in these ongoing projects in the near future, the next step is to implement the metasurface-based flat optical resonators in advanced state-of-the-art modern technology. My personal interest is in developing a LiDAR comprising a flat nanolaser, an electro-optical beam-steering device to spatially modulate the laser, and a detector operating in the eye-safe extended SWIR regime [51], [52]. An improved version of such a LiDAR could be sought in future automobile or free-space optical communication systems. In addition, I also want to contribute to developing biosensing and imaging devices for medical applications [69], [97]. I believe, my research contributions described in my Ph.D. dissertation will pave the way to realize my future plans by creating a bridge between fundamental science and real-life technologies. Thus, this Ph.D. thesis should be considered not only the end of graduate studies but also as the end of the beginning of a big dream dedicated to the ultimate advancement of human civilization.

Bibliography

[1] B. E. Saleh and M. C. Teich, *Fundamentals of photonics*. john Wiley & sons, 2019.

[2] E. Hecht, *Optics*. Pearson Education India, 2012.

[3] M. Born and E. Wolf, *Principles of optics: electromagnetic theory of propagation, interference and diffraction of light*. Elsevier, 2013.

[4] E. Abbe, "Beiträge zur theorie des mikroskops und der mikroskopischen wahrnehmung," *Archiv für mikroskopische Anatomie*, vol. 9, no. 1, pp. 413–468, 1873.

[5] D. K. Gramotnev and S. I. Bozhevolnyi, "Plasmonics beyond the diffraction limit," *Nature photonics*, vol. 4, no. 2, pp. 83–91, 2010.

[6] R. Feynman, "There's plenty of room at the bottom," in *Feynman and computation*, CRC Press, 2018, pp. 63–76.

[7] L. Novotny and B. Hecht, *Principles of nano-optics*. Cambridge university press, 2012.

[8] N. I. Zheludev and Y. S. Kivshar, "From metamaterials to metadevices," *Nature materials*, vol. 11, no. 11, pp. 917–924, 2012.

[9] N. Yu and F. Capasso, "Flat optics with designer metasurfaces," *Nature materials*, vol. 13, no. 2, pp. 139–150, 2014.

[10] X. C. Tong, *Functional metamaterials and metadevices*. Springer, 2018.

[11] A. H. Dorrah and F. Capasso, "Tunable structured light with flat optics," *Science*, vol. 376, no. 6591, eabi6860, 2022.

[12] Y. Kivshar and A. Miroshnichenko, "Meta-optics with mie resonances," *Optics and Photonics News*, vol. 28, no. 1, pp. 24–31, 2017.

[13] S. Kruk and Y. Kivshar, "Functional meta-optics and nanophotonics governed by mie resonances," *Acs Photonics*, vol. 4, no. 11, pp. 2638–2649, 2017.

[14] Y. Kivshar, "All-dielectric meta-optics and non-linear nanophotonics," *National Science Review*, vol. 5, no. 2, pp. 144–158, 2018.

[15] K. Koshelev, A. Bogdanov, and Y. Kivshar, "Meta-optics and bound states in the continuum," *Science Bulletin*, vol. 64, no. 12, pp. 836–842, 2019.

[16] M. K. Chen, X. Liu, Y. Sun, and D. P. Tsai, "Artificial intelligence in meta-optics," *Chemical Reviews*, vol. 122, no. 19, pp. 15 356–15 413, 2022.

[17] S. Abdollahramezani, O. Hemmatyar, and A. Adibi, "Meta-optics for spatial optical analog computing," *Nanophotonics*, vol. 9, no. 13, pp. 4075–4095, 2020.

[18] K. Shastri and F. Monticone, "Nonlocal flat optics," *Nature Photonics*, pp. 1–12, 2022.

[19] D. N. Neshev and A. E. Miroshnichenko, "Enabling smart vision with metasurfaces," *Nature Photonics*, pp. 1–10, 2022.

[20] N. Meinzer, W. L. Barnes, and I. R. Hooper, "Plasmonic meta-atoms and metasurfaces," *Nature photonics*, vol. 8, no. 12, pp. 889–898, 2014.

[21] V. G. Kravets, A. V. Kabashin, W. L. Barnes, and A. N. Grigorenko, "Plasmonic surface lattice resonances: A review of properties and applications," *Chemical Reviews*, vol. 118, pp. 5912–5951, 2018.

[22] E. I. Green, "The story of q," *American Scientist*, vol. 43, no. 4, pp. 584–594, 1955.

[23] C. K. Alexander and M. N. Sadiku, *Fundamentals of electric circuits*. McGraw-Hill Education, 2000.

[24] M. Agio and D. M. Cano, "The purcell factor of nanoresonators," *Nature photonics*, vol. 7, no. 9, pp. 674–675, 2013.

[25] A. I. Kuznetsov, A. E. Miroshnichenko, M. L. Brongersma, Y. S. Kivshar, and B. Luk'yanchuk, "Optically resonant dielectric nanostructures," *Science*, vol. 354, no. 6314, aag2472, 2016.

[26] K. L. Kelly, E. Coronado, L. L. Zhao, and G. C. Schatz, "The optical properties of metal nanoparticles: The influence of size, shape, and dielectric environment," *J. Phys. Chem. B*, vol. 107, no. 3, pp. 668–677, 2003.

[27] S. A. Maier *et al.*, *Plasmonics: fundamentals and applications*. Springer, 2007.

[28] C. F. Bohren and D. R. Huffman, *Absorption and scattering of light by small particles*. John Wiley & Sons, 2008.

[29] K. A. Willets and R. P. Van Duyne, "Localized surface plasmon resonance spectroscopy and sensing," *Annual review of physical chemistry*, vol. 58, no. 1, pp. 267–297, 2007.

[30] C. P. Burrows and W. L. Barnes, "Large spectral extinction due to overlap of dipolar and quadrupolar plasmonic modes of metallic nanoparticles in arrays," *Optics express*, vol. 18, no. 3, pp. 3187–3198, 2010.

[31] V. G. Kravets, A. V. Kabashin, W. L. Barnes, and A. N. Grigorenko, "Plasmonic surface lattice resonances: A review of properties and applications," *Chemical reviews*, vol. 118, no. 12, pp. 5912–5951, 2018.

[32] D. Khlopin, F. Laux, W. P. Wardley, *et al.*, "Lattice modes and plasmonic linewidth engineering in gold and aluminum nanoparticle arrays," *JOSA B*, vol. 34, no. 3, pp. 691–700, 2017.

[33] C. Cherqui, M. R. Bourgeois, D. Wang, and G. C. Schatz, "Plasmonic surface lattice resonances: Theory and computation," *Accounts of chemical research*, vol. 52, no. 9, pp. 2548–2558, 2019.

[34] B. Auguié and W. L. Barnes, "Collective resonances in gold nanoparticle arrays," *Physical Review Letters*, vol. 101, no. 14, pp. 1–4, 2008, ISSN: 00319007.

[35] S. R. K. Rodriguez, "Coupling light and matter in metallic nanoparticle arrays," Ph.D. dissertation, Technische Universiteit Eindhoven, Eindhoven, 2014.

[36] G. W. Castellanos, P. Bai, and J. Gómez Rivas, "Lattice resonances in dielectric metasurfaces," *Journal of Applied Physics*, vol. 125, no. 21, p. 213 105, 2019.

[37] S. Rodriguez, M. Schaafsma, A Berrier, and J. G. Rivas, "Collective resonances in plasmonic crystals: Size matters," *Physica B: Condensed Matter*, vol. 407, no. 20, pp. 4081–4085, 2012.

[38] K. Koshelev, S. Lepeshov, M. Liu, A. Bogdanov, and Y. Kivshar, "Asymmetric metasurfaces with high-q resonances governed by bound states in the continuum," *Physical review letters*, vol. 121, no. 19, p. 193 903, 2018.

[39] S. Murai, D. R. Abujetas, L. Liu, *et al.*, "Engineering bound states in the continuum at telecom wavelengths with non-bravais lattices," *arXiv preprint arXiv:2204.09986*, 2022.

[40] S. R. K. Rodriguez, A. Abass, B. Maes, O. T. Janssen, G. Vecchi, and J. G. Rivas, "Coupling bright and dark plasmonic lattice resonances," *Physical Review X*, vol. 1, no. 2, p. 021 019, 2011.

[41] G. Quaranta, G. Basset, O. J. Martin, and B. Gallinet, "Recent advances in resonant waveguide gratings," *Laser & Photonics Reviews*, vol. 12, no. 9, p. 1 800 017, 2018.

[42] J. Zhang, J. Ma, M. Parry, *et al.*, "Spatially entangled photon-pairs from lithium niobate nonlocal metasurfaces," *Science Advances*, vol. 8, no. 30, eabq4240, 2022.

[43] G. Pitruzzello, "Metaoptics for the consumer market," *Nature Photonics*, pp. 1–2, 2022.

[44] M. Khorasaninejad and F. Capasso, "Metalenses: Versatile multifunctional photonic components," *Science*, vol. 358, no. 6367, eaam8100, 2017.

[45] M. Khorasaninejad, W. T. Chen, R. C. Devlin, J. Oh, A. Y. Zhu, and F. Capasso, "Metalenses at visible wavelengths: Diffraction-limited focusing and subwavelength resolution imaging," *Science*, vol. 352, no. 6290, pp. 1190–1194, 2016.

[46] W. T. Chen, A. Y. Zhu, V. Sanjeev, *et al.*, "A broadband achromatic metalens for focusing and imaging in the visible," *Nature nanotechnology*, vol. 13, no. 3, pp. 220–226, 2018.

[47] A. H. Dorrah, N. A. Rubin, A. Zaidi, M. Tamagnone, and F. Capasso, "Metasurface optics for on-demand polarization transformations along the optical path," *Nature Photonics*, vol. 15, no. 4, pp. 287–296, 2021.

[48] R. C. Devlin, A. Ambrosio, N. A. Rubin, J. B. Mueller, and F. Capasso, "Arbitrary spin-to–orbital angular momentum conversion of light," *Science*, vol. 358, no. 6365, pp. 896–901, 2017.

[49] N. A. Rubin, G. D'Aversa, P. Chevalier, Z. Shi, W. T. Chen, and F. Capasso, "Matrix fourier optics enables a compact full-stokes polarization camera," *Science*, vol. 365, no. 6448, eaax1839, 2019.

[50] J. B. Mueller, N. A. Rubin, R. C. Devlin, B. Groever, and F. Capasso, "Metasurface polarization optics: Independent phase control of arbitrary orthogonal states of polarization," *Physical Review Letters*, vol. 118, no. 11, p. 113 901, 2017.

[51] I. Kim, R. J. Martins, J. Jang, *et al.*, "Nanophotonics for light detection and ranging technology," *Nature nanotechnology*, vol. 16, no. 5, pp. 508–524, 2021.

[52] "Lidar drives forwards," *Nature Photonics*, vol. 12, p. 441, 2018.

[53] B. C. Kress and C. Peroz, "Optical architectures for displays and sensing in augmented, virtual, and mixed reality (ar, vr, mr)," in *Proc. SPIE*, vol. 11310, 2020, p. 1 131 001.

[54] R. W. Boyd, *Nonlinear optics*. Academic press, 2020.

[55] A. Fedotova, L. Carletti, A. Zilli, *et al.*, "Lithium niobate meta-optics," *ACS Photonics*, vol. 9, no. 12, pp. 3745–3763, 2022.

[56] E. Klopfer, M. Lawrence, D. R. Barton III, J. Dixon, and J. A. Dionne, "Dynamic focusing with high-quality-factor metalenses," *Nano Letters*, vol. 20, no. 7, pp. 5127–5132, 2020.

[57] E. Klopfer, S. Dagli, D. Barton III, M. Lawrence, and J. A. Dionne, "High-quality-factor silicon-on-lithium niobate metasurfaces for electro-optically reconfigurable wavefront shaping," *Nano Letters*, vol. 22, no. 4, pp. 1703–1709, 2022.

[58] A. Fedotova, M. Younesi, J. Sautter, *et al.*, "Second-harmonic generation in resonant nonlinear metasurfaces based on lithium niobate," *Nano letters*, vol. 20, no. 12, pp. 8608–8614, 2020.

[59] G. P. Agrawal, *Fiber-optic communication systems*. John Wiley & Sons, 2012.

[60] G. P. Agrawal, *Lightwave technology: components and devices*. John Wiley & Sons, 2004.

[61] M. P. Hansen and D. S. Malchow, "Overview of swir detectors, cameras, and applications," in *Thermosense Xxx*, SPIE, vol. 6939, 2008, pp. 94–104.

[62] R Breiter, M Benecke, D Eich, *et al.*, "Extended swir imaging for targeting and reconnaissance," in *Infrared Technology and Applications XLIV*, SPIE, vol. 10624, 2018, pp. 11–21.

[63] R. N. Lane, "The swir advantage," in *Airborne Reconnaissance XIX*, SPIE, vol. 2555, 1995, pp. 246–254.

[64] K. Koshelev and Y. Kivshar, "Light trapping gets a boost," *Nature: News and Views*, 2019.

[65] K. Koshelev, Y. Tang, K. Li, D.-Y. Choi, G. Li, and Y. Kivshar, "Nonlinear metasurfaces governed by bound states in the continuum," *ACS Photonics*, vol. 6, no. 7, pp. 1639–1644, 2019.

[66] A. S. Solntsev, G. S. Agarwal, and Y. S. Kivshar, "Metasurfaces for quantum photonics," *Nature Photonics*, vol. 15, no. 5, pp. 327–336, 2021.

[67] T. Santiago-Cruz, S. D. Gennaro, O. Mitrofanov, *et al.*, "Resonant metasurfaces for generating complex quantum states," *Science*, vol. 377, no. 6609, pp. 991–995, 2022.

[68] F. Yesilkoy, E. R. Arvelo, Y. Jahani, *et al.*, "Ultrasensitive hyperspectral imaging and biodetection enabled by dielectric metasurfaces," *Nature Photonics*, vol. 13, no. 6, pp. 390–396, 2019.

[69] H. Altug, S.-H. Oh, S. A. Maier, and J. Homola, "Advances and applications of nanophotonic biosensors," *Nature Nanotechnology*, vol. 17, no. 1, pp. 5–16, 2022.

[70] M. Saad-Bin-Alam, "Analysis of plasmonic metastructures for engineered nonlinear nanophotonics," Ph.D. dissertation, University of Ottawa, 2019.

[71] M. S. Bin-Alam, J. Baxter, K. M. Awan, *et al.*, “Hyperpolarizability of plasmonic meta-atoms in metasurfaces,” *Nano Letters*, vol. 21, no. 1, pp. 51–59, 2020.

[72] M. S. Bin-Alam, O. Reshef, Y. Mamchur, *et al.*, “Ultra-high-q resonances in plasmonic metasurfaces,” *Nature communications*, vol. 12, no. 1, pp. 1–8, 2021.

[73] T. Stolt, A. Vesala, H. Rekola, P. Karvinen, T. K. Hakala, and M. J. Huttunen, “Multiply-resonant second-harmonic generation using surface lattice resonances in aluminum metasurfaces,” *Optics Express*, vol. 30, no. 3, pp. 3620–3631, 2022.

[74] M. I. Stockman, K. Kneipp, S. I. Bozhevolnyi, *et al.*, “Roadmap on plasmonics,” *Journal of Optics*, vol. 20, no. 4, p. 043 001, 2018.

[75] J. Kelavuori, V. Vanyukov, T. Stolt, *et al.*, “Thermal control of plasmonic surface lattice resonances,” *Nano Letters*, vol. 22, no. 10, pp. 3879–3883, 2022.

[76] M. S. Bin-Alam, O. Reshef, R. N. Ahmad, *et al.*, “Cross-polarized surface lattice resonances in a rectangular lattice plasmonic metasurface,” *Optics Letters*, vol. 47, no. 8, pp. 2105–2108, 2022.

[77] O. Reshef, M. Saad-Bin-Alam, M. J. Huttunen, *et al.*, “Multiresonant high-q plasmonic metasurfaces,” *Nano letters*, vol. 19, no. 9, pp. 6429–6434, 2019.

[78] W. Zhou, M. Dridi, J. Y. Suh, *et al.*, “Lasing action in strongly coupled plasmonic nanocavity arrays,” *Nature nanotechnology*, vol. 8, no. 7, pp. 506–511, 2013.

[79] T. Stolt and M. J. Huttunen, “Broadband frequency conversion of ultrashort pulses using high-q metasurface resonators,” *New Journal of Physics*, vol. 24, no. 2, p. 025 004, 2022.

[80] M. S. Bin-Alam, M. Z. Alam, K. Dolgaleva, and R. W. Boyd, “Ultra-high-q multi-resonant metasurface using plasmonic lattice in inhomogeneous medium,” in *2022 Conference on Lasers and Electro-Optics (CLEO)*, IEEE, 2022, pp. 1–2.

[81] Z. Liu, Y. Xu, Y. Lin, *et al.*, “High-q quasibound states in the continuum for nonlinear metasurfaces,” *Physical Review Letters*, vol. 123, no. 25, p. 253 901, 2019.

[82] M. Lawrence, D. R. Barton, J. Dixon, *et al.*, “High quality factor phase gradient metasurfaces,” *Nature Nanotechnology*, vol. 15, no. 11, pp. 956–961, 2020.

[83] A. H. Jones, S. D. March, S. R. Bank, and J. C. Campbell, "Low-noise high-temperature alinassb/gasb avalanche photodiodes for 2-μm applications," *Nature Photonics*, vol. 14, no. 9, pp. 559–563, 2020.

[84] S. Kasap, *Optoelectronics & photonics: principles & practices: international edition*. Pearson, 2013.

[85] K. Kishino, M. S. Unlu, J.-I. Chyi, J Reed, L Arsenault, and H. Morkoc, "Resonant cavity-enhanced (rce) photodetectors," *IEEE Journal of Quantum Electronics*, vol. 27, no. 8, pp. 2025–2034, 1991.

[86] Y. Nga Chen, Y. Todorov, B. Askenazi, *et al.*, "Antenna-coupled microcavities for enhanced infrared photo-detection," *Applied Physics Letters*, vol. 104, no. 3, p. 031 113, 2014.

[87] Y. L. Jing, Z. F. Li, Q. Li, *et al.*, "Pixel-level plasmonic microcavity infrared photodetector," *Scientific reports*, vol. 6, no. 1, pp. 1–8, 2016.

[88] K. Wang, M. Chekhova, and Y. Kivshar, "Metasurfaces," *Physics Today*, vol. 75, pp. 8–38, 2022.

[89] N. Yu, P. Genevet, M. A. Kats, *et al.*, "Light propagation with phase discontinuities: Generalized laws of reflection and refraction," *Science*, vol. 334, no. 6054, pp. 333–337, 2011.

[90] W. Wang, M. Ramezani, A. I. Väkeväinen, P. Törmä, J. G. Rivas, and T. W. Odom, "The rich photonic world of plasmonic nanoparticle arrays," *Materials today*, vol. 21, no. 3, pp. 303–314, 2018.

[91] B. Špačková, P. Wrobel, M. Bocková, and J. Homola, "Optical biosensors based on plasmonic nanostructures: A review," *Proceedings of the IEEE*, vol. 104, no. 12, pp. 2380–2408, 2016.

[92] D. Wang, W. Wang, M. P. Knudson, G. C. Schatz, and T. W. Odom, "Structural engineering in plasmon nanolasers," *Chemical reviews*, vol. 118, no. 6, pp. 2865–2881, 2017.

[93] R.-M. Ma and R. F. Oulton, "Applications of nanolasers," *Nature Nanotechnology*, vol. 14, no. 1, pp. 12–22, 2019.

[94] S. I. Azzam, A. V. Kildishev, R.-M. Ma, *et al.*, "Ten years of spasers and plasmonic nanolasers," *Light: Science & Applications*, vol. 9, no. 1, pp. 1–21, 2020.

[95] T. Santiago-Cruz, A. Fedotova, V. Sultanov, *et al.*, "Photon pairs from resonant metasurfaces," *Nano letters*, vol. 21, no. 10, pp. 4423–4429, 2021.

[96] H. Weigand, V. V. Vogler-Neuling, M. R. Escalé, *et al.*, "Enhanced electro-optic modulation in resonant metasurfaces of lithium niobate," *ACS Photonics*, vol. 8, no. 10, pp. 3004–3009, 2021.

[97] F. Yesilkoy, E. R. Arvelo, Y. Jahani, *et al.*, “Nanophotonic biosensors: From plasmonic to dielectric metasurfaces,” in *Optical Sensors*, Optical Society of America, 2019, SW4C–2.